Confinement effects and stability of spin-spirals and skyrmions in ultrathin magnetic films

Dissertation with the aim of achieving a doctoral degree
at the Faculty of Mathematics, Informatics and Natural Sciences
Department of Physics

of Universität Hamburg

submitted by M. Sc. Julian Claudius Hagemeister
from
Braunschweig

2016

Gutachter der Dissertation:

Herr Prof. Dr. R. Wiesendanger
Herr Prof. Dr. M. Thorwart

Gutachter der Disputation:

PD Dr. E. Vedmedenko
Prof. Dr. D. Horns
Prof. Dr. A. Lichtenstein
Herr Prof. Dr. R. Wiesendanger
Herr Prof. Dr. M. Thorwart

Vorsitzender des Prüfungsausschusses:

Prof. Dr. D. Horns

Datum der Disputation: 17.02.2017

Vorsitzender des Promotionsausschusses:

Prof. Dr. Wolfgang Hansen

Dekan der MIN-Fakultät:

Prof. Dr. Heinrich Graener

Abstract

Magnetic skyrmions are regarded as promising candidates for tiny and stable bits of information in future data storage devices which brought them into the focus of many research activities.

This thesis deals with unsolved fundamental issues about thermally activated transition processes between ferromagnetic and skyrmionic states as well as the behavior of skyrmion structures in confined geometries. The presented results were obtained with a self-written Monte Carlo program in combination with analytical and numerical methods.

Stochastic switching between ferromagnetic and skyrmionic states is analyzed with the help of the Arrhenius law and the Eyring equation. This yields activation energies and attempt frequencies. The attempt frequency of the skyrmion state is much lower than that of the ferromagnetic state which can be related to a higher entropy of the skyrmion state and is identified as the reason for the high stability of the skyrmion state.

For a skyrmionic material of finite size in the spin-spiral phase, a local parallel orientation of the spin-spiral vector with respect to an edge of the material results in a reduction of the energy. Additional energy can be saved by tilting the spin-spiral state at an edge with respect to the spin-spirals in the interior of the material. The results are used to explain recent experimental observations about spin-spiral states in magnetic Pd/Fe atomic bilayer islands on Ir(111).

In Fe/Ir(111), edge properties can be employed to tailor the alignment of the adjacent nanoskyrmion lattice. A diagonal of the square magnetic unit cell is coupled parallel to an edge of an Fe island. In contrast to this, a side of the magnetic unit cell is coupled parallel to a ferromagnetic edge. Experimental observations are well in line with Monte Carlo calculations.

Finally, effects of spatial variations of material parameters are studied. First, it is shown that they provide a convenient method to determine the phase space of skyrmionic materials. Second, they are used to obtain a qualitative understanding of recent experimental observations of non-axisymmetric skyrmions in triple layers of Fe on Ir(111).

Abstract

Magnetische Skyrmionen gelten als vielversprechende Kandidaten für Informationsbits in zukünftigen Datenspeichern und sind daher gegenwärtig Gegenstand von vielen Forschungsvorhaben.

Die vorliegende Arbeit untersucht mit theoretischen Methoden fundamentale Fragestellungen über den thermisch induzierten Übergang zwischen skyrmionischem und ferromagnetischem Zustand sowie das Verhalten von Skyrmionen in Materialien mit beschränkter räumlicher Ausdehnung. Die Ergebnisse wurden mit einem selbstgeschriebenen Monte Carlo Programm in Kombination mit analytischen und numerischen Rechnungen erzielt.

Stochastisches Schalten zwischen ferromagnetischen und skyrmionischen Zuständen wurde mithilfe der Arrhenis-Gleichung und Eyring-Gleichung untersucht. Auf diese Weise wurden Aktivierungsenergien und „Attempt"-Frequenzen bestimmt. Die „Attempt"-Frequenz des skyrmionischen Zustandes ist wesentlich kleiner als die des ferromagnetischen Zustandes, was durch eine höhere Entropie des skyrmionischen Zustandes erklärt werden kann. Sie sorgt für die hohe Stabilität des skyrmionischen Zustandes.

Am Rand eines skyrmionischen Materials in der Spin-Spiral-Phase führt eine lokal parallele Ausrichtung des Spin-Spiral-Vektors zu einer Absenkung der Energie. Ein weiterer Energiegewinn entsteht durch die Verkippung der Spin-Spirale am Rand gegenüber den Spin-Spiralen im Inneren des Materials. Diese Ergebnisse können experimentelle Messungen an magnetischen Inseln aus zwei atomaren Lagen aus Palladium und Eisen erklären.

In Fe/Ir(111) können die Kanteneigenschaften gezielt manipuliert werden, um Einfluss auf die räumliche Orientierung des angrenzenden Nanoskyrmiongitters zu nehmen. Die Diagonale der quadratischen magnetischen Einheitszelle koppelt parallel zu einer offenen Kante einer Eiseninsel. Dahingegen koppelt das Nanoskyrmiongitter mit einer Seite der magnetischen Einheitszelle an eine ferromagnetische Kante. Dieses Verhalten lässt sich sowohl in Experimenten als auch in den vorliegenden Monte Carlo Rechnungen beobachten.

Zuletzt werden die Effekte von räumlichen Variationen der Materialparameter studiert. Es wird gezeigt, dass dieser Ansatz eine komfortable Möglichkeit bietet, Phasendiagramme von skyrmionischen Systemen zu erstellen.

Darüber hinaus können räumlich variierende Materialparameter genutzt werden, um ein qualitatives Verständnis experimenteller Beobachtungen von nicht-achsensymmetrischen Skyrmionen in der atomaren Tripellage von Eisen auf Ir(111) zu erhalten.

Contents

Chapter 1

Introduction

Conservation of information has been a persistent topic throughout history of human kind. The oldest preserved artwork dates back to approximately 50,000 years ago [1], which early on revealed the need to retain information for oneself and others. Following this, it took a long time until the invention of written language revolutionized our ways of communicating a few thousand years BC by successively making vast amounts of information accessible for many people.

With this in mind, it is not surprising that we nowadays live in a society in which our everyday lives are dominated by information and communication technology. This has become possible due to discoveries in material sciences which allow to store and transfer information in highly sophisticated ways. Individual persons can use personal computers and smartphones next to various other gadgets in order to exchange information via the internet with people from all over the world. For the storage of data, there are various methods available which rely on electric charges in solid state disks or on the magnetism of material in hard disk drives. The magnetic recording was invented by the American Oberlin Smith in 1878, and subsequently the Dane Valdemar Poulsen patented a device for magnetic wire recording in the United States around 1900 [2]. Since then, the technology of magnetic recording has been greatly improved to keep up with contemporary requirements.

Currently, an individual bit of information is formed by an assembly of magnetic grains, which constitute tiny magnetic domains on the nanometer scale in a thin film disk. However, the limits in miniaturization seem to have

been reached due to conflicting material requirements known as the trilemma of magnetic recording [3]. A reduction of the bit size requires a reduction of the grain volumes, which results in the need for a large anisotropy energy to ensure thermal stability of the grains, but at the same time a low anisotropy energy is needed to ensure switchability of the magnetic bits with the write head [3]. At the moment, there are areal densities of about 1 Tb/inch^2 available [4], and different ideas are needed to increase the storage density even further. These range from an extension of the present technology by heat-assisted switching of the bits [5, 6, 7] to distinct storage concepts as the use of magnetic skyrmions as bits of information [8, 9]. Due to their potential for future data storage devices, magnetic skyrmions have become the focus of many research activities including this thesis.

Magnetic skyrmions are spatially localized magnetic knots embedded in a collinear ferromagnetic background [10, 11, 12]. They can be stabilized in certain material systems as non-centrosymmetric bulk crystals [13, 14, 15, 16, 17, 18, 19, 20] and ultrathin magnetic films [21, 22] on non-magnetic supporting crystals. Only these material systems allow for a non-vanishing Dzyaloshinskii-Moriya interaction [23, 24] which is essential for the formation of magnetic skyrmions. The bit size of a potential skyrmionic storage device is limited by the size of a skyrmion because the two states of a bit would be represented by the presence or absence of a skyrmion within a certain area. Even though magnetic skyrmions can be as small as a few nanometers in diameter [21, 22], realistic bit sizes are comparable to those in current magnetic storage devices. Therefore, an immediate increase of the bit density by the use of magnetic skyrmions is not apparent and the question about advantages of skyrmions as bits of information arises. Most promising is the exploitation of their particle-like properties which give rise to the possibility of manipulating their position within a material by an external force [25, 26, 27, 28, 29, 30, 31, 32, 33, 34, 35, 36, 37]. In particular, skyrmions can be moved along magnetic tracks giving rise to ideas of skyrmion-based race-track type storage devices [9, 38]. These have the huge advantage over solid state discs that they could be operated without any mechanically movable parts. Also, a significant increase in storage density may be possible by forming loops of skyrmion tracks. In this way, all three dimensions of space would be utilized for the data storage instead of

two dimensions as in current devices. Moreover, skyrmions may not only be employed as bits of information but also for logic operations in skyrmion-based logic devices [39].

A lot of research has been conducted in order to establish the foundations needed for the realization of such skyrmionic data storage devices. It was demonstrated both in experimental and theoretical studies that magnetic skyrmions can be written and deleted in a controlled fashion, as for example by the use of an external electric current [22]. Moreover, it was shown experimentally that skyrmions can be moved by electric currents with sufficient large velocities [40]. Currently, the main quest remains the identification of a suitable material that fulfills the necessary requirements in terms of material properties and practicability for industrial production processes. Recently, an important step was accomplished by the discovery of the first material system with interface-induced Dzyaloshinskii-Moriya interaction that not only allows for the stabilization of skyrmions at ultra-low temperatures but also at room temperature [41].

Apart from the search for materials that are suitable for technological application, there are still open questions concerning fundamental properties of skyrmionic systems. Consequently, this thesis investigates effects of material boundaries on the magnetic states of skyrmionic materials and how they could be employed to tailor the properties of individual skyrmions as well as skyrmion lattices as a whole. Furthermore, the energy landscape connecting skyrmionic and ferromagnetic states is studied in order to obtain an insight into the mechanisms governing the thermal stability of skyrmionic bits.

The main tool for the investigations was a self-written computer program that is based on a classical Monte Carlo method, the Metropolis algorithm. The following provides an overview of the content of this thesis.

Chapter 2 and chapter 3 provide an overview of previous theoretical and experimental findings about magnetic skyrmions and introduce theoretical concepts and methods used in the following chapters.

Chapter 4 deals with the stability of single skyrmions as a function of temperature and an external magnetic field as obtained with Monte Carlo calculations. Thermally activated stochastic switching between skyrmionic and ferromagnetic states is used to calculate mean lifetimes of the two states. These can

be used to derive energy barriers and attempt frequencies with the help of the Arrhenius law and to obtain an insight into the energy landscape of skyrmionic systems. Finally, the Monte Carlo results are compared to recent experimental observations about the magnetic Pd/Fe atomic bilayers on Ir(111).

In the following two chapters, confinement effects due to finite system sizes on the magnetic states of skyrmionic materials are discussed. First, numerical and analytical methods are combined to investigate the influence of boundaries onto spin-spiral states in zero external magnetic field in Chapter 5. Once more, the obtained results are compared to experimental observations about Pd/Fe atomic bilayer islands on Ir(111). Second, the behavior of the nanoskyrmion lattice in the atomic monolayer of Fe on Ir(111) in the presence of one or multiple competing edges is studied in chapter 6. In experiment, edges of Fe islands and Fe stripes as well as edges imposed by an additional ferromagnetic Ni island were investigated, recently. Monte Carlo calculations using energy parameters based on density function theory calculations lead to a deeper insight into the experimentally found edge effects and to an estimate about energy costs that arise due to formation of a domain wall between different rotational domains of the nanoskyrmion lattice.

Chapter 7 deals with spatial modulations of material parameters in skyrmionic systems. In the first part of the chapter, small parameter gradients are used to derive phase diagrams. The second part of the chapter investigates the origin of the highly non-axisymmetric skyrmionic textures found in triple atomic layers of Fe on Ir(111). In this experimental system, the material parameters spatially vary because of reconstruction features induced by a mismatch of lattice constants of the Iron and Iridium.

Chapter 8 ends the thesis with a summary and evaluation of the presented findings.

Chapter 2

Theoretical and experimental background

There are materials whose magnetic behavior can be understood without taking the influence of the environment onto the atomic magnetic moments into considerations. These include some crystals that contain rare earth elements for example [42]. However, for a large number of material systems, the influence of the environment onto the atomic magnetic moments is strong and can consequently not be neglected. The surrounding crystal field may result in a magnetic anisotropy which favors the alignment of the magnetization along certain crystallographic directions (see section 2.1.1). Furthermore, the localized atomic magnetic moments can be coupled to the magnetic moments of atoms in the close vicinity. This includes the exchange and Dzyaloshinskii-Moriya interaction between two magnetic moments (section 2.1.3 and section 2.1.4) and higher order contributions as the biquadratic interaction (section 2.1.6) and the 4-spin interaction (section 2.1.5). The competition of multiple of these energy contributions can be used to explain the formation of non-collinear magnetic states as spin-spirals and magnetic skyrmions which is discussed in section 2.2.

2.1 Energies in magnetic materials

2.1.1 Magnetic anisotropy

In magnetic materials, certain orientations of the magnetization can be energetically preferred which is called magnetic anisotropy. This phenomenon can originate from the sample shape, the crystal symmetry and stress [43]. The shape anisotropy has its origin in the demagnetization field due to free poles at surfaces of a sample and it prefers a minimization of the magnetic stray field. In contrast to this, the crystal anisotropy has a quantum mechanical origin. The spin of an electron in an atom is typically coupled to its orbital momentum which itself is linked to the shape of the charge distribution of the electron. This is commonly known as spin-orbit coupling. For an isolated atom, the energy of the atom does not depend on the spatial orientation of the electronic orbitals. However, the situation changes in solids where the atom is embedded in the crystal field of surrounding atoms and chemical bonding of the orbitals occurs. If the crystal field has a low symmetry and the orbital charge distribution is non-spherical the energy of the atom will depend on the spatial orientation of the orbital. An uniaxial crystal anisotropy is typically expressed as

$$E_{\mathrm{a}} = \sum_{i=1}^{n} K_i \sin^{2i} \Theta \tag{2.1}$$

but it is often sufficient to consider the first two terms, only. Within this description, a positive K_{i} denotes an easy axis. Θ is the angle between the direction of the magnetization and the direction of the easy axis of the considered material.

2.1.2 Demagnetization field

The magnetization $\mathbf{M}$ of a magnetic material is the macroscopic density of magnetic dipole moments [43]. At a surface with the surface normal $\mathbf{n}$ it gives rise to an effective magnetic charge density [44]

$$\sigma = \mathbf{n} \cdot \mathbf{M} \quad . \tag{2.2}$$

This causes vector magnetic fields both outside and inside of the material. The field that passes through the material is called *demagnetization field* because its orientation is opposite to the magnetization $\mathbf{M}$. In order to minimize the energy linked to the demagnetization field, surface charges are avoided where possible. This can be done by the orientation of a uniform magnetization along certain directions of a particular sample which gives rise to the shape anisotropy (section 2.1.1). Another way is the formation of domain structures. This thesis deals with magnetic skyrmions in ultrathin magnetic layers and hence the energy due to the demagnetization field is neglected. A system with large magnetic stray fields would stabilize bubble domains instead of magnetic skyrmions [45].

2.1.3 Exchange interaction

The exchange interaction is a quantum mechanical phenomenon that is responsible for long range order in magnetic materials. Its origins lie in the Coulomb repulsion between electrons and the Pauli exclusion principle. For two interacting electrons, its *isotropic* contribution [46] to the Hamiltonian is given by

$$\mathcal{H}_{\text{exch.}} = -J_{ij} \cdot \mathbf{S}_i \cdot \mathbf{S}_j \tag{2.3}$$

J_{ij} is the so called exchange constant which is calculated as the exchange integral for the two electron orbitals linked to the spins $\mathbf{S}_i$ and $\mathbf{S}_j$. In the literature, different conventions are used for the exchange constant. The group of S. Heinze in e.g. reference [21] provides the exchange energy per atom which means that double summations are used and the resulting energy is not divided by the factor of one half. This convention applies for chapter 5 and 6 since energy parameters from the group of S. Heinze were used. However, a different convention applies for the other chapters 4 and 7. There, the exchange energy is given per bond which means that when doing double summations, the resulting energy has to be multiplied by a factor of one half. The same applies for other interaction energies which are used within this thesis as the Dzyaloshinskii-Moriya interaction.

Depending on the sign of the exchange constant, either the singlet or triplet state and hence antiparallel or parallel spin alignment can be preferred energetically. A coherent rotation of the spin system does not lead to a change in the energy. The Bethe-Slater curve provides the energy of the triplet and singlet states as a function of the interatomic distance. Two electrons close to each other will have antiparallel spins because of the Pauli principle while a parallel alignment becomes favorable for larger distances. The interaction has been generalized for many body systems and is considered in the Hamiltonian of the Heisenberg model in the same form for all nearest-neighbor sites. For energy parameter sets for specific materials as e.g. the atomic monolayer Fe on Ir(111) (section 6), contributions going beyond the nearest-neighbor sites are also taken into account.

An additional *anisotropic* part of the exchange energy is typically neglected since it is only a comparably small relativistic effect [46]. It is expressed by $J_{xx,ij}S_{x,i}S_{x,j} + J_{yy,ij}S_{y,i}S_{y,j} + J_{zz,ij}S_{z,i}S_{z,j}$ and thus the energy of the system depends on the spatial orientation of the magnetic moments with respect to the line connecting the two magnetic sites. Throughout the thesis, only isotropic contributions of the exchange energy are considered, i.e. $J = J_{xx,ij} = J_{yy,ij} = J_{zz,ij}$. However, a dependence of J on the spatial orientation of a bond is used in chapter 7.

2.1.4 Dzyaloshinskii-Moriya interaction

Dzyaloshinskii reported in 1958 about an antisymmetric part of the exchange energy which he derived from crystal symmetry considerations [23]. It can provide a non-vanishing contribution in the combination of a low crystal symmetry and a large spin-orbit coupling. The interaction for two localized magnetic moments $\mathbf{S}_1$ and $\mathbf{S}_2$ is written as

$$\mathbf{D}_{i,j} \cdot (\mathbf{S}_i \times \mathbf{S}_j) = \mathbf{S}_i \cdot \begin{pmatrix} 0 & D_z & -D_y \\ -D_z & 0 & D_x \\ D_y & -D_x & 0 \end{pmatrix} \cdot \mathbf{S}_j \tag{2.4}$$

with the Dzyaloshinskii-Moriya (DM) vector $\mathbf{D}_{i,j}^T = (D_x, D_y, D_z)$ which is a material parameter. Note that different conventions about double summations

as explained in section 2.1.3 are used within this thesis. The Dzyaloshinskii-Moriya interaction favors a canting of the magnetic moments in contrast to the symmetric part of the exchange interaction which favors (anti-)parallel alignment. However, not only the angle between the magnetic moments influences the energy but also the spatial orientation of the magnetic moments with respect to the DM vector. Hence, the DM interaction is called anisotropic [47]. Moriya demonstrated the calculation of the strength of this interaction by using an extended version of Anderson's formalism of superexchange interaction incorporating the effect of spin-orbit coupling [24]. He considered two magnetic sites with spin-orbit coupling on the magnetic sites and different crystal field splittings for the two sites. The strength is equal to zero if there is a center of inversion at the point bisecting the line connecting the two lattice sites. Non-vanishing contributions can be found in non-centrosymmetric bulk crystals as the B20 compounds [48]. Additionally, A. Fert pointed out the possibility for non-vanishing contributions in ultrathin magnetic layers deposited onto supporting non-magnetic crystals [49]. Its strength was calculated by A. Fert and P.M. Levy [50]. They considered a three site mechanism which takes a non-magnetic impurity atom with a large spin-orbit interaction along with two magnetic sites into account. In this case, the DM interaction arises due to a spin-orbit scattering of the conduction electrons by the impurity atom. The Hamiltonian of the spin-orbit interaction is proportional to the atomic number Z [43] and hence the coupling constant D can expected to be large for heavy impurity atoms.

2.1.5 4-Spin interaction

The 4-spin interaction is a higher order contribution to the interaction between localized magnetic moments and it has its origin in the electron hopping between four atomic sites $\{ijkl\}$. It can be derived using the Hubbard model [51] as

$$E_{4-\text{spin}} = -\sum_{ijkl} K_{ijkl}[(\mathbf{S}_i \cdot \mathbf{S}_j)(\mathbf{S}_k \cdot \mathbf{S}_l) + (\mathbf{S}_i \cdot \mathbf{S}_l)(\mathbf{S}_j \cdot \mathbf{S}_k) - (\mathbf{S}_i \cdot \mathbf{S}_k)(\mathbf{S}_j \cdot \mathbf{S}_l)] \tag{2.5}$$

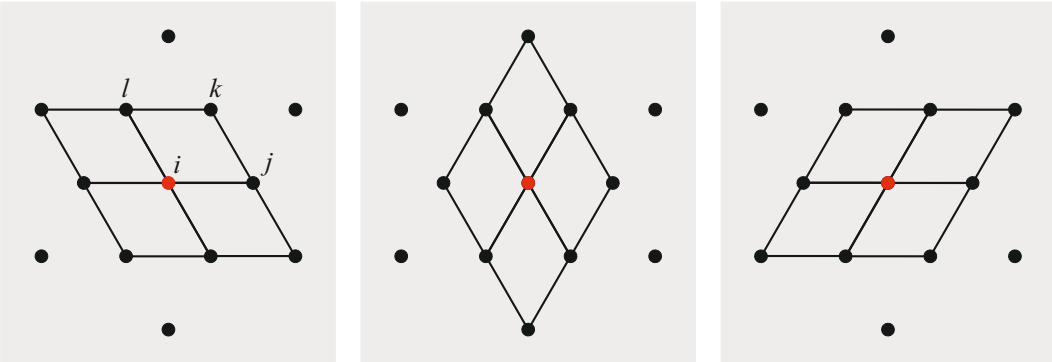

Figure 2.1: 4-Spin interaction. Sketch of the cells contributing to the calculation of the 4-spin energy of the magnetic moment at the lattice site marked in red.

with the material parameter K_{ijkl}. This expression is valid for any lattice [51] but within this thesis, it will be used for triangular two-dimensional lattices in chapter 6 for the description of Fe/Ir(111), only. Fig. 2.1 shows that twelve cells each consisting of four atoms have to be taken into account in order to calculate the 4-spin energy of the magnetic moment at one particular site of the triangular lattice. The magnetic ground state of a hypothetical material that can be described exclusively with a 4-spin interaction was investigated in Ref. [52].

2.1.6 Biquadratic interaction

The biquadratic energy term

$$E_{\text{biq}} = -\sum_{ij} B_{ij} (\mathbf{S}_i \cdot \mathbf{S}_j)^2 \tag{2.6}$$

with the material parameter B_{ij} is on the same expansion order as the 4-spin interaction. It is taken into account for nearest-neighbor sites and it favors a parallel or anti-parallel alignment of the corresponding magnetic moments in case of $B_{ij} > 0$. A perpendicular orientation of neighboring magnetic moments is favored when $B_{ij} < 0$. Ref. [52] presents a detailed discussion of the magnetic ground states for a two-dimensional hexagonal lattice. This interaction is used for the description of Fe/Ir(111) in chapter 6.

2.1.7 Zeeman energy

The Zeeman energy is responsible for a parallel alignment of the magnetic moments of a material with respect to an external magnetic field $\mathbf{B}$. The energy of a magnetic moment $\boldsymbol{\mu}$ is given by

$$E_{\mathrm{Z}} = -\boldsymbol{\mu} \cdot \mathbf{B} \quad . \tag{2.7}$$

2.2 Magnetic skyrmions

In the previous section, various energy contributions that play a role in the formation of non-trivial magnetic states were presented. Among these complex magnetic states are the so called magnetic skyrmions which are the focus of this thesis and are hence introduced in the following.

2.2.1 General introduction

Initially, skyrmions were discussed by the name giver Tony Skyrme in the context of non-linear field theory in order to describe elementary particles [53]. They are characterized by a topological integer number which prevents a continuous transformation of the field into a state with a different topological number. Later, it was found that this theory is also applicable to certain magnetic systems which led to the theoretical proposal of magnetic skyrmions [10, 54] as localized non-collinear magnetic textures with particle-like character [55]. It has become accepted knowledge that magnetic skyrmions are formed due to a competition of the Dzyaloshinskii-Moriya interaction, the exchange interaction and the magnetic anisotropy energy. Experimentally, skyrmions were observed in the bulk of non-centrosymmetric magnetic materials [13, 15, 16, 17, 20] and in ultrathin magnetic layers [21, 22] deposited onto supporting non-magnetic crystals. Skyrmions can appear in a Bloch- or in a Néel-type form [56] (see Fig. 2.2) as magnetic knots that are embedded in a ferromagnetic background. The focus of this thesis is on ultrathin film systems which typically exhibit the Néel-type skyrmions. Therein, the magnetization direction at the skyrmion center is opposite to the one of the ferromagnetic background and the magnetization profile through the skyrmion center is close to the one of a 360°

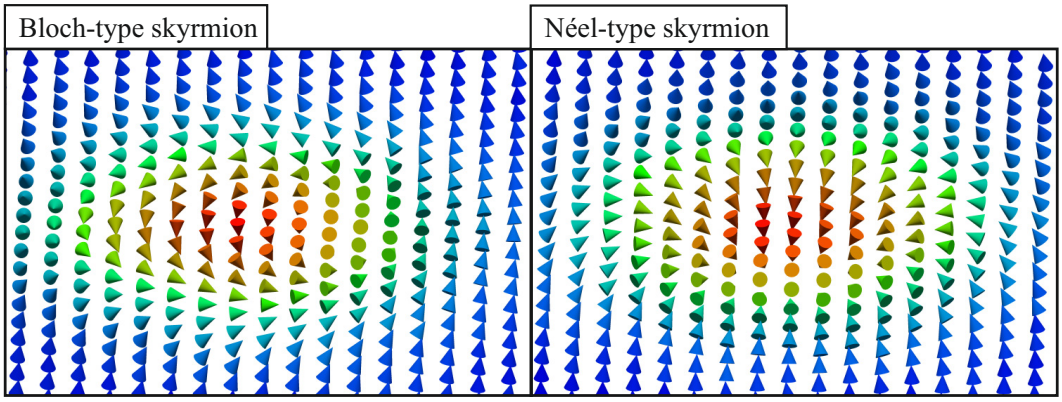

Figure 2.2: Magnetic skyrmions. Sketches of a chiral and Néel-type magnetic skyrmion. The cones indicate the spatial orientations of the atomic magnetic moments.

Néel-type magnetic domain wall [57]. This particular type of skyrmions is formed due to the spatial orientation of the DM vector which is perpendicular to the connection line of two magnetic sites and lies predominantly within the plane of the magnetic film due to symmetry reasons for this class of materials [58]. The skyrmions can appear depending on the exact material parameters and an external magnetic field in close packed lattices as the thermodynamical ground state or diluted as metastable isolated objects in a ferromagnetic background [11, 12].

Furthermore, additional energy contributions as the dipole-dipole interaction or the 4-spin interaction can have an influence on the properties of the skyrmions or even prevent the formation of skyrmions if they are comparably large. If for example the dipole-dipole interaction provides the dominating energy contribution so called bubble domains with a much larger lateral size and different stability properties are likely to be formed [45]. Still, a weak Dzyaloshinskii-Moriya interaction can be sufficient to impose a favorable sense of rotation and the resulting objects are called skyrmion bubbles [59].

The results of the Monte Carlo calculations that are presented in the course of this thesis are in close relation to skyrmionic ultrathin material systems as Fe/Ir(111) and Pd/Fe/Ir(111). Hence, the main experimental and theoretical findings about these systems are discussed in the following.

2.2.2 Ultrathin film systems

The first experimentally found ultrathin film system that exhibits magnetic skyrmions was the fcc stacked atomic monolayer of Fe on Ir(111) [60, 61, 21]. It is a rather unique system which can not be described in a satisfactory way by only taking the exchange and Dzyaloshinskii-Moriya interaction and the anisotropy energy into consideration. Instead, higher order energy contributions as the 4-spin interaction and the biquadratic energy were found to also play an important role [21] giving rise to unique behavior. Fcc stacked Fe/Ir(111) displays a square nanoskyrmion lattice with a very small distance of about 1 nm between the skyrmion centers in a large range of external magnetic field [0 T, 9 T] [62]. Fig. 2.3 Ia shows the atomic magnetic configuration and Fig. 2.3 Ib,Ic display measurement results obtained with a spin-polarized scanning tunneling microscope. The nanoskyrmion lattice is linked to the un-

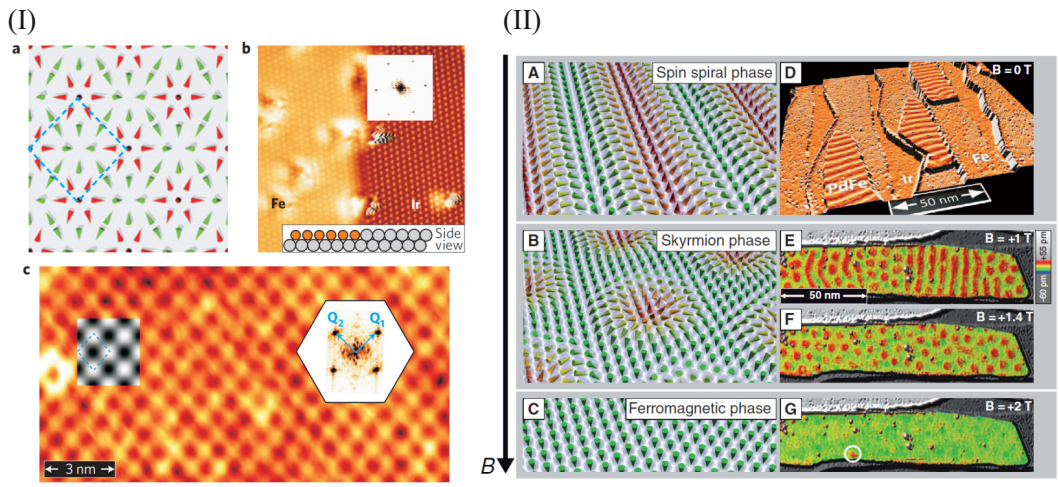

Figure 2.3: Magnetic states of Fe/Ir(111) and Pd/Fe/Ir(111). Figure (I) reprinted by permission from Macmillan Publishers Ltd: [NATURE PHYSICS] (Ref. [21], url), copyright (2011). Figure (II) from Ref. [22], url , reprinted with permission from AAAS. (I) Fe/Ir(111). (**a**) Sketch of the nanoskyrmion lattice. (**b**) Image obtained with a scanning tunneling microscope. (**c**) Image with magnetic contrast on the nanoskyrmion lattice obtained with a spin-polarized scanning tunneling microscope. (II) Pd/Fe/Ir(111). (**A-C**) Sketches of the different magnetic phases which can be obtained as a function of an applied external magnetic field. (**D-G**) Corresponding experimental images with magnetic contrast obtained with a spin-polarized scanning tunneling microscope at 8 K.

derlying atomic lattice in such a way that a diagonal of the square magnetic unit cell is parallel to a close-packed atomic row. Thus, it can appear in one of three rotational domains with respective angles of 120°. In chapter 6 of this thesis, experimental and theoretical observations of confinement effects of the nanoskyrmion lattice in constricted geometries are discussed.

The second experimentally found ultrathin film system in which magnetic skyrmions can be stabilized is Pd/Fe/Ir(111). The properties of this system are quite different from the ones of the previously introduced Fe/Ir(111). Pd/Fe/Ir(111) can indeed be described by an effective Hamiltonian which takes only an exchange and Dzyaloshinskii-Moriya interaction and an anisotropy energy into account [57] and is in this respect very close to the initial theoretical proposal of magnetic skyrmions [10, 11, 12]. In zero magnetic field, spin-spiral states as shown in Fig. 2.3 IIA, IID with spin-spiral periods of $6-7\,\mathrm{nm}$ were observed at temperatures below about $10\,\mathrm{K}$ [22]. The dependence of the spin-spiral period on the energy parameters is discussed in chapter 5 of this thesis. Qualitatively speaking, the period decreases with an increasing ratio of D/J. Magnetic skyrmions are formed in the presence of an external magnetic field which is oriented perpendicular to the surface of the magnetic system (Fig. 2.3 IIB, IIE,IIF). In contrast to the nanoskyrmions in Fe/Ir(111), the skyrmions form a close-packed lattice with a six-fold symmetry at intermediate magnetic fields. A large magnetic field aligns the magnetic moments parallel to its direction and isolated magnetic skyrmions exist as metastable excitations (Fig. 2.3 IIC, IIG). Their size shrinks with an increasing magnetic field [57]. This is in good agreement with theoretical calculations that show a decrease of the skyrmion size with an increasing magnetic field for skyrmions within the skyrmion lattice and isolated skyrmions [63].

2.3 Transition theory

This section provides an introduction to the available theoretical tools that can be used to describe activated escape behavior of a system from a local energy minimum. Furthermore, it is discussed how the existing models apply to the circumstances of skyrmionic materials.

The first generally accepted description of activated transition behavior was

the Arrhenius equation

$$k = A \cdot \exp\left(-E/RT\right) \tag{2.8}$$

that describes the temperature dependence of the rate constant k of a chemical reaction in which an activation energy E has to be overcome on the molecular level in order to be executed. A is a pre-exponential factor and R the gas constant. It is highly non-trivial to calculate the pre-exponential factor and there is a lot of theoretical work dealing with this issue. For example, it can be shown that the pre-exponential factor can be expressed in the regime of large damping as

$$A = \frac{\omega\omega'}{2\pi\zeta} \tag{2.9}$$

with the damping coefficient ζ [64]. The frequencies ω and ω' originate from an approximation of the potential well of the initial state and the energy barrier with potentials of harmonic oscillators. In other words, if ω is large the system will oscillate quickly back and forth in its potential well and attempt to overcome the energy barrier often.

Furthermore, there are various extensions of the Arrhenius equation and a famous one was developed by Henry Eyring [65] who described the reaction rate of a chemical process by

$$k = \kappa \frac{k_\mathrm{B} T}{h} \exp\left(\Delta S/R\right) \exp\left(-\Delta H/RT\right) \tag{2.10}$$

according to Ref. [66] with the Planck constant h. ΔS and ΔH provide the entropy and energy differences when going from the potential well to the transition state. This model allows to additionally obtain an insight into the entropy changes during chemical reactions. The coefficient κ is a transmission coefficient which takes into account the possibility that not all activated complexes give rise to products [66].

These descriptions of transition rates are not only suitable for chemical reactions but can be generalized and applied in various different situations. In order to give an example related to magnetic materials, Néel and Brown

discussed that the reversal of the magnetization of a magnetic particle over an internal anisotropy energy barrier E can be described in a corresponding way [67, 68]. Therein, the pre-exponential factor is called attempt frequency which is associated with the frequency of the gyromagnetic precession [69]. That is the frequency with which a magnetic moment precesses around an external magnetic field.

For skyrmionic magnetic bulk systems, C. Schütte and A. Rosch showed in Ref. [70] that the creation and destruction of skyrmions is driven by singular magnetic defects, so called Bloch points, that can be considered as emergent magnetic monopole and antimonopole pairs whose creation rate is in agreement with eq. 2.8. Further discussions of such Arrhenius-like activated skyrmion creation and annihilation can be found in Ref. [71, 72, 73]. In Ref. [22], N. Romming *et al.* demonstrated the possibility to decisively trigger transitions between ferromagnetic skyrmionic states by means of the current of a spin-polarized scanning tunneling microscope. In view of these findings, the assumption of an energy landscape similar to the one depicted in Fig. 2.4 and corresponding lifetimes τ_{Sk} and τ_{FM} of the skyrmionic and ferromagnetic sates

$$\tau_{\mathrm{Sk}} = \langle \nu_0^{\mathrm{Sk}\to\mathrm{FM}} \rangle^{-1} \cdot \exp\left(E_{\mathrm{a}}^{\mathrm{Sk}}/k_{\mathrm{B}}T\right) \tag{2.11}$$

$$\tau_{\mathrm{FM}} = \langle \nu_0^{\mathrm{FM}\to\mathrm{Sk}} \rangle^{-1} \cdot \exp\left(E_{\mathrm{a}}^{\mathrm{FM}}/k_{\mathrm{B}}T\right) \tag{2.12}$$

with the attempt frequencies ν_0 and activation energies E_{a} are justified. In this picture, the configurations that the system passes through during a transition process are parametrized by a so-called reaction coordinate γ. This model will be used in chapter 4. Studies that dealt with the determination of the reaction

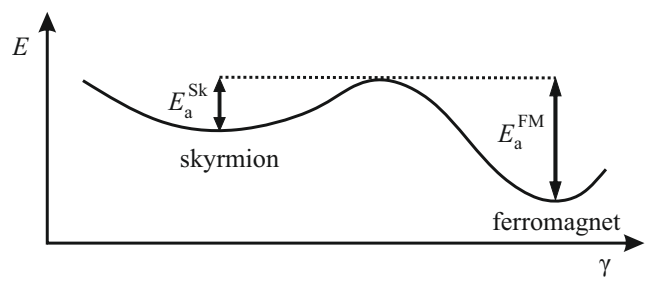

Figure 2.4: Energy landscape. Sketch of the potential wells of the skyrmion state and ferromagnetic state as a function of a reaction coordinate γ.

coordinate suggest that transitions between skyrmion state and ferromagnetic state take place via axisymmetric spin configurations [74, 75, 76]. However, it could not be excluded that strongly non-axisymmetric solutions play a role.

Chapter 3

Methods

3.1 Statistical mechanics

Methods of statistical mechanics are used to derive macroscopic properties of systems with a large number of particles from the physical principles governing the behavior on the microscopic scale. Examples for these many particle systems are gases, fluids and solids for which it is impossible and in general also unnecessary to solve the vast number of equations of motion for the individual particles. Instead, a statistical approach is used to derive important properties as the specific heat, the magnetic susceptibility or the electric conductivity. The key definitions are the ones of the *microstate* and *macrostate*. A microstate is defined by a complete set of coordinates and momenta for all the particles of a system. In contrast, the macrostate is given by macroscopic properties as e.g. the energy, volume and the temperature. A macrostate is characterized by a set of microstates, the statistical ensemble, which can be occupied with certain probabilities. For the Monte Carlo calculations within this work, the systems have been investigated within the canonical ensemble which will be introduced in the following.

Canonical ensemble

The canonical ensemble describes systems which are in contact with a heat bath keeping it at a fixed temperature T. The probability to find the system in the microstate r with the energy E_r is

$$p_r = \exp\left(-\frac{E_r}{k_\mathrm{B}T}\right)/Z \tag{3.1}$$

where Z is the canonical partition function which is given due to the normalization condition

$$\sum_r p_r = 1 \tag{3.2}$$

as

$$Z = \sum_r \exp\left(-\frac{E_r}{k_\mathrm{B}T}\right) \tag{3.3}$$

Then, the expectation value for a macroscopic property like the magnitude of the magnetization $M = |\mathbf{M}|$ is given by

$$\langle M \rangle = \sum_r p_r(T) \cdot M_r \tag{3.4}$$

with M_r being the magnetization of the microstate r.

An important quantity is the free energy F

$$F = -k_\mathrm{B}T \ln(Z) \tag{3.5}$$

from which other quantities like the magnetization $\mathbf{M}$, the entropy S, the heat capacity C_H and the susceptibility X_T

$$\mathbf{M} = -\left(\frac{\partial F}{\partial \mathbf{H}}\right)_T \qquad S = k_\mathrm{B}\frac{\partial}{\partial T}(T \ln Z)$$

$$C_H = -T\left(\frac{\partial^2 F}{\partial T^2}\right)_H \qquad X_T = -\frac{1}{V}\left(\frac{\partial^2 F}{\partial H^2}\right)_T$$

can be derived. However, a different description of the heat capacity and the susceptibility are more convenient for the Monte Carlo calculations. They can also be obtained from the fluctuations of the system as

$$C_H = k_\mathrm{B}\beta^2(\langle E^2\rangle - \langle E\rangle^2) \qquad X_T = \beta(\langle M^2\rangle - \langle M\rangle^2) \tag{3.6}$$

in which the heat capacity is determined by fluctuations in the energy and the susceptibility by fluctuations within the magnetization. The quantities $\langle E^2\rangle$ and $\langle E\rangle^2$ are proportional to the square of the particle number N while the relative fluctuation of the energy is small $\propto 1/N$ [77]. These fluctuations are typically too small to be detected in experiments but they can be observed in Monte Carlo calculations. The same applies for the fluctuations in the magnetization.

3.2 Monte Carlo

Monte Carlo (MC) methods are used in various fields of studies to find approximate solutions in cases where analytical approaches fail or are too inconvenient. With regard to statistical mechanics, they can be employed to obtain approximate values for thermodynamic properties of a given system by performing a random walk in phase space. A method to elegantly perform this random walk in phase space is the famous Metropolis algorithm which will be used in the course of this work. In the following, the general theory of the generation of random states of a system is discussed. Thereafter, the Metropolis algorithm is introduced.

3.2.1 Transition theory

Master equation

A system with the microstates n and the corresponding time dependent occupation probabilities $w_n(t)$ is considered. The dynamics of the system can be described by the master equation

$$\frac{\partial w_n(t)}{\partial t} = -\sum_m \left[w_n(t)\mathcal{T}(n \to m) - w_m(t)\mathcal{T}(m \to n)\right] \tag{3.7}$$

with $\mathcal{T}(n \to m)$ being the transition probability from state n to state m. In thermal equilibrium, the occupation probabilities $w_n(t)$ are time independent

and hence the left side of the equation becomes zero. The choice of the *detailed balance* condition

$$w_n(t)\mathcal{T}(n \to m) = w_m(t)\mathcal{T}(m \to n) \tag{3.8}$$

trivially ensures an according vanishing of the right side of the equation. This is a sufficient but not a necessary condition [78]. Moreover, the time independent probabilities w_n are chosen to be equivalent to the Boltzmann probabilities p_n. Within a MC method, the transition probability is typically a product of the probability to create a new test state $\mathcal{C}(n \to m)$ and the probability for the acceptance of this state $\mathcal{A}(n \to m)$.

$$\mathcal{T}(n \to m) = \mathcal{C}(n \to m) \cdot \mathcal{A}(n \to m) \tag{3.9}$$

When the creation of a new test configuration is a symmetric process, one finds $\mathcal{C}(n \to m) = \mathcal{C}(m \to n)$. Equation 3.8 yields

$$\frac{\mathcal{A}(n \to m)}{\mathcal{A}(m \to n)} = \frac{p_m}{p_n} = \exp[-\beta(E_m - E_n)] \tag{3.10}$$

as a condition for the choice of the acceptance probabilities. This is fulfilled by the Metropolis algorithm which is presented in the following section.

Markov chain

A Markov chain is a stochastic process that produces succeeding states of a system. From a current state n of the system, a random new state m is generated with the transition probability $\mathcal{T}(n \to m)$. Most important, the transition probabilities don't depend on the previous states and hence on the history of the system. Of course, the normalization condition

$$\sum_m \mathcal{T}(n \to m) = 1 \tag{3.11}$$

has to be fulfilled. The Metropolis algorithm provides a method to generate new configurations of a system in such a way. For a system consisting of multiple magnetic moments on a discrete lattice, the sequence of states simulate artificial dynamics.

3.2.2 Metropolis algorithm

Usually, a summation over all energy states is necessary to obtain the canonical partition function and thereby the full information about a system. Analytically, this can be impossible for large systems with many degrees of freedom. The Metropolis algorithm [79] is a powerful tool that avoids the problem of the determination of the partition function and directly calculates approximate values of thermodynamical properties as for example the heat capacity. It is based on the finding that random configurations of a system can be generated weighted with the corresponding Boltzmann probability without the need of the partition function. Therefore, having generated a large amount of random states $\{i\}$, an approximate value $\overline{Q}$ for the expectation value $\langle Q \rangle$ of a quantity Q is obtained as an arithmetic mean

$$\overline{Q} = \frac{1}{n} \sum_{i=1}^{n} Q_i \approx \sum_r Q_r \exp\left(-\frac{E_r}{k_\mathrm{B}T}\right) / Z = \langle Q \rangle \tag{3.12}$$

with n being the number of values of Q obtained during a Monte Carlo calculation.

The Metropolis algorithm consists of the two steps:

- Make a random trial change on the system and calculate the resulting energy difference ΔE.
- Accept the new configuration with the probability $p = \min\{1, \exp(-\beta \Delta E)\}$.

These steps are repeated multiple times. Here, $\beta = 1/k_\mathrm{B}T$. This algorithm provides a very efficient method to minimize the energy because energetically more favorable trial states ($\Delta E < 0$) will always be accepted. Energetically more unfavorable trial states ($\Delta E > 0$) are accepted with a value smaller one according to a Boltzmann factor. This choice of acceptance probabilities is in compliance with eq. 3.10. For the course of this thesis, a Monte Carlo step is defined as N random trial changes with N being the number of magnetic moments of the considered system.

The Metropolis algorithm is used to describe the behavior of magnetic moments on discrete sites of a lattice. The directions of the magnetic moments are given by vectors $\mathbf{S}_i \in \mathbb{R}^3$ of unit length. A trial change on the system

is done by choosing a lattice site and a random new direction for the corresponding magnetic moment. There are multiple ways to generate such a new direction. The first one that was used for this work is called the uniform spin sampling. Three random numbers S_x, S_y, S_z are chosen uniformly distributed in the interval [-1,1]. If the resulting vector lies outside of the unit sphere, a new set of random values will be created. If the resulting vector lies within the unit sphere, the vector will be projected onto the surface of the unit sphere and accepted as a new trial direction for the magnetic moment at the chosen lattice site. This method of producing new random spin directions ensures a uniform distribution on the surface of the unit sphere. The second method to create a new random direction is the Gaussian spin sampling method [80]. Here, normal distributed variations are added to the current spin direction at a random lattice site. Three values s_x, s_y, s_z are created according to the normal distribution $\mathcal{N}(0, \sigma^2)$. Then, the new direction $\mathbf{S}_i^*$ of a current magnetic moment $\mathbf{S}_i$ is determined as

$$\mathbf{S}_i^* = \frac{\mathbf{S}_i + \mathbf{s}_{\mathcal{N}(0,\sigma^2)}}{|\mathbf{S}_i + \mathbf{s}_{\mathcal{N}(0,\sigma^2)}|} \tag{3.13}$$

with

$$\mathbf{s}_{\mathcal{N}(0,\sigma^2)} = \begin{pmatrix} s_\mathrm{x} \\ s_\mathrm{y} \\ s_\mathrm{z} \end{pmatrix} \tag{3.14}$$

The Gaussian sampling method is useful when relatively smooth spin trajectories are desired. This can be practical for a system close to the equilibrium state at low temperatures in order to fine-tune the orientations of the magnetic moments. For most of the MC calculations presented in this work, the uniform sampling method was used. In cases where the Gaussian sampling method was employed, it is noted explicitly.

3.3 Lattices and boundary conditions

All results from Monte Carlo calculations that are shown in the course of this thesis were performed on two-dimensional hexagonal lattices with vari-

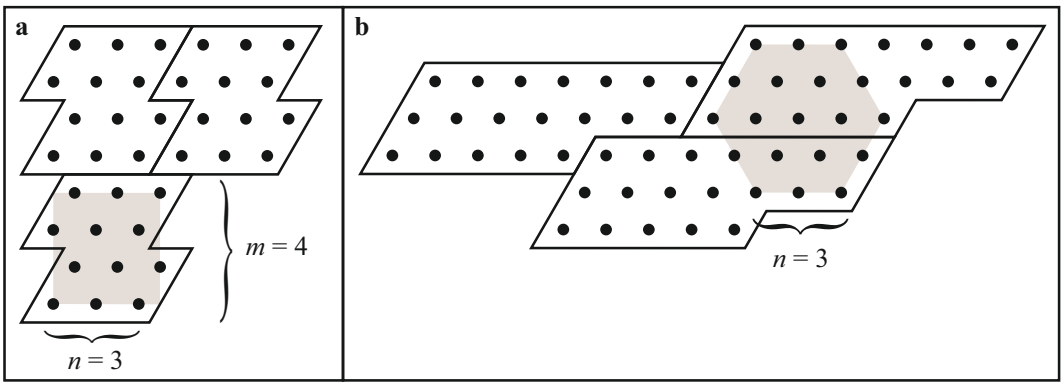

Figure 3.1: Boundary conditions. (**a**) Periodic boundary conditions for a hexagonal lattice with an overall rectangular boundary shape. One side coincides with a close-packed row. (**b**) Construction of helical boundary conditions for a hexagonal lattice with an overall hexagonal boundary shape as shown in (**c**).

ous sizes and boundary shapes as well as different boundary conditions. The choice of system size and boundary conditions depends strongly on the purpose of a calculation. Some investigations of this thesis explicitly deal with the effects of boundaries onto the magnetic ground states of skyrmionic materials. The orientation of spin-spirals with respect to the edge of a magnetic island is discussed in chapter 5 and the alignment of the nanoskyrmion lattice in Fe/Ir(111) with respect to an edge is the focus of chapter 6. However, influences due to finite system sizes can be undesired in other situations as for example when studying phase transitions. Phase transitions only occur in the thermodynamic limit for infinite systems that obviously can not be considered in computer calculations because of limited memory and processing time. Hence, a method called finite size scaling based on the changes observed when varying the system size can be used for this purpose. Apart from this, periodic boundary conditions can be used to reduce boundary effects. At the boundary of a system, the lattice sites have a reduced number of nearest neighbors and the idea is to connect lattice sites at opposite sides of the system in order to fill up the missing number of neighbors. The exact method depends on the lattice type and for the hexagonal lattices shown in this thesis, two different methods were used. First, a hexagonal lattice with an overall rectangular boundary shape similar to the one shown in Fig. 3.1a is considered. It consists of m rows of n lattice sites and the periodic boundary conditions can be found by

a periodic repetition of the lattice. This choice can be problematic in certain cases since the boundary shape has a different symmetry than the lattice itself and another method to set boundary conditions in which the boundary shape resembles the symmetry of the lattice is convenient. For this purpose, a hexagonal lattice with a hexagonal boundary shape is considered and so called helical boundary conditions [99] are set up in the way indicated in Fig. 3.1 b. Each "edge" consists as depicted of n sites which results in a total number of lattice sites

$$N = 3n^2 - 3n + 1 \quad . \tag{3.15}$$

This type of lattice is used for the Monte Carlo calculations regarding the stability properties of a single skyrmion in chapter 4 because the hexagonal boundary shape is closer to the axisymmetric shape of a skyrmion than a rectangular boundary. Besides this, skyrmions typically form a close packed lattice when they are not in the diluted phase.

3.4 Phase transitions and finite size effects

Materials can typically exist in different phases depending on external parameters as e.g. the temperature and a magnetic field. This can concern for example their state of aggregation (e.g. solid, fluid and gaseous) or also their magnetic order (e.g. ferromagnetic and paramagnetic). The following discussion will focus on phase transitions of magnetic materials but applies in a similar way to other material systems.

Phases are described by a suitable order parameter and their exact choice depends on the considered system, e.g. the magnetization for a ferromagnet. A phase transition is characterized by a change of the order parameter. For a ferromagnet, the magnetization is zero above a critical temperature T_c and unequal to zero below T_c. This change in the magnetization is continuous and hence the phase transition is called continuous. At T_c, the correlation length ξ diverges. For a ferromagnet, the correlation length provides the size of clusters in which the magnetic moments are parallel. The divergence of the correlation length leads to a divergence in the susceptibility X [64] that can be used to

determine the position of the phase transition. However, the divergence occurs in the thermodynamic limes of infinite systems, only. For finite systems, the correlation length is limited by the system size and hence the susceptibility has a finite value at the critical temperature. This means that, strictly speaking, no phase transition occurs in finite systems. Still, the susceptibility exhibits a peak which is interpreted as a phase transition within this work. Besides of the susceptibility, the specific heat capacity provides an alternative quantity that may exhibit a divergence at a phase transition. Also here, a peak instead of a divergence can be obtained for finite system sizes.

Typically, the position $T_\mathrm{c}(L)$ of the peak for a finite system of size L is not identical with the position T_c of the divergence for an infinite system [81, 82]. *D. P. Landau* found using two-dimensional and three-dimensional Ising lattices that the difference $T_\mathrm{c} - T_\mathrm{c}(L)$ for the specific heat is small for systems with periodic boundary conditions, but may be significant for small systems with open boundary conditions [83, 84]. Here, $T_\mathrm{c}(L)$ is shifted to smaller temperatures.

3.5 Topological charge

Here, the concept of the topological charge Q in the context of magnetic skyrmions is presented. It proves to be a very useful order parameter since it gives the number of skyrmions within a magnetic system. It is typically defined via

$$Q = \frac{1}{4\pi} \int_A \mathbf{m} \cdot \left(\frac{\partial \mathbf{m}}{\partial x} \times \frac{\partial \mathbf{m}}{\partial y} \right) \mathrm{d}x\mathrm{d}y \tag{3.16}$$

as an integral over a magnetic surface A whose local direction of magnetization is described by the continuous field $\mathbf{m}$. For a spin-spiral state or the ferromagnetic state, the topological charge is equal to zero since the coordinate system can be chosen in such a way that the spatial derivative of the magnetization is zero in at least one spatial direction. For a single skyrmion, the local magnetization directions cover the whole surface of the unit sphere and consequently the integral is equal to the surface area of the unit sphere. Hence, an integer number is obtained by the division of 4π. For discrete magnetic models, the

integral needs to be replaced by a sum as described in Ref. [85, 86]. In the following, this process will be explained for a system of magnetic moments $\mathbf{S}_i$ on a hexagonal lattice. Therein, the magnetic moments are arranged at the corners of equilateral triangles. For each set of three magnetic moments on these triangles, the solid angle Ω is determined via

$$\Omega = 2 \cdot \mathrm{atan2}(N, D) \tag{3.17}$$

$$N = \mathbf{S}_1 \cdot (\mathbf{S}_2 \times \mathbf{S}_3) \tag{3.18}$$

$$D = \mathrm{S}_1\mathrm{S}_2\mathrm{S}_3 + (\mathbf{S}_1 \cdot \mathbf{S}_2)\mathrm{S}_3 + (\mathbf{S}_1 \cdot \mathbf{S}_3)\mathrm{S}_2 + (\mathbf{S}_2 \cdot \mathbf{S}_3)\mathrm{S}_1 \tag{3.19}$$

as shown in Ref. [86]. The order of the arguments of the atan2 function is consistent with the definition of the Fortran function ATAN2. Then, the integral can be replaced by the sum over the solid angles of all triangles.

3.6 Random telegraph signal

Random telegraph noise usually refers to temporal resistance fluctuations in small devices that show random switching between two or several discrete values. This was experimentally observed e.g. for metal oxide semiconductor field-effect transistors (MOSFETs) [87] and Cu nanobridges [88]. Similar behavior has been found for various systems as for example for magnetic nanoislands whose magnetization direction can spontaneously be reversed due to thermal agitation [89, 90, 91]. This effect is known as superparamagnetism.

In chapter 4 of this thesis, stochastic switching between ferromagnetic and skyrmionic states of a magnetic system is discussed. The obtained two-level process is characterized by the Dzyaloshinskii-Moriya interaction and skyrmion number as a function of the Monte Carlo step. The Dzyaloshinskii-Moriya interaction provides a random telegraph signal that is used to obtain the mean times spent in ferromagnetic or skyrmionic states between two succeeding switching events.

3.6.1 Determination of switching events

In the following, the method used to identify the switching processes between the skyrmionic and ferromagnetic states is presented. For this purpose, the DM

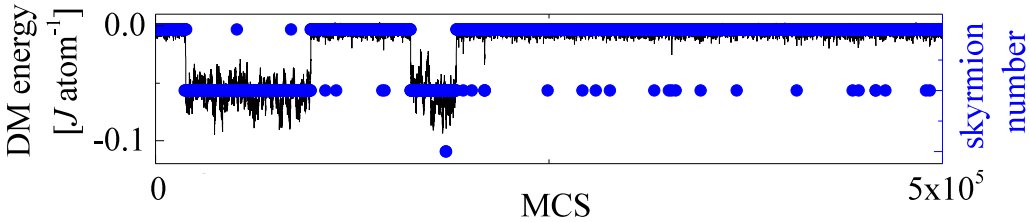

Figure 3.2: DM energy and skyrmion number. The DM energy and the corresponding skyrmion number as a function of the time given in MC steps for $k_{\mathrm{B}}T = 0.61\,J$ and $\mu B = 0.103\,J$ revealing a two state behavior due to the ongoing creation and annihilation of a single skyrmion.

energy and the skyrmion number (see section 3.5) were calculated as a function of the Monte Carlo step as shown exemplarily in Fig. 3.2 for $k_{\mathrm{B}}T = 0.61\,J$ and $\mu B = 0.103\,J$ for a magnetic system with a hexagonal lattice with 631 lattice sites as investigated in chapter 4. The DM energy exhibits a two level behavior while the skyrmion number adopts discrete natural number values between zero and two for these parameters within this range of MCS. The skyrmion number switches predominantly between zero and one corresponding to the two levels in the DM energy. However, local fluctuations add or remove topological charge to the skyrmion number without any visible corresponding

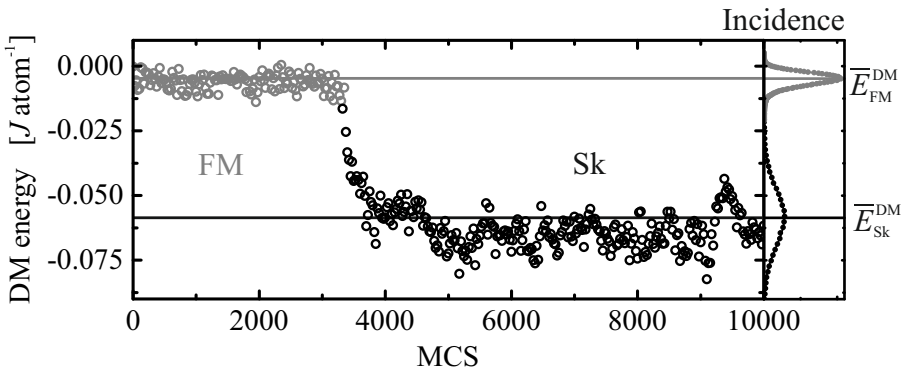

Figure 3.3: Identification of a switching event. DM energy as a function of the time given in MC steps for $k_{\mathrm{B}}T = 0.61\,J$, $\mu B = 0.103\,J$ exhibiting a two state behavior due to the ongoing creation and annihilation of a single skyrmion. The frequency distribution of the DM energies exhibits two peaks whose positions $\overline{E}_{\mathrm{FM}}^{DM}$ and $\overline{E}_{\mathrm{Sk}}^{\mathrm{DM}}$ are marked by the gray and black horizontal lines. A switching event is identified by the coincidence when the DM energy subsequently crosses these two energies as a function of the Monte Carlo step.

changes in the DM energy. Consequently, these fluctuations are neglected when determining the total number of skyrmions within the system and it is more convenient to choose the DM energy to identify switching events since it is less sensitive to local fluctuations. The frequency distribution of the DM energy at a particular temperature and magnetic field exhibits two peaks at $\overline{E}_{\mathrm{FM}}^{\mathrm{DM}}$ and $\overline{E}_{\mathrm{Sk}}^{DM}$ corresponding to the FM and Sk states as shown in Fig. 3.3. The switching events are identified by finding the coincidences at which the DM energy subsequently crosses the energies $\overline{E}_{\mathrm{FM}}^{\mathrm{DM}}$ and $\overline{E}_{\mathrm{Sk}}^{\mathrm{DM}}$ in either order as a function of the Monte Carlo step. Fig. 3.3 shows a switching event from the ferromagnetic to the skyrmionic state, i.e. the DM energy subsequently crosses $\overline{E}_{\mathrm{FM}}^{\mathrm{DM}}$ and $\overline{E}_{\mathrm{Sk}}^{\mathrm{DM}}$.

3.6.2 Determination of lifetimes

For a random telegraph signal with the two levels 0 and 1, the number of switching events within a given time interval is Poisson distributed and hence the time τ between two switching events can be described by an exponential distribution of the type

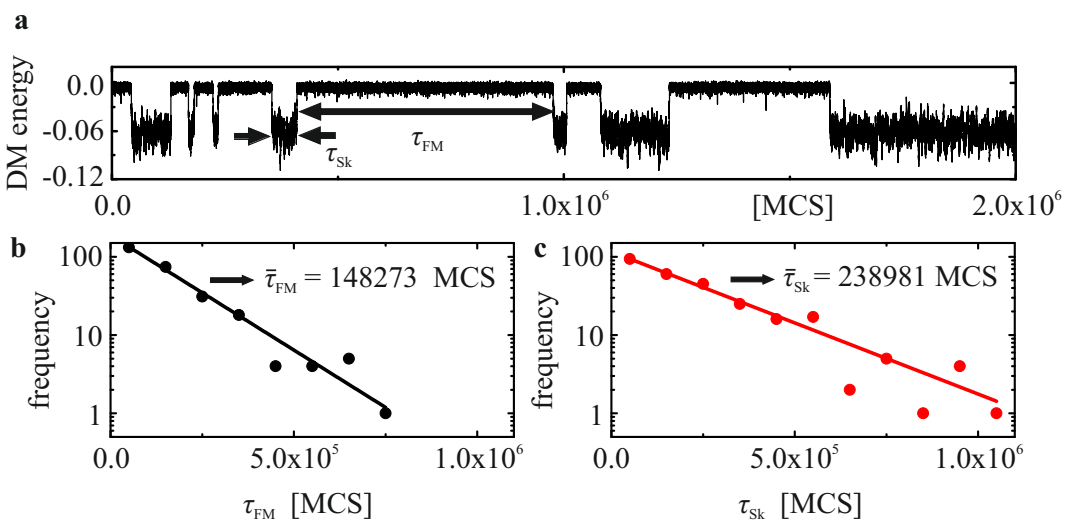

Figure 3.4: Lifetime analysis. (**a**) DM energy as a function of the Monte Carlo step for $\mu B = 0.1\,J$ and $k_{\mathrm{B}}T = 0.61\,J$. (**b**, **c**) Lifetime histograms of the telegraph signal shown in (a) for the ferromagnetic state and skyrmionic state. Exponential fits yield the mean lifetimes $\overline{\tau}_{\mathrm{FM}}$ and $\overline{\tau}_{\mathrm{Sk}}$.

$$P_{0,1}(\tau) = \frac{1}{\overline{\tau}_{0,1}} \exp(-\frac{\tau}{\overline{\tau}_{0,1}}) \quad . \tag{3.20}$$

Therein, $\overline{\tau}_0$ and $\overline{\tau}_1$ are average time constants of the two levels and $P_0(\tau) \cdot d\tau$ and $P_1(\tau) \cdot d\tau$ provide the probabilities that the system remains in state 0 and 1 for the time τ and then switches to the respective other level in the time interval $[\tau, \tau + d\tau]$ [92].

Having identified the switching events between ferromagnetic and skyrmionic states using the Dzyaloshinskii-Moriya energy as a function of the Monte Carlo step, the times τ_{FM} and τ_{Sk} (see Fig. 3.4 a) that the system stays in either of the two states between two succeeding switching events can easily be determined. Figures 3.4 b and 3.4 c show the histograms of τ_{FM} and τ_{Sk} which were obtained from the analysis of the Dzyaloshinskii-Moriya energy for 10^8 Monte Carlo steps at $\mu B = 0.1\,J$ and $k_{\mathrm{B}}T = 0.61\,J$. Exponential fits provide the mean lifetimes $\overline{\tau}_{\mathrm{FM}} = 148273\,\mathrm{MCS}$ and $\overline{\tau}_{\mathrm{Sk}} = 238981\,\mathrm{MCS}$ according to equation 3.20. These values are close to the arithmetic means

$$\frac{1}{n}\sum_{i=1}^{n} \tau_{\mathrm{FM},i} = 143224\,\mathrm{MCS} \qquad \frac{1}{n}\sum_{i=1}^{n} \tau_{\mathrm{Sk},i} = 220087\,\mathrm{MCS} \quad . \tag{3.21}$$

3.7 Spin-polarized tunneling current

In section 7.2.6, the possibility to manipulate the lateral position of a magnetic skyrmion by means of a spin-polarized current injected from a magnetic tip of a scanning tunneling microscope is discussed. In the following, the theoretical concepts that give rise to the incorporation of a spin-polarized current into the Monte Carlo calculations are presented while detailed information about scanning tunneling microscopy can be found elsewhere as e.g. in Ref. [93].

The tunneling current I of a spin-polarized scanning tunneling microscope can be separated into an unpolarized part I_0 and a polarized part I_P with

$$I(\mathbf{R}_T, V, \theta) = I_0(\mathbf{R}_T, V) + I_P(\mathbf{R}_T, V, \theta) \tag{3.22}$$

as shown by Wortmann *et. al.* in Ref. [94]. Therein, θ denotes the angle enclosed by the tip magnetization and sample magnetization, and $\mathbf{R}_T$ and

V are the tip position and the bias voltage between tip and sample. The unpolarized part of the tunneling current was initially described by *J. Tersoff* and *D.R. Hamann* in Ref. [95]. They made the assumption that the work function ϕ of the tip is equal to that of the surface leading to the decay constant $\kappa = \hbar^{-1}(2m\phi)^{1/2}$ for the electronic wave functions of tip and sample. The tip apex was modeled with spherically symmetric s waves. The result was an unpolarized tunneling current which depends exponentially on the distance between tip and sample. However, this part of the current is not of interest for the simulations presented in this thesis and will consequently be neglected.

Stapelfeldt et. al. suggested in Ref. [96] that the spin-polarized part of the tunneling current can be accounted for within simulations by an additional contribution

$$H_T = -g \sum_i \mathbf{T}_i \cdot \mathbf{S}_i \tag{3.23}$$

$$\mathbf{T}_i = -T_0 \cdot P \cdot \mathbf{m}_{\text{tip}} \exp\left(-2\kappa r_i\right) \tag{3.24}$$

to the total Hamiltonian. P is the polarization of the tip magnetization $\mathbf{m}_{\text{tip}}$, T_0 the spin-polarized current averaged over the surface unit cell, r_i is the distance between tip and sample atom i and g is a coupling constant. Obviously, the influence of the spin-polarized current decreases exponentially with an increasing distance between tip and sample which is in agreement with the considerations by *J. Tersoff* and *D.R. Hamann* in Ref. [95]. Apart from that, the Hamiltonian is consistent with the Hamiltonian $H_{\text{sd}} = -J_{\text{sd}}\mathbf{S} \cdot \mathbf{s}$ of the s-d model which describes the interaction of local magnetic moments $\mathbf{S}$ given by localized d electrons with a conduction electron spin density $\mathbf{s}$ of s electrons [97]. The model originates from investigations of the interaction between conduction electrons in a non-magnetic metal with localized magnetic moments of impurity atoms [98]. Therefore, one can not expect precise results in the context of s electrons and d electrons within a magnetic material. However, it captures an important effect that arises when a spin-polarized current flows through a material with spatially inhomogeneous magnetic order. The conduction electrons rotate to follow the local magnetization direction and in order to obey angular momentum conservation, the local magnetic structure experiences a torque which is also known as spin transfer torque.

In the context of spin-polarized scanning tunneling microscopy, the spin-polarized s electrons are the electrons tunneling between magnetic tip and magnetic sample. The interaction takes place with the localized electron states of the sample.

Chapter 4

Stability of skyrmionic bits

For this chapter, lifetimes of skyrmionic and ferromagnetic states were calculated with the Monte Carlo program as a function of temperature and external magnetic field. The Arrhenius law is used for the determination of energy barriers and attempt frequencies which provide an insight into the shape of the underlying energy landscape of the investigated skyrmionic system.

The results are compared to experimental results obtained by Niklas Romming with a spin-polarized scanning tunneling microscope. A procedure is proposed that permits the determination of effective material parameters and the quantification of the Monte Carlo time scale from the comparison of theoretical and experimental data.

Results of this chapter are part of the following publication:

J. Hagemeister, N. Romming, K. von Bergmann, E.Y. Vedmedenko & R. Wiesendanger. Stability of single skyrmionic bits. Nat. Commun. **6** 8455 (2015).

4.1 Simulation parameters and simulation scheme

4.1.1 Model Hamiltonian and system properties

For the sake of generality, an ultrathin magnetic film with the standard effective Hamiltonian

$$H = -J \sum_{<i,j>} \mathbf{S}_i \cdot \mathbf{S}_j - \sum_{<i,j>} \boldsymbol{D}_{i,j} \cdot (\mathbf{S}_i \times \mathbf{S}_j) + K \sum_i \sin^2(\Theta_i) - \mu \sum_i \boldsymbol{B} \cdot \mathbf{S}_i \tag{4.1}$$

is considered. Therein, $\mathbf{S}_i = \boldsymbol{\mu}_i/\mu$ is a three-dimensional magnetic moment of unit length, K describes an uniaxial perpendicular magnetic anisotropy and $\boldsymbol{B}$ is a uniform external magnetic field. J is the effective nearest-neighbor exchange integral and $\boldsymbol{D}_{i,j}$ is an effective nearest-neighbor Dzyaloshinskii-Moriya coupling. For symmetry reasons, the DM-vector $\boldsymbol{D}_{i,j}$ is chosen to be perpendicular to the vector connecting two spins $\mathbf{S}_i$ and $\mathbf{S}_j$ and to lie within the plane of the magnetic film [58]. Systems consisting of up to 1000 Heisenberg spins on a two-dimensional triangular lattice with a hexagonal boundary shape (Fig. 4.1) using helical boundary conditions (see Ref. [99] and section 3.3) were investigated by means of extended MC simulations. Energy parameters typical for thin-films showing skyrmionic phases i.e. $D/J \approx 0.32$ and $K \approx 0.07\,J$ were used [100, 101, 102]. Note that D and J provide energies per bond throughout this chapter.

A typical phase diagram of a thin film skyrmionic system described by the equation (4.1) can be found elsewhere [15, 103, 104]. In order to summarize, the system exhibits a spin-spiral state in zero field within a certain range of the energy parameters at low temperatures. A perpendicular magnetic field can be used to cause a transition from the spin-spiral state to a skyrmionic (Sk) state. In a sufficiently large field, the system becomes fully polarized and transforms into the ferromagnetic (FM) state. The simulations have been performed at fields and temperatures near the phase boundary separating the ferromagnetic and skyrmionic phases where individual skyrmions are formed. In this region of the phase space, the distance between skyrmions is much larger than the skyrmion diameter and the energies of the skyrmionic and

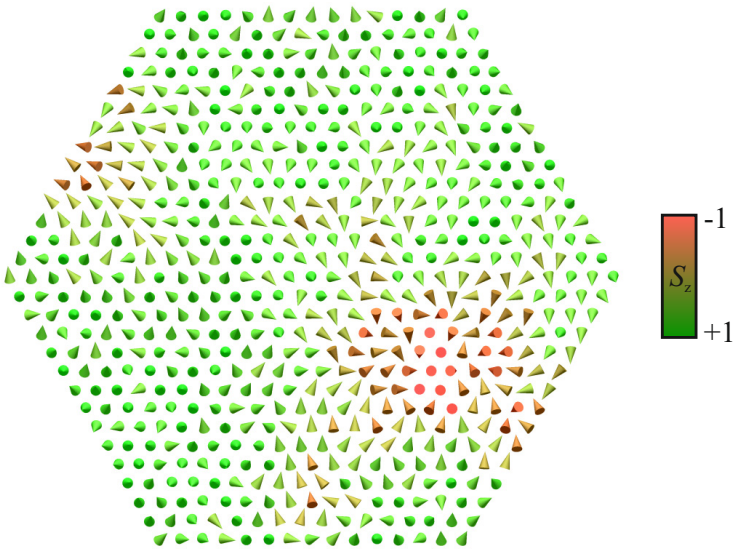

Figure 4.1: Model system. A triangular spin lattice consisting of 631 sites with a hexagonal boundary shape and helical boundary conditions containing a thermally excited single skyrmion at $k_\mathrm{B}T = 0.61\,J$ and $\mu B = 0.093\,J$.

the ferromagnetic states are nearly degenerate and a thermally activated creation and annihilation of single skyrmions within the ferromagnetic phase is expected. Indeed, this process can be captured with Monte Carlo simulations allowing for an exploration of the energy landscape of skyrmionic systems as will be discussed in the course of this chapter. The switching between the distinct topological states can be characterized by the skyrmion number which oscillates predominantly between zero and unity and the DM energy which exhibits abrupt changes when a skyrmion is created or annihilated as shown in section 3.6.1 and section 3.6.2. The size of the spin system used for the simulations in this chapter was chosen in such a way that only one single skyrmion was stochastically created and annihilated within the system near the critical field B_c separating the FM and Sk phases as a function of the time measured in MC steps (see section 4.1.2).

4.1.2 Choice of System Size

The total number of skyrmions that can be present in the system simultaneously depends on the system size N and consequently, the system size has an influence on the stability of an individual skyrmion. Figure 4.2 shows the

mean lifetimes of the FM state and an individual skyrmion as a function of the system size for $k_{\mathrm{B}}T = 0.61\,J$ and $\mu B = 0.1\,J$. The system was restricted to geometries with a hexagonal boundary shape leaving only certain possible values for N. The red and black points mark the mean lifetimes for the values of N that comply with this constriction. The system can contain a maximum of one skyrmion for relatively small system sizes $N < 800$. In the range $500 < N < 800$ the single skyrmion is the more probable state compared to the ferromagnet. For system sizes $N < 500$ this stability relation is inverted and the ferromagnet is the more probable state. This behavior may be ascribed to two effects. Firstly, the skyrmion is restricted to a smaller region with a reduction of the system size providing less space to evade local perturbations. Secondly, the system eventually becomes too small to allow the formation of a whole skyrmion. In systems larger than $N \approx 800$, multiple skyrmions may be present within the system at the same time. In order to study the stability properties of an individual skyrmion, the system size of $N = 631$ was chosen which is close to the region allowing for multiple skyrmions.

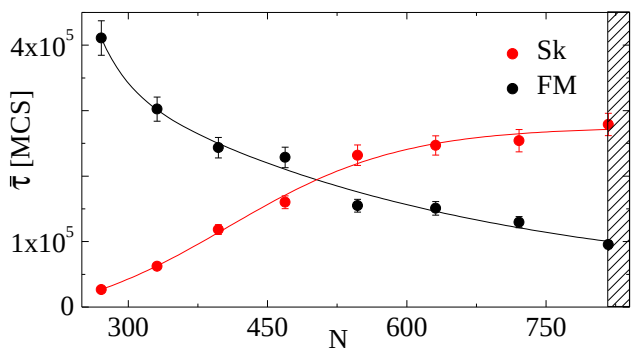

Figure 4.2: Dependence of the lifetimes on the system size. The mean lifetimes $\overline{\tau}_{\mathrm{FM,Sk}}$ as a function of the number of lattice sites N for $k_{\mathrm{B}}T = 0.61\,J$ and $\mu B = 0.1\,J$. Since triangular lattices with a hexagonal boundary shape are considered, certain values of N are possible only. The red and black points mark the mean lifetimes for the values of N that comply with this constriction. The shaded area to the right side marks the region in which the system size is large enough to allow two skyrmions to be present simultaneously. For the calculations presented in the following within this chapter, $N = 631$ was chosen in order to study the stability properties of a single skyrmionic bit.

4.2 Lifetimes and energy landscape

Fig. 4.3 a shows the DM energy as a function of the MC time at three different magnetic fields for the temperature $k_{\mathrm{B}}T = 0.61\,J$. While the system is found with equal probabilities in the Sk and FM states at the critical field of $\mu B_{\mathrm{c}} = 0.103\,J$, the Sk state becomes preferred for fields $B < B_{\mathrm{c}}$ as shown for $\mu B_1 = 0.093\,J$. This population imbalance gets inverted in the range $B > B_{\mathrm{c}}$ at which the FM state becomes more stable as shown for $\mu B_2 = 0.114\,J$.

Fig. 4.3 b shows the histograms of the DM energies which exhibit two peaks corresponding to the FM and Sk states. The peaks of the Sk states are much broader than those of the FM, which may be ascribed to thermally induced fluctuations in the skyrmion size. Additionally, the peak of the Sk state shifts to higher energies with an increasing field indicating that the skyrmion equilibrium size decreases with the field [12]. As the probability to find the system in either state is equivalent to the area underneath the peaks, the areas are equal for both states at B_{c} only. The mean lifetimes $\overline{\tau}_{\mathrm{Sk}}$ and $\overline{\tau}_{\mathrm{FM}}$ cannot be deduced directly from the histograms but are rather determined as $\sum_{i=1}^{N}(\tau_{\mathrm{FM,i/Sk,i}})/N$ (see section 3.6.2) from the individual lifetimes $\tau_{\mathrm{Sk,i}}$ and

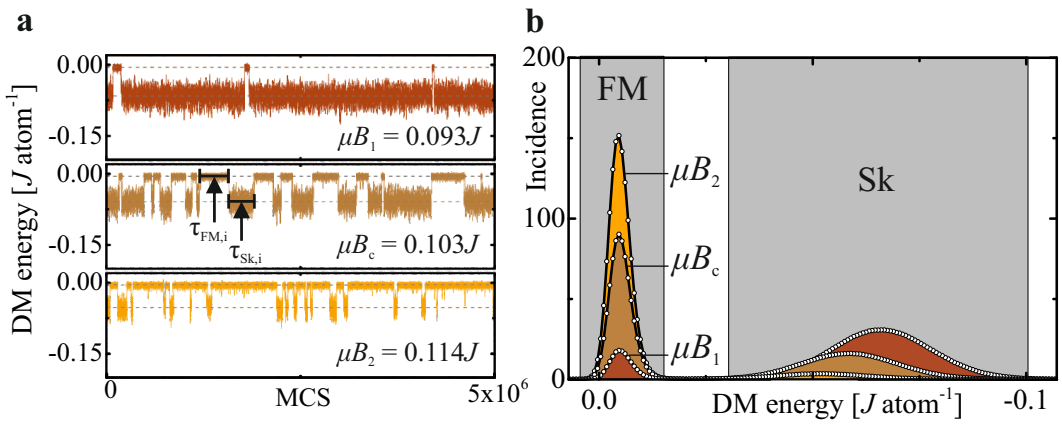

Figure 4.3: Thermally induced creation and annihilation of a single skyrmion. (**a**) The DM energy as a function of the Monte Carlo step for different magnetic fields at $k_{\mathrm{B}}T = 0.61\,J$ exhibiting a two-state behavior due to the ongoing creation and annihilation of a single skyrmion. (**b**) The histogram of the DM energy shows two peaks corresponding to the FM and Sk states. The Sk and FM states are populated with equal probability at the critical field B_{c} and the areas underneath the peaks of the histogram are equal.

$\tau_{\mathrm{FM,i}}$ shown in Fig. 4.3 b. For this purpose, more than $N = 1000$ switching events have been recorded for each set of temperature and field to achieve reliable statistics. Fig. 4.4 a shows the effect of both the magnetic field and the temperature on the mean lifetimes within the range $\mu B = (0.093 - 0.114)\,J$ and $k_{\mathrm{B}}T = (0.6 - 0.7)\,J$. The red points give $\overline{\tau}_{\mathrm{Sk}}$ and the black points $\overline{\tau}_{\mathrm{FM}}$ as determined from the MC calculations. For a fixed temperature, the skyrmionic state gets destabilized by an increasing field and, therefore, the mean lifetime of a skyrmion decreases. The ferromagnetic state, in contrast, gets stabilized and the corresponding mean lifetime increases. Surprisingly, the mean lifetimes exhibit a very asymmetric behavior with respect to the intersection point $(B_{\mathrm{c}}, \overline{\tau}_{\mathrm{c}})$ showing that the Sk and FM states respond differently to changes in the magnetic field. Such an asymmetry can appear for several reasons including field dependent changes in the activation energy, in the energies of the Sk and FM states or in the dynamics.

In order to clarify this behavior, particular attention has to be paid to the

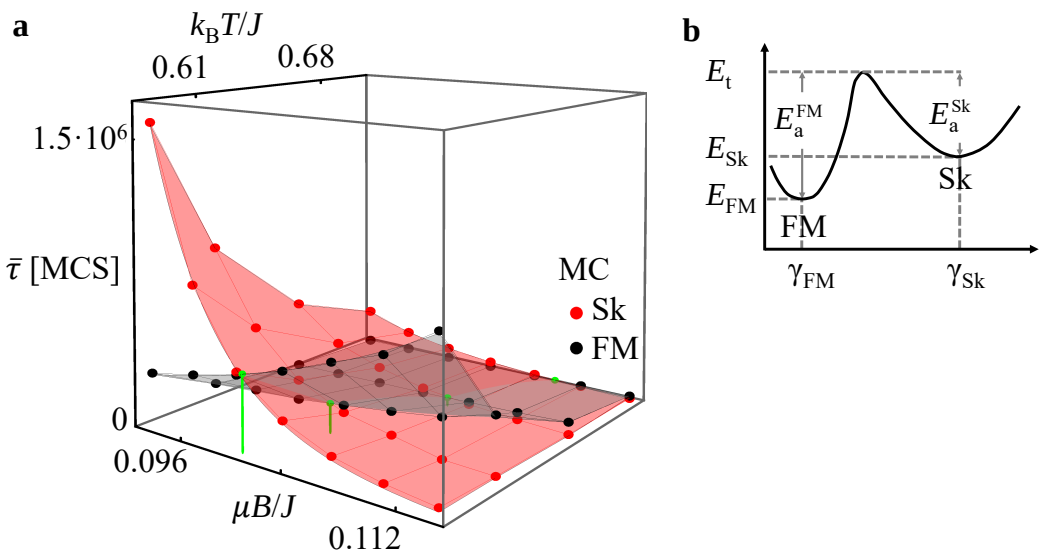

Figure 4.4: Lifetimes as a function of temperature and magnetic field. (**a**) Mean lifetimes of the Sk and FM states as a function of the magnetic field and the temperature. The red and black points are the results of MC calculations. The points of intersection $(B_{\mathrm{c}}, \overline{\tau}_{\mathrm{c}})$ are marked by green spheres. B_{c} increases linearly with T in this temperature range. (**b**) A sketch of the energy landscape with the energy minima E_{Sk} and E_{FM} of the Sk and FM states which are separated by activation energies given by $E_{\mathrm{a}}^{\mathrm{Sk}}$ and $E_{\mathrm{a}}^{\mathrm{FM}}$.

shape of the energy landscape and its dependence on the magnetic field. As a starting point, a simplified one-dimensional energy landscape (Fig. 4.4 b) is considered with two energy minima E_{Sk} and E_{FM} of the Sk and FM states, which are separated by an energy barrier giving rise to the two activation energies $E_{\mathrm{a}}^{\mathrm{Sk}}$ and $E_{\mathrm{a}}^{\mathrm{FM}}$. The reaction coordinate γ describes the spin configurations between the two energy minima. The field dependencies of E_{FM} and E_{Sk} can immediately be derived from the MC calculations and are shown in Fig. 4.5 a for the temperature $k_{\mathrm{B}}T = 0.61\,J$. Both energies decrease linearly with the field. This behavior is evident for the FM because of its direct Zeeman proportionality but is less trivial for the Sk state. The FM state is energetically favored over the Sk state over the full range of investigated fields. A linear extrapolation of E_{FM} and E_{Sk} to smaller fields yields a degeneracy at $\mu B = 0.065\,J$, yet the skyrmion is more stable ($\overline{\tau}_{\mathrm{Sk}} > \overline{\tau}_{\mathrm{FM}}$) for $\mu B < 0.103\,J$.

The energy of the separating barrier is more difficult to access because the intermediate spin configurations are yet unknown. However, $E_{\mathrm{a}}^{\mathrm{FM}}$ and $E_{\mathrm{a}}^{\mathrm{Sk}}$ can be derived from the temperature dependence of the mean lifetimes which are found to decrease exponentially with the temperature allowing to describe them with the Arrhenius-law by the functions

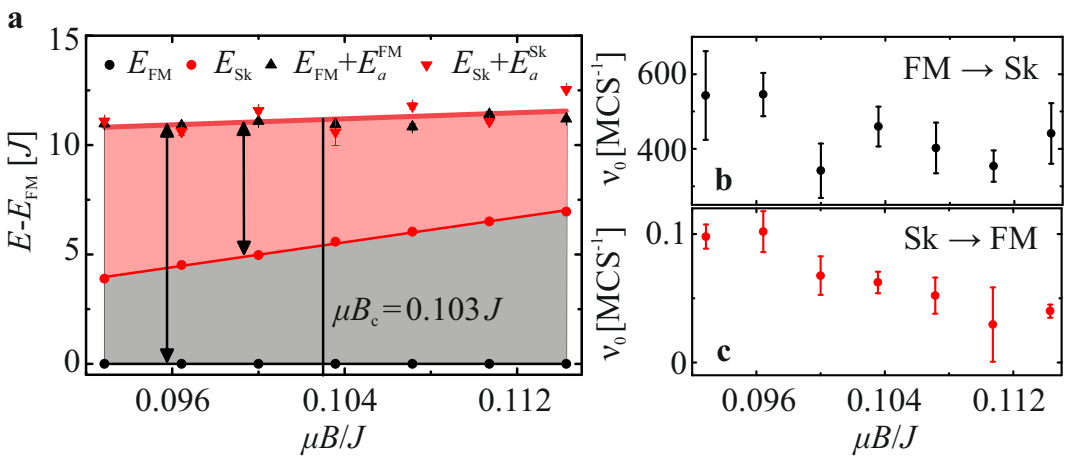

Figure 4.5: Activation energies and attempt frequencies. (**a**) The energies E_{Sk} and E_{FM} of the Sk and FM states as a function of the magnetic field for the temperature $k_{\mathrm{B}}T = 0.61\,J$ alongside with the energy of the transition state E_{t} (Fig. 4.4 b) which is given by the sum of the energy levels and the corresponding activation energies. (**b**, **c**) The attempt frequencies ν_0.

$$\overline{\nu}_0^{\mathrm{FM}} = \frac{1}{\overline{\tau}_0^{\mathrm{FM}}} = \nu_0^{\mathrm{FM}\to\mathrm{Sk}} \cdot \exp(-\frac{E_{\mathrm{a}}^{\mathrm{FM}}}{k_{\mathrm{B}}T}) \tag{4.2}$$

$$\overline{\nu}_0^{\mathrm{Sk}} = \frac{1}{\overline{\tau}_0^{\mathrm{Sk}}} = \nu_0^{\mathrm{Sk}\to\mathrm{FM}} \cdot \exp(-\frac{E_{\mathrm{a}}^{\mathrm{Sk}}}{k_{\mathrm{B}}T}) \tag{4.3}$$

with the attempt frequencies $\nu_0^{\mathrm{FM}\to\mathrm{Sk}}$ and $\nu_0^{\mathrm{Sk}\to\mathrm{FM}}$. The activation energies derived from fits of numerical data by equations (4.2, 4.3) correspond to the vertical heights of the shaded areas in Fig. 4.5 a. $E_{\mathrm{a}}^{\mathrm{Sk}}$ and $E_{\mathrm{a}}^{\mathrm{FM}}$ both depend linearly on the magnetic field. $E_{\mathrm{a}}^{\mathrm{Sk}}$ decreases from $7.4\,J$ to $4.7\,J$ in the investigated field range while $E_{\mathrm{a}}^{\mathrm{FM}}$ increases only slightly and is about $11\,J$. The observation that $E_{\mathrm{a}}^{\mathrm{Sk}}$ responds more sensitive to changes in the field than $E_{\mathrm{a}}^{\mathrm{FM}}$ may be explained by the fact that the magnetic microstructure of the ferromagnetic state remains unchanged (up to fluctuations) with increasing field strength, while the size of an isolated skyrmion shows a strong field dependence [12]. A similar activated behavior as described by equation (4.3) with a comparable value for $E_{\mathrm{a}}^{\mathrm{Sk}}$ was found for bulk skyrmionic systems [70].

The energy of the barrier state E_{B} is given by the sums of the energies of the FM and Sk states and the corresponding activation energies as $E_{\mathrm{B}}^1 = E_{\mathrm{FM}} + E_{\mathrm{a}}^{\mathrm{FM}}$ and $E_{\mathrm{B}}^2 = E_{\mathrm{Sk}} + E_{\mathrm{a}}^{\mathrm{Sk}}$. The energies E_{B}^1 and E_{B}^2, shown by the black and red triangles in Fig. 4.5 a, coincide within the range of numerical accuracy indicating that the system passes the same barrier state for both transition directions justifying the one-dimensional picture of the energy landscape.

Summing up, it is found that for fields $B < B_{\mathrm{c}}$ the Sk state is more stable than its ferromagnetic counterpart despite the fact that it is still energetically less favorable. Also, the activation energy of the Sk is smaller than that of the FM in this range. Thus, the intrinsic energy and most unexpectedly the activation energy cannot be the dominating mechanism stabilizing the skyrmion. In order to shed light onto this finding, the attempt frequencies have been investigated. From the Arrhenius fit one finds that the attempt frequencies are on the order of $\nu_0^{\mathrm{Sk}\to\mathrm{FM}} \approx 0.05\,\mathrm{MCS}^{-1}$ and $\nu_0^{\mathrm{FM}\to\mathrm{Sk}} \approx 400\,\mathrm{MCS}^{-1}$ throughout the whole range of explored magnetic fields (Fig. 4.5 b). This large discrepancy can be ascribed to the attempt frequencies as the reason for the stability of the Sk state for fields $B < B_{\mathrm{c}}$ in the present MC calculations. These data also imply that the energy minimum of the Sk state is broader than that of the FM state since the attempt frequencies describe in a first approximation the geometry of the energy landscape in the vicinity of the energy minima.

4.3 Comparison with experiment

The calculations presented above concern a generic two-dimensional skyrmionic system which can effectively be described by a Hamiltonian of equation (4.1). In the following, the numerical findings are compared with experimental results obtained for Pd/Fe/Ir(111) [22]. The experimental investigations on Pd/Fe/Ir(111) were performed at a temperature of 4.2 K with a spin-polarized scanning tunneling microscope (SP-STM) using a Cr-bulk tip. The system exhibits a spin-spiral state at zero magnetic field at low temperatures. In a perpendicular magnetic field, the system adapts a two-level behavior: only skyrmionic and ferromagnetic configurations remain stable [22]. The temperature is such that the thermal energy alone is insufficient to go from the FM to the Sk state at moderate field values between 2.5 T and 4.5 T. Instead, the additional energy from the spin-polarized tunnel current is needed to overcome the energy barrier and to reach the other energy minimum. Single skyrmions that are pinned to atomic defects in the ferromagnetic phase were observed at fields of 3.5 T − 4 T. Within this field range, using a spin-polarized tunnel current $I = 100\,\mathrm{nA}$ and an applied voltage of $U = \pm 600\,\mathrm{mV}$ a stochastic switching between the Sk and the FM states was induced and the corresponding telegraph signal in the differential conductance has been recorded [22].

In order to justify a comparison between these experimental data and the present MC-calculations, particular attention has to be paid to the origin of the excitations leading to the spontaneous switching between the two states. In standard MC-simulations the system under investigation is in equilibrium with a thermal bath, which is described by the energy E_b being an essential part of the Boltzmann probability $p_\mathrm{B} = e^{-E_\mathrm{i}/E_\mathrm{b}}$. The exact origin of E_b is never addressed and is traditionally attributed to the thermal energy $E_\mathrm{b} = k_\mathrm{B}T$. In the present experimental system the spontaneous switching between the two states is not purely induced by thermal energy. Instead, the dominant mechanism was found to be the injection of additional energy due to tunneling electrons from the tip of a SP-STM [22]. Here, it is assumed that the MC temperature includes both thermal and electronic excitations. Note also that the experiments were performed on skyrmions located at local atomic defects which were neglected within the MC simulations.

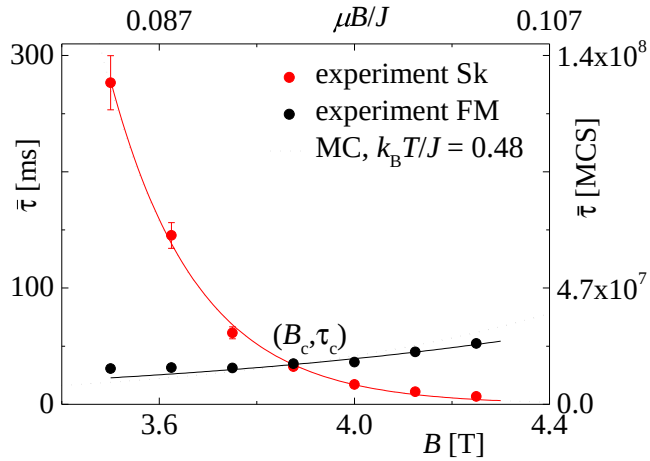

Figure 4.6: Lifetimes from Monte Carlo simulations and experiments on Pd/Fe/Ir(111). Mean lifetimes obtained from experiments on Pd/Fe/Ir(111) as a function of the magnetic field B in combination with mean lifetimes obtained from MC calculations. The MC data is linearly rescaled to the experimental data such that the critical points given by $(B_c, \overline{\tau}_c)$ coincide. The lifetimes are described by exponential functions $\overline{\tau}_{\mathrm{FM/Sk}}(B) \propto \exp(\lambda_{\mathrm{FM/Sk}} B)$.

Fig. 4.6 shows experimentally obtained mean lifetimes of the Sk and FM states as a function of B for the bias voltage of $U = -600\,\mathrm{mV}$. The functions show a very good qualitative agreement with the theoretically obtained data of Fig. 4.4 a. In agreement with the MC data, the lifetimes are strongly asymmetric with respect to the critical field $B_c \approx 3.9\,\mathrm{T}$ at which the lifetimes are equal. This finding allows us to compare the experimental and MC mean lifetimes. More than that, the MC results can be calibrated using the experimental data by linearly rescaling $\overline{\tau}^{\mathrm{MC}}_{\mathrm{FM/Sk}}(B)$ in such a way that the MC intersection point $(B_c^{\mathrm{MC}}, \overline{\tau}_c)$ coincides with that found experimentally. Now, the task remains to determine the correct MC temperature at which the field dependent mean lifetimes best fit to the experimental data. In order to find the required MC temperature, $\overline{\tau}_{\mathrm{FM/Sk}}(B)$ were described by exponential functions of the form

$$\overline{\tau}_{\mathrm{FM/Sk}} \propto \exp(\lambda_{\mathrm{FM/Sk}} B) \tag{4.4}$$

with the fit parameters $\lambda_{\mathrm{FM/Sk}}$ as proposed in Ref. [70] for the Sk state. The horizontal black and red lines in Fig. 4.7 a show the values $\lambda_{\mathrm{FM}}^{\mathrm{exp}}$ and $\lambda_{\mathrm{Sk}}^{\mathrm{exp}}$ obtained from fits to the experimental data. The thickness of these lines gives

the uncertainty. For the MC data, the values $\lambda^{\mathrm{MC}}_{\mathrm{FM/Sk}}$ depend on the MC temperature and are shown by the red and black dashed lines in Fig. 4.7 a. The curves $\lambda^{\mathrm{exp}}_{\mathrm{Sk}}$ and $\lambda^{\mathrm{MC}}_{\mathrm{Sk}}$ intersect at $k_{\mathrm{B}}T = 0.48\,J$, while no intersection can be observed for $\lambda^{\mathrm{exp}}_{\mathrm{FM}}$ and $\lambda^{\mathrm{MC}}_{\mathrm{FM}}$ within the explored MC temperature range. Seemingly, the best agreement between experiment and MC simulations is obtained for the MC temperature $k_{\mathrm{B}}T \approx 0.48\,J$. Note that for $k_{\mathrm{B}}T < 0.58\,J$, the MC mean lifetimes were extrapolated from the temperature dependent calculations because of insufficient MC statistics in direct simulations. The feasibility of the proposed calibration method has been confirmed by the calculation of the Sk probability $p_{\mathrm{Sk}}(B) = \overline{\tau}_{\mathrm{Sk}}(B)/(\overline{\tau}_{\mathrm{Sk}}(B) + \overline{\tau}_{\mathrm{FM}}(B))$ (Fig. 4.7 b) which is 0.5 at the critical field B_{c} and approaches 1 for small and 0 for large fields. The experimentally and numerically determined curves show a good agreement.

From the correspondence between the experimental and the MC time at B_{c} the physical time scale is immediately set as $2 \cdot 10^{-9}$ s per MC step. From the knowledge of the experimental B_{c}, the MC field is derived by the scaling factor $B^{\mathrm{exp}}_{\mathrm{c}}/B^{\mathrm{MC}}_{\mathrm{c}}$. Taking the magnetic moment $\mu = 3\,\mu_{\mathrm{B}}$ for Pd/Fe/Ir(111) [100] into account, all coupling constants can naturally be determined. According to the described calculations the nearest-neighbor effective exchange interaction for Pd/Fe/Ir(111) equals $J = (7 \pm 0.2)$ meV per bond (or 3.5 meV per atom), while the DM parameter is $D = 2.2$ meV per bond (or 1.1 meV per atom).

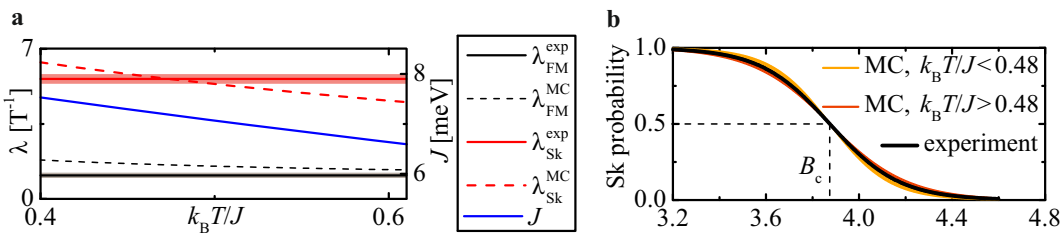

Figure 4.7: Calibration of MC results with experimental data obtained on Pd/Fe/Ir(111). (**a**) The fit parameter $\lambda_{\mathrm{FM/Sk}}$ (Fig. 4.6) for the experimental data (exp) and MC data (MC). The values $\lambda^{\mathrm{MC}}_{\mathrm{FM/Sk}}$ depend on the MC temperature used. The best correspondence between experiment and MC is found using the MC temperature $k_{\mathrm{B}}T \approx 0.48\,J$ marked by the vertical gray line. The calibration of the MC mean lifetimes at this temperature with the experimental lifetimes provide an absolute value for the exchange parameter of $J = (7.1 \pm 0.2)$ meV. (**b**) The skyrmion probability $p_{\mathrm{Sk}}(B) = \overline{\tau}_{\mathrm{Sk}}(B)/(\overline{\tau}_{\mathrm{Sk}}(B) + \overline{\tau}_{\mathrm{FM}}(B))$.

These values are close to the effective interaction parameters given in Ref. [100, 102]. From the considerations above, the activation energies between single skyrmions and the ferromagnetic phase in Pd/Fe/Ir(111) are on the order of $E_{\mathrm{a}}^{\mathrm{Sk}} \approx 35\,\mathrm{meV} - 50\,\mathrm{meV}$ and $E_{\mathrm{a}}^{\mathrm{FM}} \approx 80\,\mathrm{meV}$ at the temperature $k_{\mathrm{B}}T = 0.48\,J$. This is somewhat smaller than activation barriers observed for nanoscale Fe/W islands of comparable size [91] (≈ 100 atoms) to the skyrmions.

The overall good agreement suggests that the present MC simulations are suited to describe skyrmionic systems and capture the physics of the creation and annihilation of individual skyrmions.

4.3.1 Stability bounds of skyrmions in Pd/Fe/Ir(111)

Using the results of the MC simulations, the dependence of the mean lifetime $\overline{\tau}_{\mathrm{c}} = \overline{\tau}_{\mathrm{FM}}(B_{\mathrm{c}}) = \overline{\tau}_{\mathrm{Sk}}(B_{\mathrm{c}})$ at the critical field B_{c} can be derived as a function of the inverse temperature $J/k_{\mathrm{B}}T$ finding an exponential dependence as shown in Fig. 4.8. The data points were obtained from the field and temperature dependent mean lifetimes presented in Fig. 4.4 a. Considering a constant magnetic field, the mean lifetimes $\overline{\tau}_{\mathrm{Sk}}(T)$ and $\overline{\tau}_{FM}(T)$ exhibit an Arrhenius-like dependence on the temperature as discussed in the previous section. The exponential fit functions approximating the temperature dependent mean lifetimes $\overline{\tau}_{\mathrm{Sk}}(T, B)$ and $\overline{\tau}_{FM}(T, B)$ at a specific field ($B = \mathrm{const.}$) intersect in $(T_{\mathrm{c}}, \overline{\tau}_{\mathrm{c}})$. This is shown exemplarily in the inset of Fig. 4.8 for the magnetic field $\mu B = 0.093\,J$. The point of intersection $(T_{\mathrm{c}}, \overline{\tau}_{\mathrm{c}})$ at which $\overline{\tau}_{\mathrm{Sk}} = \overline{\tau}_{FM} = \overline{\tau}_{\mathrm{c}}$ is marked by a black circle and can be found again in the graph of the main panel. The other data points in the main panel were found in the same way by the intersections of $\overline{\tau}_{\mathrm{Sk}}(T)$ and $\overline{\tau}_{FM}(T)$ at other magnetic fields. This procedure is possible because the point of intersection depends on the magnetic field, i.e. $(T_{\mathrm{c}}(B), \overline{\tau}_{\mathrm{c}}(B))$. The numerical results are quantified by the experimental data for Pd/Fe/Ir(111) as discussed in the previous section providing absolute energy and time scales for the MC simulation. With this correspondence, one can derive that the skyrmionic and ferromagnetic states are stable on the order of years at the critical field B_{c} for temperatures lower than 19 K. Furthermore, the mean lifetimes are smaller than 50 µs for temperatures larger than about 60 K which provides an estimate for the critical temperature of the system. In Monte Carlo calculations using energy parameters obtained from

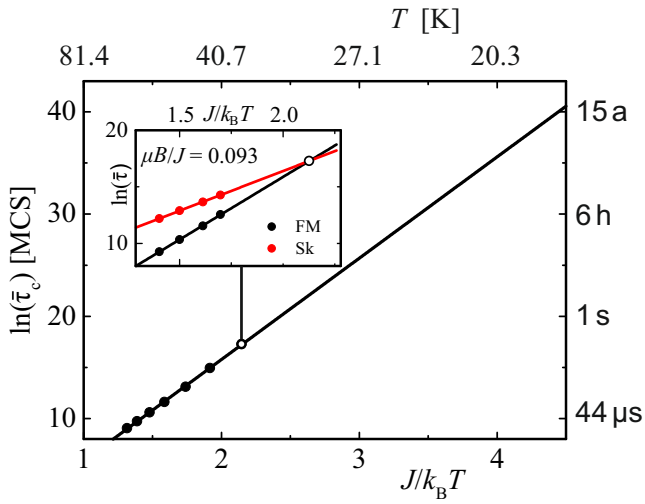

Figure 4.8: Temperature dependence of $\overline{\tau}_c$. The mean lifetime $\overline{\tau}_c = \overline{\tau}_{FM}(B_c) = \overline{\tau}_{Sk}(B_c)$ as a function of the inverse temperature J/k_BT obtained from MC simulations. A temperature lower than 19 K is needed to achieve mean lifetimes on the order of years in the system Pd/Fe/Ir(111).

density function calculations, a transition temperature of about 100 K was reported [73].

Thus, a device on the basis of this material will be able to operate at the temperature of liquid He only. In order to increase the operation temperature the activation energies need to be larger while leaving the D/J ratio constant. It can be speculated that this can be achieved by coherent increase of both energy parameters by e.g. using multilayers in order to increase the number of nearest-neighbors and at the same time the number of interfaces which are necessary for a strong DM coupling. From Fig. 4.8, one observes that the value of $J/k_BT = 2.43$ corresponds to a lifetime of approximately $1s$. If this lifetime is desired at room temperature of 300 K an exchange constant of approximately 63 meV is needed. Therefore, a material with an even larger exchange constant has to be used for technological applications where lifetimes on the order of years are required.

4.4 Entropy

In the following, the entropy of the skyrmionic system investigated in this chapter is calculated and a connection to the temperature dependence of the

critical field B_c is found.

Ezawa estimated in Ref. [105] the entropy of an extended thin magnetic film exhibiting skyrmions and used it to derive a phase diagram spanned by temperature and an external magnetic field. Particularly, the critical magnetic field separating skyrmionic and ferromagnetic phases was found to increase with the temperature due to a higher entropy of the skyrmion phase. A similar behavior for the critical field B_c is observed for the present system as shown in Fig. 4.9. Ezawa calculated the entropy of the extended system adapting at maximum N skyrmions by using the formula for n subset-element combinations $N!/n!(N-n)!$. Hence, skyrmions were treated as an ensemble of quasiparticles.

In the present investigation, a single skyrmion is an extended object with internal degrees of freedom. Therefore, another approach for the estimation of the entropy for the system discussed in this chapter is needed.

4.4.1 Entropy from heat capacity

The entropy can be determined from thermodynamic principles based on the heat capacity C similar to Ramirez *et al.* in Ref. [106]. The heat capacity is

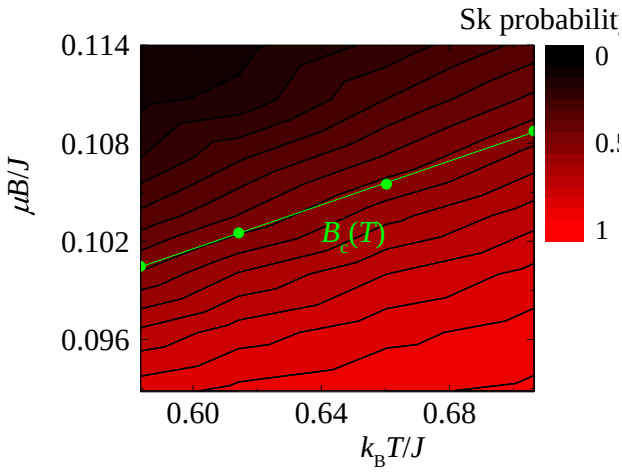

Figure 4.9: Skyrmion probability and critical magnetic field. The critical magnetic field derived from MC simulations as a function of the temperature. The skyrmion probability $\overline{\tau}_{Sk}/(\overline{\tau}_{Sk}+\overline{\tau}_{FM})$ is color coded in red to black.

calculated in the Monte Carlo simulation by

$$C = \frac{< E^2 > - < E >^2}{k_B T^2}$$

as a function of the temperature for various magnetic fields. For a given magnetic field, the temperature was reduced from the paramagnetic disordered state at $k_B T = 6\,J$ to the ordered equilibrium state at $k_B T = 0.01\,J$ in 1000 steps and $2 \cdot 10^4$ Monte Carlo steps were done at each temperature step. Fig. 4.10 a shows the heat capacity as a function of the temperature exemplarily for the magnetic field $\mu B = 0.1\,J$.

The entropy $S(T)$ can then be determined by evaluating the integral

$$S(T) = \int_{T'=0}^{T'=T} \frac{C(T')}{T'} dT.$$

In Monte Carlo simulations one faces the problem that the temperature is always a value greater than zero and therefore, for $k_\mathrm{B} T < 0.58\,J$ the integral cannot be properly evaluated. However, there is access to the entropy difference between a low temperature T_0 and a high temperature T_∞ at which the sample is disordered.

$$\Delta S = \int_{T'=T}^{T'=T_\infty} \frac{C(T')}{T'} dT$$

The total magnetic entropy of N independent quantum spins is known to be $S = R \cdot \ln(2J + 1)$ with J being the total angular momentum. For classical

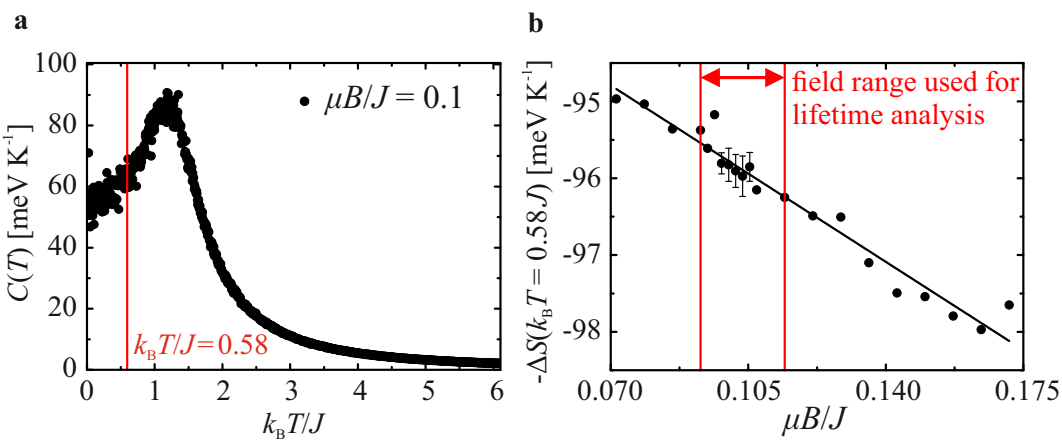

Figure 4.10: Heat capacity and entropy. (**a**) Heat capacity $C(T)$ as a function of the temperature for the magnetic field $\mu B = 0.1J$. (**b**) Entropy difference $-\Delta S$ as a function of the magnetic field.

spin systems this value corresponds to $S = R \cdot \ln 4\pi$ as stated by McMichael *et al.* in Ref. [107]. Hence, the magnetic entropy per spin can reach a maximum of $S/R = \ln 4\pi \approx 2.5$. In the limit of strong interactions this value might be strongly reduced. However, the limit of $\ln 4\pi$ can be assumed as a total spin entropy at an infinite temperature. Hence, while the absolute values of entropy at finite temperatures cannot be obtained, the entropy difference $\Delta S = S(T_\infty) - S(T)$ can be calculated as a function of an external magnetic field. Fig. 4.10 b shows $-\Delta S(k_\mathrm{B}T = 0.58\,J, B)$ in the broad range of magnetic fields for $k_\mathrm{B}T = 0.58\,J$, which lies below the ordering temperature. As one can see from this figure, $\Delta S(B)$ linearly increases with increasing field ($-\Delta S(B)$ linearly decreases). This means that the entropy of the ordered state $S(T, B)$ decreases with increasing field as the total entropy is $S(T, B) = S(T_\infty) - \Delta S$. In other words, the skyrmionic state ($B < B_\mathrm{c}$) possesses a larger entropy than the ferromagnetic state.

Since the influence of the entropy becomes more prominent for higher temperatures, the stability of a skyrmion increases at a given magnetic field with the temperature and hence, $B_\mathrm{c}(T)$ should also increase with the temperature. The entropic contribution due to the formation of a single skyrmion is estimated to be on the order of 0.7 meV/K as the entropy difference between the magnetic fields $B = 1.1B_\mathrm{c}$ and $B = 0.9B_\mathrm{c}$.

4.4.2 Entropy from Eyring equation

The entropy difference as obtained with the help of the heat capacity is in good agreement with considerations using the Eyring equation [65, 66] (see also section 2.3)

$$\nu = \kappa \frac{k_\mathrm{B}T}{h} \exp(\frac{\Delta S}{k_B}) \exp(-\frac{\Delta U}{k_B T}) \tag{4.5}$$

which provides a link between the transition rate ν and the entropy and energy differences ΔS and ΔU going from the initial to the transition state. Applying the Eyring equation to the skyrmionic system, one obtains the attempt frequencies ν_Sk and ν_FM of the Sk and FM states as

$$\nu_{\mathrm{Sk}} = \kappa_{\mathrm{Sk}} \frac{k_{\mathrm{B}} T}{h} \exp(\Delta S_{Sk}/k_B) \exp(-\frac{\Delta U_{Sk}}{k_B T}) \tag{4.6}$$

$$\nu_{\mathrm{FM}} = \kappa_{\mathrm{FM}} \frac{k_{\mathrm{B}} T}{h} \exp(\Delta S_{FM}/k_B) \exp(-\frac{\Delta U_{FM}}{k_B T}) \tag{4.7}$$

At B_c, the transition rates are equal ($\nu_{Sk} = \nu_{FM}$) and therefore

$$\Delta U_{Sk} - \Delta U_{FM} = T(\Delta S_{Sk} - \Delta S_{FM}) - k_{\mathrm{B}} \ln \frac{\kappa_{\mathrm{FM}}}{\kappa_{\mathrm{Sk}}} \tag{4.8}$$

The differences $\Delta U_{Sk} - \Delta U_{FM}$ and $\Delta S_{Sk} - \Delta S_{FM}$ are equal to the differences of the internal energies and entropies of the two states. The energy difference has been found to be $\approx 6\,J$ at B_{c} from Fig. 4.5 a. Considering $\kappa_{\mathrm{FM}} \approx \kappa_{\mathrm{Sk}}$ in a first approximation, this leads to an entropy difference of $\approx 0.9\,\mathrm{meV/K}$ between the FM and Sk states with ($S_{\mathrm{Sk}} > S_{\mathrm{FM}}$) at the temperature $k_B T/J = 0.58$. This is close to the one stated above of $0.7\,\mathrm{meV/K}$. The discrepancy could be a result of the initially neglected term $k_{\mathrm{B}} \ln \kappa_{\mathrm{FM}}/\kappa_{\mathrm{Sk}}$ with $\kappa_{\mathrm{FM}} \approx 10 \cdot \kappa_{\mathrm{Sk}}$. In chemical reactions, κ takes into account the possibility that not all activated complexes give rise to products. In the present context, the interpretation is unclear but one can speculate that κ_{FM} and κ_{Sk} are related to the probabilities that "skyrmion seeds" and "ferromagnet seeds" result in a change of the magnetic state.

4.4.3 Entropy from slope of critical magnetic field

Moreover, a direct link between the dependence of the critical magnetic field as a function of the temperature ($B_{\mathrm{c}}(T)$) and the entropy difference between the Sk and FM states can be shown. From equation (4.8) follows

$$E_{\mathrm{FM}}(B_{\mathrm{c}}, T) - E_{\mathrm{Sk}}(B_{\mathrm{c}}, T) = T(S_{\mathrm{FM}}(B_{\mathrm{c}}, T) - S_{\mathrm{Sk}}(B_{\mathrm{c}}, T)) - k_{\mathrm{B}} \ln \frac{\kappa_{\mathrm{FM}}}{\kappa_{\mathrm{Sk}}} \tag{4.9}$$

with E_{FM}, E_{Sk} and S_{FM}, S_{Sk} the energies and entropies of the FM and Sk states. The difference of the activation energies is equal to the difference of the energies of the FM and Sk states because the transition state is the same for both directions as shown in section 4.2 for the present system.

Differentiating both sides of the equation with respect to the temperature while assuming that the entropy difference is in a first approximation independent of the temperature ($\Delta S(B_\mathrm{c}, T) = S_\mathrm{FM}(B_\mathrm{c}, T) - S_\mathrm{Sk}(B_\mathrm{c}, T)) = \Delta S(B_\mathrm{c})$ yields

$$\frac{\partial}{\partial T}(E_\mathrm{FM} - E_\mathrm{Sk}) = \Delta S(B_\mathrm{c}) \tag{4.10}$$

It is reasonable to assume that the equilibrium size of a skyrmion at the critical field is approximately independent of the temperature. Therefore, the change of difference of the energy levels with the temperature is dominated by the Zeeman energy and hence

$$\frac{\partial}{\partial T}(E_\mathrm{FM} - E_\mathrm{Sk}) \approx \frac{\partial}{\partial T}\Delta E_\mathrm{Z}(B_c) \approx \Delta M_\mathrm{z}\frac{\partial}{\partial T}B_\mathrm{c} \tag{4.11}$$

The difference of the z-component of the magnetization between the two states can be derived from the MC simulations as $\overline{\Delta M}_\mathrm{z} \approx 120\,\mu$. The slope of the change of the critical field with respect to the temperature can be taken from Fig. 4.9 and one obtains

$$|\overline{\Delta M}_\mathrm{z}\frac{\partial}{\partial T}B_\mathrm{c}| \approx 0.7\,\mathrm{meV/K} \tag{4.12}$$

4.4.4 Conclusion

It was shown that different ways lead to similar values within the range of $\approx (0.7 - 0.9)\,\mathrm{meV/K}$ as the entropy difference between the Sk and FM states. Hence, it can be concluded that the skyrmion stability is drastically enhanced by a larger entropy compared to the ferromagnetic state.

4.5 Metastability of states

In this section, the metastability of the ferromagnetic and skyrmionic states as a function of the external magnetic field is discussed. Starting point are curves of the magnetization as a function of an external magnetic field for

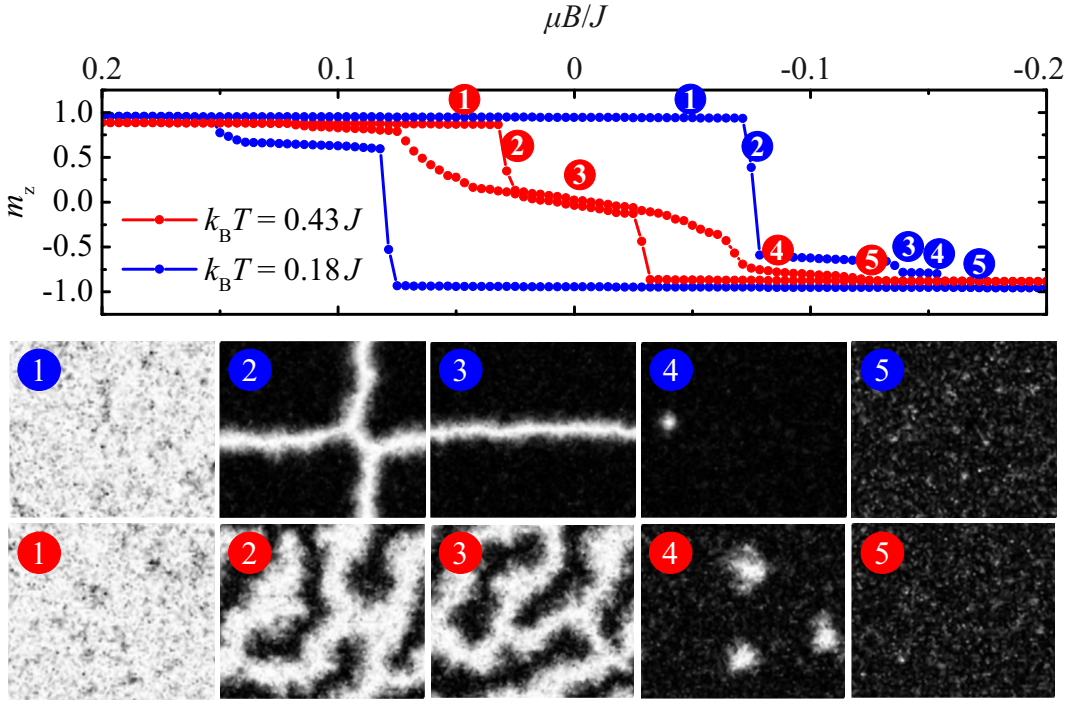

Figure 4.11: Magnetization curves. The mean perpendicular component of the magnetization as a function of the magnetic field for the temperatures $k_{\mathrm{B}}T = 0.43\,J$ and $k_{\mathrm{B}}T = 0.18\,J$. Starting point was a ferromagnetic state. Exemplary configurations of the system are indicated with numbers in the curve.

a hexagonal lattice consisting of 5776 lattice sites with a rectangular boundary shape using periodic boundary conditions. A larger system than before is used for this investigation in order to reduce finite size effects onto the formation of the various magnetic phases. Hysteresis curves of the type shown in Fig. 4.11 are obtained when varying the magnetic field in the range between $\mu B = -2.1\,J$ and $\mu B = +2.1,\,J$ using 121 field steps with 10^5 MC steps each. When decreasing the magnetic field, no transitions from a ferromagnetic to a skyrmionic configuration is found for the temperatures $k_{\mathrm{B}}T = 0.43\,J$ and $k_{\mathrm{B}}T = 0.18\,J$. For the lower temperature, the ferromagnetic state even survives when the direction of the external magnetic field is reversed. In both cases, the ferromagnetic state is followed by spin-spiral like states which can be transformed into one or multiple skyrmions in a magnetic field with a reversed direction. These skyrmions are destroyed by sufficiently large magnetic fields which brings the system into the ferromagnetic state.

The results are in good agreement with the findings presented in the pre-

vious sections of this chapter. The energy barrier protecting the skyrmion state decreases with an increasing magnetic field and it is found to vanish at $\mu|B| \approx 0.156\,J$ by linearly extrapolating the data presented in Fig. 4.5. This is approximately also the magnetic field at which the ferromagnetic state is reached in the hysteresis curves in Fig. 4.11. It can be concluded that the magnetic field transforms the local minimum of the skyrmion into a saddle point at this particular field. In an analogous way, one finds that the energy barrier protecting the ferromagnetic state vanishes at the magnetic field of $\mu|B| \approx 0.22\,J$ pointing into the opposite direction of the sample magnetization. This goes along well with the observation from the hysteresis curve that the ferromagnetic state can be left at low temperatures with the application of a magnetic field pointing into the opposite direction, only.

4.6 Damping regime

The interpretation concerning the shape of the potential wells of the skyrmionic and ferromagnetic states are motivated by the formula for the escape rate r for a system with a viscosity η and an energy barrier Δ in the regime of a high damping [108]

$$r = \frac{\omega\omega'}{\eta} \exp(-\Delta/k_B T) \tag{4.13}$$

Therein, ω and ω' approximate by harmonic potentials the energy landscape around the energy minimum and the barrier respectively. So, if the barrier height and shape ω' is identical on the ways back and forth which is a reasonable assumption because the identity of the barrier height has been shown, the difference in total frequency $\omega \cdot \omega'/\eta$ can only be explained by the shape of the energy minima. To be able to apply the Kramers' theorem one has to satisfy two conditions (i) the energy barrier has to be significantly higher than the thermal energy and (ii) the system has to be in the regime of intermediate to high damping. The energy barriers for the skyrmionic system presented in this chapter have a height of about $(5-10)\,J$ which is by about a factor of ten larger than the thermal energy of $k_B T \approx 0.6\,J$. Hence, the condition (i) is satisfied. The determination of the correct damping regime (ii) is more subtle.

There are strong arguments indicating that the Monte Carlo calculations take place in the regime of high damping since it has been shown for an ensemble of single domain particles that the results of the Landau-Lifshitz-Gilbert equation and a classical heat-bath Monte Carlo scheme coincide in the regime of high damping [109]. With other words, the regime of high damping is imposed by the simulation method. Hence, this supports the assumption that this transition theory provides a good approximation to the MC simulations even though the skyrmionic system is more complex.

4.7 Conclusion

The results of the general MC treatment presented in this chapter reveal several important peculiarities of the switching between single Sk and FM states. The most important finding is that in contrast to other nanomagnets [110] the field dependent mean lifetimes of the Sk and FM states are strongly asymmetric. The analysis reveals that the stability of skyrmions is hidden in the dynamics and the geometry of the energy landscape. Particularly, the attempt frequency of the skyrmion annihilation is orders of magnitudes smaller than that of the skyrmion creation due to a more shallow shape of the potential. The good agreement of these general conclusions with the experimental data on the Pd/Fe bilayer on Ir(111) allow us to make predictions about the applicability of field stabilized skyrmions in thin magnetic films for data storage devices. In order to be able to populate the two states corresponding to "0" and "1" of a binary data cell with an equal probability the applied magnetic field has to be close to B_c. Furthermore, to ensure the stability of the two states of a bit, the energy barrier and hence the activation energy has to be optimized.

Chapter 5

Confinement of spin-spiral state

In this chapter, equilibrium properties of spin-spiral states in two-dimensional systems are discussed. Classical Heisenberg spins on a discrete hexagonal lattice and the continuum model were used to derive effects due to the finite size of a magnetic system. In the end, the findings are employed to explain recent experimental observations about spin-spiral states in the Pd/Fe atomic bilayer on the Ir(111) surface.

Results of this chapter contributed to the following publication:

L. Schmidt, J. Hagemeister, P.-J. Hsu, A. Kubetzka, K. von Bergmann & R. Wiesendanger. Symmetry breaking in spin spirals and skyrmions by in-plane and canted magnetic fields. New J. Phys. **18** 075007 (2016).

5.1 Model Hamiltonian and crystal structure

For the following investigations, the standard Hamiltonian

$$H = -J \sum_{<i,j>} \mathbf{S}_i \cdot \mathbf{S}_j - \sum_{<i,j>} \mathbf{D}_{i,j} \cdot (\mathbf{S}_i \times \mathbf{S}_j) + K \sum_i \sin^2(\Theta_i) \tag{5.1}$$

for skyrmionic systems is chosen. It takes an effective nearest-neighbor exchange interaction and nearest-neighbor Dzyaloshinskii-Moriya interaction with the parameters J and $D = |\mathbf{D}_{i,j}|$ per atom into account. An uniaxial anisotropy energy can be included by the parameter K, which is set to zero for simplicity.

$\mathbf{S}_i$ is considered to be of unit length and can take any orientation in three-dimensional space. In a wide parameter range, the interactions are known to lead to spin-spiral and skyrmionic states at low temperatures [103, 104]. As model systems, triangular two-dimensional lattices are chosen in order to resemble the geometry of pseudomorphic grown magnetic layers on the (111) surface of an fcc-type crystal as e.g. Iridium. For this class of systems, the DM vectors $\mathbf{D}_{i,j}$ are expected to predominantly lie within the magnetic layer and to be perpendicular to the connection line of two atomic sites [58]. Here, the tilting of DM vectors with respect to the magnetic layer is neglected. This particular choice of orientation of the DM-vectors leads to cycloidal spin-spiral and hedgehog-like skyrmion states.

5.2 Infinite system

In the following, the formation of homogenous spin-spiral states in infinite systems at zero temperature is investigated in the absence of an external magnetic field and with a negligible magneto-crystalline anisotropy. Using a discrete model for the description of a magnetic crystal, the energy of a spin-spiral state will depend on the spatial orientation of the corresponding wave vector $\mathbf{k}_{\mathrm{SS}}$. For a triangular lattice, the two crystallographic directions $[\bar{1}2\bar{1}]$ and $[10\bar{1}]$ (see Fig. 5.1) are considered with their total energies

$$E_{[\bar{1}2\bar{1}]}(\Theta) = -2J - 4J\cos(\Theta) - 2\sqrt{3}D\sin(\Theta) \tag{5.2}$$

$$E_{[10\bar{1}]}(\Theta) = -2J\cos(2\Theta) - 2D\sin(2\Theta) - 4J\cos(\Theta) - 2D\sin(\Theta) \tag{5.3}$$

per atom where Θ is the angle between the magnetization directions of neighboring ferromagnetic atomic rows. The energy $E_{[\bar{1}2\bar{1}]}$ can be minimized analytically with respect to Θ providing

$$\tan(\Theta^{\min}_{[\bar{1}2\bar{1}]}) = \frac{\sqrt{3}}{2}\frac{D}{J} \tag{5.4}$$

$$\lambda_{[\bar{1}2\bar{1}]} = \frac{\sqrt{3}}{2}a \cdot 2\pi/\mathrm{atan}(\frac{\sqrt{3}}{2}\frac{D}{J}) \tag{5.5}$$

while $E_{[10\bar{1}]}$ needs to be minimized numerically. The resulting equilibrium spin-spiral periods $\lambda_{[\bar{1}2\bar{1}]}$ and $\lambda_{[10\bar{1}]}$ are shown in Fig. 5.2 a and their deviation

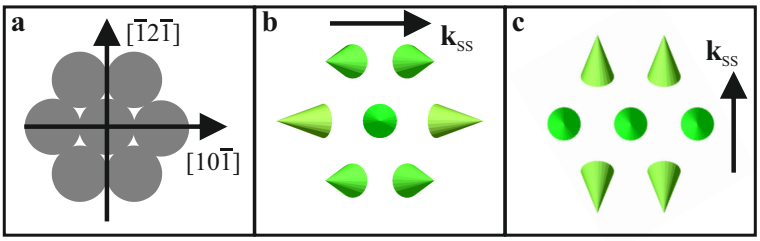

Figure 5.1: Spin-spirals on a triangular lattice. (**a**) Sketch of a 2D triangular lattice with crystallographic directions. (**b**), (**c**) Sketch of spin-spirals along two different crystallographic directions.

is found to be less than 0.5 % for the displayed parameter range. Even smaller is the percental deviation of the two energies for the differently oriented spin-spiral states (Fig. 5.2 b). The deviation increases with an increasing ratio of D/J because the corresponding spin-spiral period shrinks at the same time and, hence, the influence of the discrete spin lattice increases. The alignment of $\mathbf{k}_{SS}$ parallel to the $[10\bar{1}]$ direction is the energetically preferred state which can be explained by the contribution of all bonds to the reduction of both the DM energy and the exchange energy in this state which is not the case for an alignment of $\mathbf{k}_{SS}$ parallel to the $[\bar{1}2\bar{1}]$ direction.

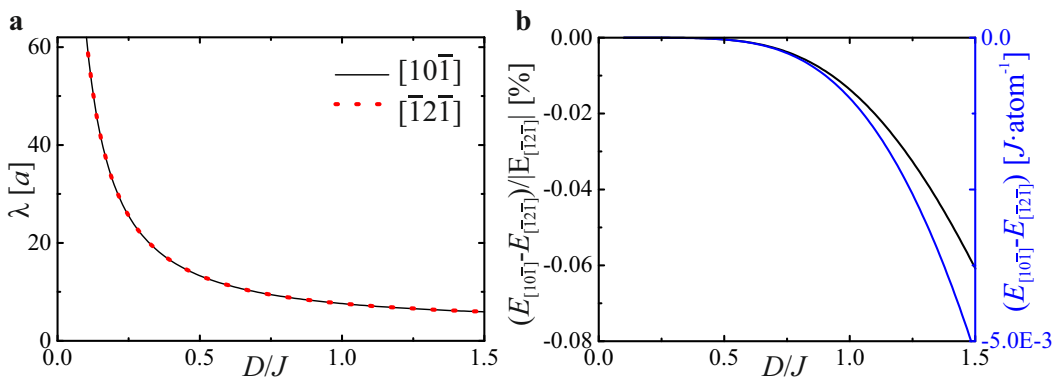

Figure 5.2: Spin-spiral period. (**a**) The equilibrium period of a spin-spiral as a function of D/J. (**b**) The energy difference for spin-spirals with $\mathbf{k}_{SS}$ parallel to the $[\bar{1}2\bar{1}]$ and $[10\bar{1}]$ directions.

5.3 Finite size effects

Both within simulations and in experimental systems, one is typically confronted with finite size effects. Therefore, the investigation of the influence of a boundary onto the formation of spin-spiral states is of both theoretical and experimental interest. First, a uniform spin-spiral state is considered and the energy cost due to a reorientation of $\mathbf{k}_{\mathrm{SS}}$ from parallel to perpendicular with respect to an edge is determined. Second, local relaxation processes of the spin-spiral state at an edge are studied using the continuum model and MC calculations.

5.3.1 Uniform spin-spiral state

A close-packed atomic edge of a finite system is considered (Fig. 5.3 a and b) at which the atoms have the reduced number of four nearest-neighbor atoms instead of six as in the interior of an extended system. The bulk equilibrium spin-spiral states of the previous section are continued uniformly to the edge. Thus, the influence on the magnetic system due to the symmetry breaking of the edge is constricted to the magnetic moments of the first atomic row because nearest-neighbor exchange and DM interactions are considered, only.

It is found that for the atoms at the edge, the energy is most favorable when $\mathbf{k}_{\mathrm{SS}}$ is parallel to the edge and most unfavorable when $\mathbf{k}_{\mathrm{SS}}$ is perpendicular to the edge as shown exemplarily for $D/J = 0.44$ in Fig. 5.3 c. The reason for the energetically preferred parallel orientation is that all bonds contribute to a reduction of both the exchange energy and the DM energy in this case while for a perpendicular orientation, the magnetic moments at the edge are coupled ferromagnetically with respect to each other and the exchange energy is minimized, only (Fig. 5.3 a and b). Fig. 5.3 d shows the energy difference between parallel and perpendicular orientation of $\mathbf{k}_{\mathrm{SS}}$ as a function of D/J. The potential energy gain by a reorientation of $\mathbf{k}_{\mathrm{SS}}$ are orders of magnitudes larger for a magnetic moment at an edge than for a magnetic moment within an extended film as can be observed by a comparison with Fig. 5.2 d.

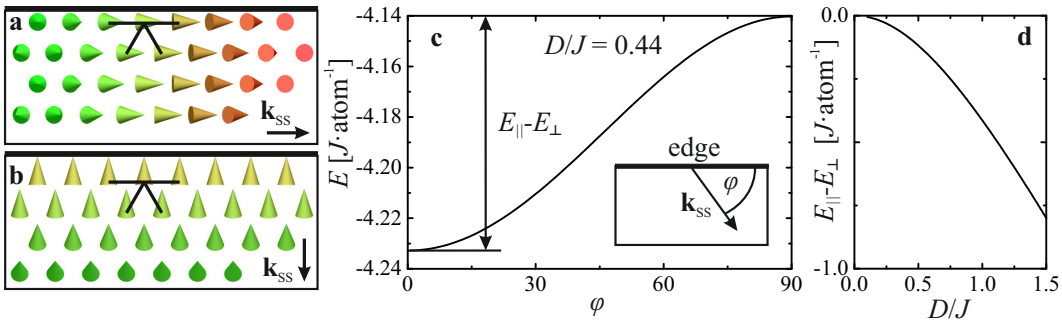

Figure 5.3: Spin-spirals at an edge. (**a**), (**b**) Spin-spiral states with $\mathbf{k}_{SS}$ parallel and perpendicular to the upper edge which is marked with the black bar. Atoms at the edge have four nearest-neighbor atoms only as indicated exemplarily for one site. (**c**) The energy of the spin-spiral state for $D/J = 0.44$ as a function of the angle ϕ between $\mathbf{k}_{SS}$ and the edge. (**d**) The energy difference between parallel and perpendicular orientation of $\mathbf{k}_{SS}$ with respect to the edge as a function of D/J.

5.3.2 Edge tilt effect

Additional tilting effects are expected at the boundaries of thin magnetic samples with interfacial Dzyaloshinskii-Moriya interaction as has been pointed out and explored by *S. Rohart* and *A. Thiaville* using the continuum model [111]. They considered magnetic stripes and nanodots with ferromagnetic exchange interaction, an interface-induced DM interaction and an anisotropy energy as model systems. Edge effects of the uniformly magnetized, spin-spiral and skyrmionic states within these systems are presented but a discussion concerning edge tilt effects in spin-spiral states with an orientation of $\mathbf{k}_{SS}$ parallel to an edge is missing. In the following, this issue will be investigated first within the continuum model and second using Monte Carlo calculations.

The energy E of a two-dimensional magnetic system whose magnetization can be described by a vector field $\mathbf{m}$ within the continuum model is given by

$$E = E_{\text{ex}} + E_{\text{DM}} + E_{\text{K}} \tag{5.6}$$

with

$$E_{\mathrm{ex}} = \int\int A_{\mathrm{c}} \left[\left(\frac{\partial \mathbf{m}}{\partial x} \right)^2 + \left(\frac{\partial \mathbf{m}}{\partial y} \right)^2 \right] \mathrm{d}x\mathrm{d}y \tag{5.7}$$

$$E_{\mathrm{DM}} = \int\int D_{\mathrm{c}} \left[\left(m_{\mathrm{x}} \frac{\partial m_{\mathrm{z}}}{\partial x} - m_{\mathrm{z}} \frac{\partial m_{\mathrm{x}}}{\partial x} \right) + \left(m_{\mathrm{y}} \frac{\partial m_{\mathrm{z}}}{\partial y} - m_{\mathrm{z}} \frac{\partial m_{\mathrm{y}}}{\partial y} \right) \right] \mathrm{d}x\mathrm{d}y \tag{5.8}$$

$$E_{\mathrm{K}} = -\int\int K_{\mathrm{c}} (\mathbf{m} \cdot \mathbf{e}_z)^2 \mathrm{d}x\mathrm{d}y \tag{5.9}$$

according to previous investigations on skyrmionic systems [11] with the continuum parameters $A_{\mathrm{c}}, D_{\mathrm{c}}, K_{\mathrm{c}}$ for the exchange interaction, Dzyaloshinskii-Moriya interaction and anisotropy energy. The vector $\mathbf{e}_z$ provides the system normal. Once more, the anisotropy energy is neglected ($K_{\mathrm{c}} = 0$) for simplicity. The conversion between the continuum parameters and the parameters for the discrete model using a triangular two-dimensional lattice is given according to *S. Rohart* [112] by

$$A_{\mathrm{c}} = \sqrt{3} J \tag{5.10}$$

$$D_{\mathrm{c}} = 2\sqrt{3} D/a \tag{5.11}$$

A magnetic stripe within the $(\hat{y}, \hat{x})$ plane with finite length in $\hat{x}$ and infinite width in $\hat{y}$ direction is considered. Its magnetization $\mathbf{m}$ is parametrized by

$$\mathbf{m}^T = (0, \sin\Theta, \cos\Theta) \tag{5.12}$$

corresponding to a Néel-type spin-spiral state. In order to capture edge effects, a local tilting of the spin-spiral by the angle α around $\hat{y}$ is introduced with the rotation matrix

$$R_{\mathrm{y}}(\alpha) = \begin{pmatrix} \cos\alpha & 0 & \sin\alpha \\ 0 & 1 & 0 \\ -\sin\alpha & 0 & \cos\alpha \end{pmatrix} \tag{5.13}$$

providing the magnetization

$$\mathbf{m}^T = (\sin\alpha\cos\Theta, \sin\Theta, \cos\alpha\cos\Theta) \tag{5.14}$$

In the following, the approximation that α depends on the x-coordinate and Θ on the y-coordinate only is used for simplicity. Furthermore, the equilibrium spin-spiral period $2\pi\xi$ and $\Theta = y/\xi$ with $\xi = 2A_\mathrm{c}/D_\mathrm{c}$ are used. Then, the energy can be written as

$$E = \int_{x_A}^{x_B} A_\mathrm{c} \left[\left(\frac{\partial \alpha}{\partial x} \right)^2 \pi\xi + 2\pi/\xi \right] - D_\mathrm{c} \left[\left(\frac{\partial \alpha}{\partial x} \right) \pi\xi + 2\pi \cos\alpha \right] dx \tag{5.15}$$

where x_A and x_B are the boundaries of the magnetic stripe in the x direction. Note that the integration in y direction over one period length has been performed already and hence, a one-dimensional minimization problem remains which can be solved by using variation calculus. The energy is minimized by the function $\alpha(x)$ which satisfies

$$\frac{\partial^2 \alpha}{\partial x^2} = \frac{2\sin\alpha}{\xi^2} \tag{5.16}$$

and the boundary conditions

$$\frac{\partial \alpha}{\partial x} = \frac{1}{\xi} \qquad x = x_A, x = x_B \tag{5.17}$$

Integration of equation 5.16 provides

$$\left(\frac{\partial \alpha}{\partial x} \right)^2 = -\frac{4\cos\alpha + C}{\xi^2} \tag{5.18}$$

with the integration constant C. Far away from the border, the undisturbed Néel-type spin-spiral state is expected with $\alpha = 0$ and $\partial\alpha/\partial x = 0$. Therefore, the integration constant C can be determined as $C = -4$. Combining the equations (5.17) and (5.18) results in

$$\cos\alpha = \frac{3}{4} \tag{5.19}$$

at the edge of the magnetic stripe. This is equivalent to $\alpha \approx \pm 41.41°$ where the sign needs to be determined by the rotational sense imposed by the DM interaction. Interestingly, the tilting angle of the spin-spiral at the edge of the

magnetic stripe is independent of the material parameters D_c and J_c within this model. However, the length scale on which the influence of the edge on the spin-spiral state diminishes is given by ξ and thus depends on the material parameters. A strong DM interaction will lead to a short spin-spiral period and also a short length on which the edge influence diminishes.

These findings are in good agreement with Monte Carlo calculations as will be shown in the following. A two-dimensional hexagonal lattice in the $(\hat{x}, \hat{y})$ plane with rectangular boundary shape is considered (Fig. 5.4). Periodic boundary conditions are used along the $\hat{y}$ direction and the magnetic moments at the right edge are fixed during the MC calculations. The length of the magnetic sample in the $\hat{x}$ direction is chosen as $159 \cdot \sqrt{3}/2\, a$ which is larger than two times the period of the spin-spirals in the investigated parameter range $J/D \in [1.25, 10]$. Values within this parameter range are selected in such a way that one to three spin-spiral periods are equal to an integer number which can then be used for the width of the magnetic stripe in the $\hat{y}$ direction. This is done to avoid a squeezing or stretching of the spin-spiral states during the MC calculations due to a mismatch of the width of the magnetic stripe and the spin-spiral period.

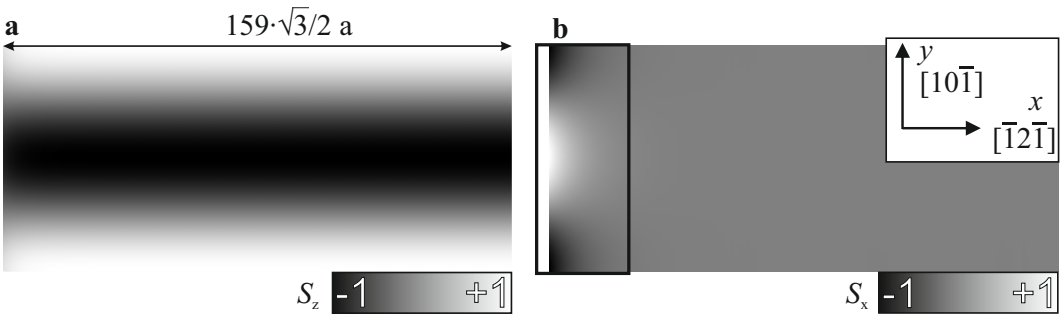

Figure 5.4: Edge tilt in spin-spirals. Néel-type spin-spiral on a two-dimensional triangular lattice with a rectangular shape for $J/D = 10$ as obtained from MC calculations. The system consists of 160 atomic rows in the $\hat{x}$ direction with an inter-row distance of $\sqrt{3}/2\, a$. The width in the $\hat{y}$ direction was adopted in such a way that it is equal to an integer multiple of the spin-spiral period. Periodic boundary conditions were used in the $\hat{y}$ direction. The orientation of the magnetic moments at the right edge is fixed. (**a**) Contrast of the z-component of the magnetization. (**b**) Contrast of the x-component of the magnetization revealing the edge tilt effect at the left edge.

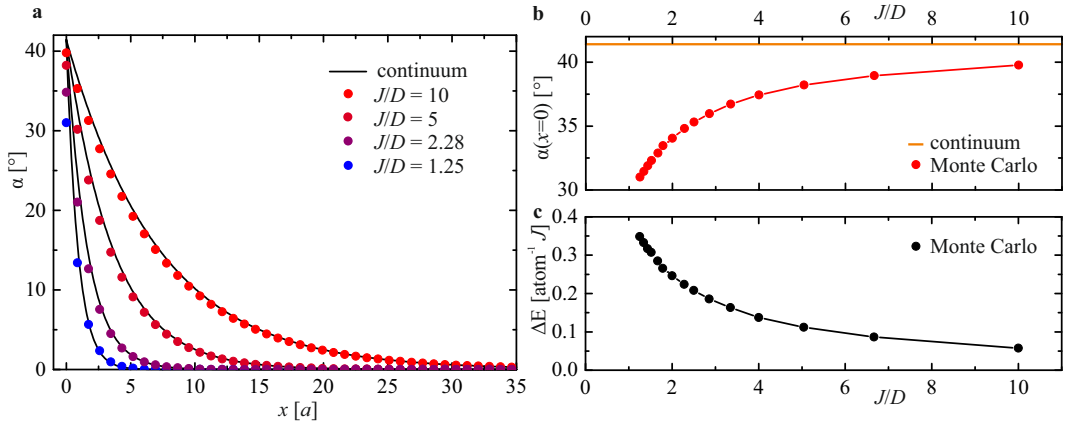

Figure 5.5: Edge tilt profile. (**a**) Tilting angle of the Néel-type spin-spiral as a function of the distance to the edge as obtained from the continuum model and MC calculations. (**b**) Tilting angle at the edge. (**c**) Energy save per atom at an edge due to the tilting compared to the uniform Néel-type spin-spiral state.

Starting point for the MC calculations are artificially set-up Néel-type spin-spiral states according to equation (5.12). Following this, MC calculations are used to find the equilibrium tilting angle of spin-spirals as a function of the distance to the left free edge. This means that the spin-spirals in atomic rows parallel to the edge are rotated by random angles around the $\hat{y}$ axis during the MC calculation. Each initial state is relaxed for $5 \cdot 10^5$ MC steps at the temperature $k_\mathrm{B}T = 1.72 \cdot 10^{-6}\,J$. The result for $J/D = 10$ is shown in Fig. 5.4. The contrast of the z-component of the magnetization is similar to the one expected for a spin-spiral state (Fig. 5.4 a). However, a non-vanishing contrast of the x-component of the magnetization appears at the left edge of the magnetic sample, only, revealing the edge tilting effect (Fig. 5.4 b). The tilting of the spin-spirals as a function of the distance to the edge for several values of J/D are shown in Fig. 5.5 a. Profiles as obtained by the continuum model from equations (5.17, 5.18) using the classical Runge-Kutta method are included for a comparison between the two models. A good agreement between the two models can be observed. This is further investigated by taking a closer look at the tilting angle in the first atomic row at the edge which is found to increase with an increasing J/D and seems to approach the continuum value of 41.41° from smaller values (Fig. 5.5 b). The energy save that arises due to the edge tilt is shown in Fig.5.5 c. The continuum model and MC calculations

that have been presented so far, consider a coherent rotation of the spin-spiral in an atomic row parallel to the edge, only. However, the influences of this restriction are comparably small as has been checked for $J/D = 10$ by an additional post-relaxing of the obtained spin structures by a MC calculation that allows for an individual adjustment of the orientation of the magnetic moments. Gaussian sampling according to section 3.2.2 with σ in the range of [0.05,0.1] was used for this purpose.

5.4 Comparison with experiment

Here, the theoretical results from above are compared to experimental observations made on the atomic bilayer islands of fcc stacked Pd on fcc stacked Fe on Ir(111) with a spin-polarized scanning tunneling microscope [22, 113]. See Ref. [114, 115, 93] for an introduction to (spin-polarized) scanning tunneling microscopy. Fig. 5.6 taken from Ref. [113] shows an island at $T = 8\,\mathrm{K}$ measured at the constant tunneling current $I = 0.2\,\mathrm{nA}$ and the bias voltage $U = 50\,\mathrm{meV}$. The island exhibits a spin-spiral state with a strong tendency to locally align the spin-spiral vector $\mathbf{k}_{\mathrm{SS}}$ parallel to an edge. Within the interior of the island, $\mathbf{k}_{\mathrm{SS}}$ is predominantly parallel to a crystallographic direction equivalent to the $[11\bar{2}]$ direction. While the first observation is in a qualitative good agreement with the theoretical findings, the second observation can not be explained qualitatively by the simplified model taking next-nearest exchange and DM-interactions into account, only. Therein, the $[10\bar{1}]$ direction

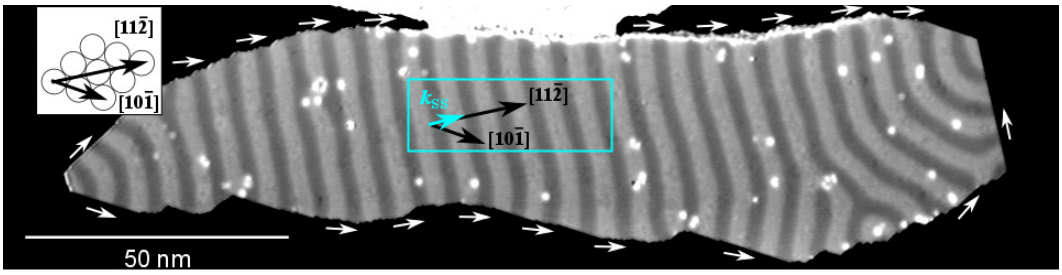

Figure 5.6: Coupling of spin-spirals to edges of atomic Pd/Fe-bilayers on Ir(111). The image is taken from Ref. [113]. Spin-spiral state on the bilayer Pd-Fe on Ir(111) measured with a spin-polarized scanning tunneling microscope. The white arrows indicate the orientation of $\mathbf{k}_{\mathrm{SS}}$ at the edge of the island.

was found to be energetically weakly favorable. In order to gain an insight into the influence of the edge of an island onto the formation of the spin-spiral state within its interior, absolute numbers for possible energy costs at the edge and within the interior region are determined based on the theoretical results. By analyzing the area and the border length of the island in Fig. 5.6, quantitative values for the energy contributions at the edge and the interior of the island can be made. The area of the island is approximately $6000\,\mathrm{nm}^2$ and the perimeter $445.5\,\mathrm{nm}$. This means that the island consists of about $N = 95000$ Fe atoms of which $N_{\mathrm{edge}} = 1650$ are located at an edge. The energy costs due to a reorientation of $\mathbf{k}_{\mathrm{SS}}$ depends on the value for D/J. The effective exchange energy parameter $J = |J_{\mathrm{eff}}| = 2.3\,\mathrm{meV}$ and $D = 1\,\mathrm{meV}$ with $D/J \approx 0.435$ by Dupé *et al.* are used for the following considerations. A reorientation of $\mathbf{k}_{\mathrm{SS}}$ from the $[10\bar{1}]$ to the $[11\bar{2}]$ direction within the interior of the island would cost about $N \cdot 1.44 \cdot 10^{-5}\,J \approx 3\,\mathrm{meV}$. However, a pure reorientation of $\mathbf{k}_{\mathrm{SS}}$ from parallel to perpendicular to the edge without taking edge tilting effects into account would already result in an energy cost of $N_{\mathrm{edge}} \cdot 9.2 \cdot 10^{-2}\,J \approx 350\,\mathrm{meV}$. The values for the energy costs per atom were taken from Fig. 5.2 b and Fig. 5.3 c. The edge tilting effect would decrease the energy of the state where $\mathbf{k}_{\mathrm{SS}}$ is parallel to an edge even further by $0.22\,J$ per atom at the edge. Hence, an additional energy contribution of $N_{\mathrm{edge}} \cdot 0.22\,J \approx 835\,\mathrm{meV}$ is obtained. Summing up, a total energy contribution of $1185\,\mathrm{meV}$ at the edge are in competition with $3\,\mathrm{meV}$ within the interior of the island within the used model. Therefore, a strong influence of the edge on the alignment of the spin-spirals within the interior of the island can be explained. However, there are multiple effects that could decrease this effect. These can be changing energy parameters to the edge of the island, atomic defects within the island, higher order parameters of the exchange and DM-interaction and contributions of the anisotropy energy.

5.5 Conclusion

Within this chapter, basic properties of spin-spiral states as their period were discussed for ultrathin film based skyrmionic systems consisting of two-dimensional discrete hexagonal spin lattices. Furthermore, the influence of an edge due to a finite system size was investigated. It was found that it is energetically favor-

able to locally align the spin-spiral vector parallel with respect to an edge. The energy is further reduced by a tilting of the spin-spiral state at an edge. For this finding, calculations using the Monte Carlo program and the continuum model were combined and found to be in good agreement. The continuum model shows that the tilting angle of the spin-spiral state at an edge is equal to 41.41° and independent of the parameters D and J for zero anisotropy. The results are consistent with the experimental observation that the spin-spiral vector tends to be locally parallel to an edge in Pd/Fe bilayer islands on Ir(111).

Chapter 6

Confinement of nanoskyrmions in Fe/Ir(111)

Topic of this chapter are confinement effects on the square nanoskyrmion lattice in the fcc-type Fe atomic monolayer on Ir(111) which arise due to the finite size of the Fe layer. First, frustration effects due to symmetry mismatch of the square nanoskyrmion lattice and the boundary shape of triangular Fe islands is studied. Second, the influence of a ferromagnetic edge is investigated which is realized in experiment by the deposition of additional Ni islands. The presented experimental results were obtained and analyzed by Davide Iaia and André Kubetzka and Kirsten von Bergmann. Monte Carlo calculations using energy parameters based on the parameter set obtained with density function theory calculations by Stefan Heinze *et al.* [21] are compared to the experimental findings and provide a deeper insight into the edge effects. In the beginning of this chapter, the experimental findings are presented in section 6.1 and following this, the Monte Carlo results are shown in section 6.2. An introduction to the material system Fe/Ir(111) is given in the beginning of this thesis in section 2.2.2.

Results of this chapter are part of the following publication:

J. Hagemeister, D. Iaia, E.Y. Vedmedenko, K. von Bergmann, A. Kubetzka & R. Wiesendanger. Skyrmions at the edge: Confinement effects in Fe/Ir(111). Phys. Rev. Lett. **117** 207202 (2016).

6.1 Experimental studies

Sample preparation and STM experiments were performed in a multi-chamber system with different chambers for single crystal preparation, thin film growth and low temperature STM [116], with base pressures in the low 10^{-10} mbar range. The Ir(111) single crystal surface was prepared by repeated cycles of Ar^+ ion etching and annealing at about 1600 K and occasional heating at $T = 1500$ K in an O_2 atmosphere of $p = 1 \times 10^{-6}$ mbar down to $p = 5 \times 10^{-8}$ mbar. After the last annealing step of the Ir(111) surface, the Fe evaporation was deposited after a 90 min break in order to ensure room temperature growth. The SP-STM measurements were done with bulk Cr tips which were prepared *in situ* by voltage pulses and controlled collisions with the Ir(111) surface.

Fig. 6.1 shows a current map of a sample area exhibiting both an extended fcc Fe atomic monolayer high stripe, which grew from an Ir step edge (upper left of Fig. 6.1), and two free-standing fcc Fe islands. A current map measured with the feedback loop active, as in Fig. 6.1, is essentially equivalent to a differentiated topography image, $\mathrm{d}z/\mathrm{d}x(x, y)$, and allows to show small-scale structures on large areas and on different height levels without the need for image processing. Three types of rotational domains can be seen and were labeled A, B and C. Commonly observed one-dimensional defects of the magnetic texture within the stripes are dislocation lines, see left inset, separating equivalent but laterally shifted skyrmion lattices. Apparently they result from stress, which might arise from a varying stripe width or from pinning at remaining defects within the layer. The rotational domains exhibit a clear trend of coupling with a diagonal of the magnetic unit cell parallel to straight, close-packed edges: in the stripe in Fig. 6.1, two C domains and an A domain are found at respective edges, while the surrounding domain is of type B. In the case of the C domains a defect and the 2nd layer Fe island might have played a role in the domain formation, but no defects are found in the vicinity of the A domain. This kind of edge domain is much more rare in stripes with smoother edges.

In the islands, due to their defined shapes, the coupling of the skyrmion lattice to the edges is most apparent: the A domain is found at the left edge, type B and C at the upper and right edges, respectively. Consequently, a

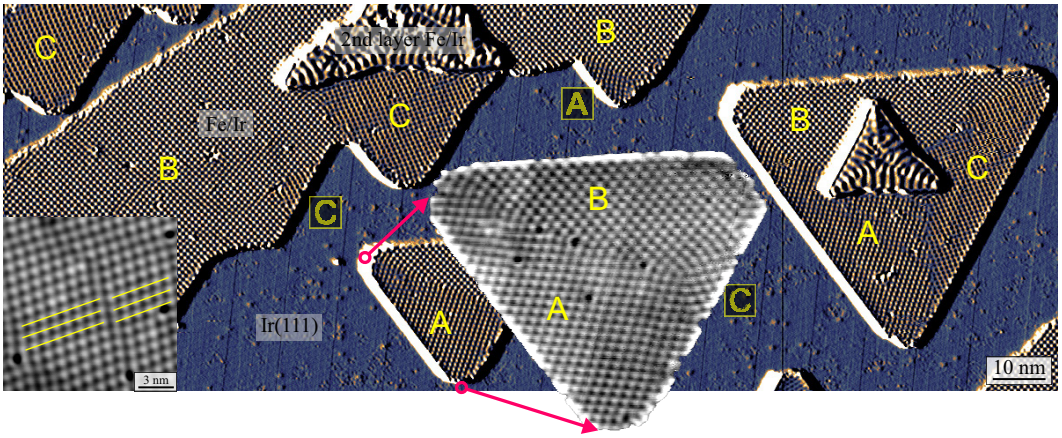

Figure 6.1: Coupling of nanoskyrmion lattice to close-packed edges. Spin-polarized STM current map of fcc Fe on Ir(111), the insets show topographic data in gray. Measurement parameters: $I = 1\,\mathrm{nA}$, $U = 20\,\mathrm{mV}$, $T = 7.7\,\mathrm{K}$, $B = 1.5\,\mathrm{T}$, bulk Cr tip. One can observe three rotational domains of the nanoskyrmion lattice, labeled A, B and C, which show a strong correlation to the Fe step edge direction, i.e. one diagonal of the magnetic unit cell shows a preference for coupling parallel to the edge. The mismatching symmetry of the square nanoskyrmion lattice and the triangular shape of islands leads to frustration and the formation of domain walls.

triple-domain state arises from the combined effect of coupling to the edges and the mismatching symmetries of triangular island shape and square skyrmion lattice. Details of this state can be seen in the inset in Fig. 6.1, showing the height data, $z(x, y)$. The domain wall width is on the order of the skyrmion size, i.e. $\approx 1\,\mathrm{nm}$. The C domain is much smaller than the other two domains, possibly because the domain wall between domain A and B is pinned at defects. The magnetic frustration of the system also becomes apparent by magnetic noise within the image data, i.e. the spin configuration is not entirely stable during imaging, especially in the right corner of the island and at the domain wall between domain B and C. The simplest type of this kind of magnetic jitter is a domain wall movement, activated thermally or by the tunnel current. The larger island in Fig. 6.1 shows a similar triple-domain state, despite the second layer island on top, which itself has a magnetic spiral state [117]. Note that the vast majority of Fe islands grow in hcp stacking on Ir(111) [118] which exhibit a hexagonal spin texture and consequently show no sign of frustration due to confinement.

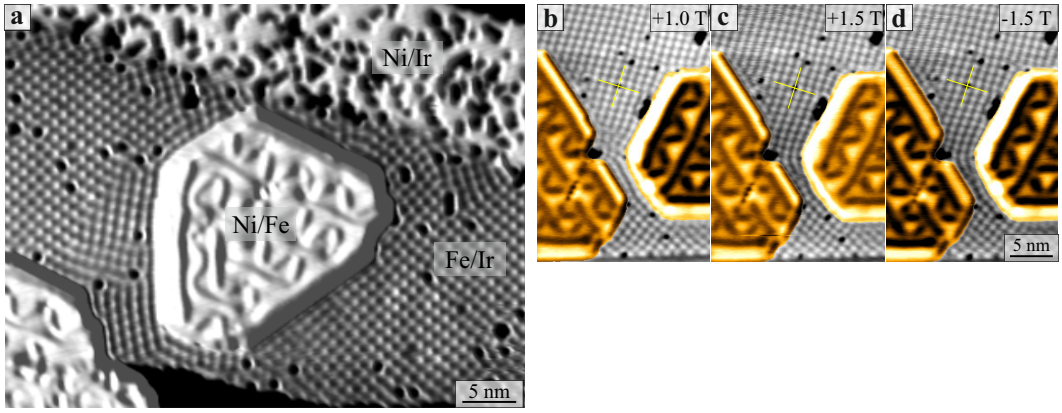

Figure 6.2: Coupling of nanoskyrmion lattice to a ferromagnetic edge. (**a**) Pseudo 3D SP-STM topography image of a Ni island on a fcc Fe stripe on Ir(111). The ferromagnetic Ni causes frustration in the surrounding nanoskyrmion lattice. Here, a side of the magnetic unit cell shows a preference for parallel orientation to the ferromagnetic edge, in contrast to the free-standing edges in Fig. 6.2. (**b-d**) Field-dependent SP-STM data ($I = 1\,\mathrm{nA}$, $U = 500\,\mathrm{mV}$, $T = 7.5\,\mathrm{K}$, bulk Cr tip, gray: topographic data on Fe/Ir(111), color: $\mathrm{d}I/\mathrm{d}U$ signal on Ni/Fe/Ir(111)). (**c**) The right island switched from down to up and the magnetic contrast on Fe/Ir(111) inverted in the upper part of the image. (**d**) Both islands switched from up to down and the magnetic contrast on Fe/Ir(111) inverted again. This can be seen by using a defect (see e.g. yellow cross) as a reference, and demonstrates that this part of the nanoskyrmion lattice is magnetically coupled to the right islands.

The island edges select the adjacent rotational domains, despite the resulting energy cost for domain wall formation due to frustration in the interior of the island. To investigate the impact of edge properties onto the nanoskyrmion lattice, the boundary conditions are modified from open to ferromagnetic. For that purpose, monoatomic layer Ni islands were prepared on fcc Fe/Ir(111) stripes which are ferromagnetic with an out-of-plane easy axis [119]. The effect of such an island onto the surrounding skyrmion lattice can be seen in Fig. 6.2 a. Small domains are formed in the island's vicinity, with a side of the magnetic unit cell oriented parallel to the island edge. These orientations are distinct from the three observed in Fe stripes and islands in Fig. 6.1. The coupling of the skyrmion lattice can be demonstrated directly by switching the NiFe islands in an external magnetic field: between Fig. 6.2 b and c the right island is switched from down to up by increasing the external field from $+1\,\mathrm{T}$

to +1.5 T. This is accompanied by magnetic contrast inversion of the skyrmion lattice in the upper half of the image. Switching both islands from up to down in Fig. 6.2 d also switches the skyrmion lattice back to a state like in Fig. 6.2 b. The skyrmion lattice in the upper part of the image is thus coupled to the right island, where a side of the magnetic unit cell runs parallel to the island edge.

6.2 Monte Carlo studies

The previous section discusses experimental observations of confinement effects on the nanoskyrmion lattice in Fe/Ir(111). In the following, it is shown that the major effects can be reproduced with Monte Carlo calculations allowing for a deeper insight into underlying mechanisms. First, the model Hamiltonian and a consistency check with previous experimental results are presented. Then, the formation of triple-domain states within triangular islands due to the symmetry mismatch of the island boundary and the square symmetry of the nanoskyrmion lattice is studied. In the course of this, edge energies and domain wall energies are calculated. Furthermore, the behavior of the nanoskyrmion lattice in the vicinity of a ferromagnetic edge is investigated and an energetically unstable rotational domain of the nanoskyrmion lattice is found which is unequal to the three rotational domains discussed in previous experimental and theoretical studies.

6.2.1 Model Hamiltonian and consistency check

The magnetic behavior of the pseudomorphic, fcc grown atomic Fe monolayer on the Ir(111) surface can be described with the Hamiltonian

$$\begin{aligned} H = &- \sum_{i,j} J_{i,j} \mathbf{S}_i \cdot \mathbf{S}_j - \sum_{i,j} \mathbf{D}_{i,j} \cdot (\mathbf{S}_i \times \mathbf{S}_j) - \sum_{i,j} B_{i,j} (\mathbf{S}_i \mathbf{S}_j)^2 + K_\perp \sum_i (\mathrm{S}_i^\mathrm{z})^2 \\ &- \sum_{ijkl} K_{ijkl} [(\mathbf{S}_i \mathbf{S}_j)(\mathbf{S}_k \mathbf{S}_l) + (\mathbf{S}_i \mathbf{S}_l)(\mathbf{S}_j \mathbf{S}_k) - (\mathbf{S}_i \mathbf{S}_k)(\mathbf{S}_j \mathbf{S}_l)] \end{aligned} \tag{6.1}$$

with localized Heisenberg spins $\mathbf{S}_i$ on a triangular lattice as demonstrated by Heinze *et al.* [21]. The contributing energy terms originate from the exchange interaction up to the eighth nearest neighbor, the Dzyaloshinskii-Moriya (DM)

interaction, the biquadratic interaction, a perpendicular anisotropy and the four-spin interaction with the parameters [21]

$$\begin{aligned} J_1 &= +5.7\,\text{meV} & J_2 &= -0.84\,\text{meV} & J_3 &= -1.45\,\text{meV} \\ J_4 &= -0.06\,\text{meV} & J_5 &= +0.2\,\text{meV} & J_6 &= +0.2\,\text{meV} \\ J_7 &= -0.2\,\text{meV} & J_8 &= +0.5\,\text{meV} & D_{i,j} &= -1.8\,\text{meV} \\ K_{ijkl} &= -1.05\,\text{meV} & B_{i,j} &= -0.2\,\text{meV} & K_\perp &= -0.8\,\text{meV} \quad . \end{aligned} \tag{6.2}$$

An introduction to the various contributing energy terms is provided in chapter 2 of this thesis. For simplicity, the contributions of the exchange interaction up to the third nearest neighbors are taken into account, only. For a consistency check, the magnetic ground state at low temperatures and the transition temperature are determined. A circular magnetic sample system is chosen in order to minimize the effects of a symmetry breaking due to the boundary on the formation of the nanoskyrmion lattice. The temperature is reduced from 50 K to 1 K in 50 temperature steps each consisting of $2 \cdot 10^5$ MC-steps. A nanoskyrmion lattice state is found at $T = 1\,\text{K}$ as can be observed in Fig. 6.3 a which displays an excerpt of the atomic magnetic configuration. In experiments with spin-polarized scanning tunneling microscopes, the projection of the local sample magnetization onto the magnetization direction of the tip is determined. Hence, a color map image of the nanoskyrmion lattice (Fig. 6.3 b) in which the color scale is determined by the perpendicular component of the magnetization is created for further comparison. The corresponding Fourier transform (Fig. 6.3 c) shows four main spots that can be described with the vectors $\mathbf{Q}_1$ and $\mathbf{Q}_2$ with $|\mathbf{Q}_1| = |\mathbf{Q}_2| = Q = 0.264 \times 2\pi/a$ and an inner angle of $\theta = 85.6°$. The reciprocal vectors $\mathbf{Q}_\text{L}$ of the underlying atomic lattice can be added under the assumption of the lattice constant $a = 2.715\,\text{Å}$ [21] and a reciprocal vector is found to lie in the middle of $\mathbf{Q}_1$ and $\mathbf{Q}_2$ which gives rise to the formation of three rotational domains of the nanoskyrmion lattice as reported in previous investigations [21]. Here, it is found that $\mathbf{Q}_1 + \mathbf{Q}_2 \approx 3 \cdot \mathbf{Q}_\text{L}$. In previous experimental investigations, $Q = 0.277 \times 2\pi/a$ and $\theta = 92.2°$ [21] were observed.

In order to determine the transition temperature, the specific heat of the system was calculated as a function of the temperature (Fig. 6.3 d) which

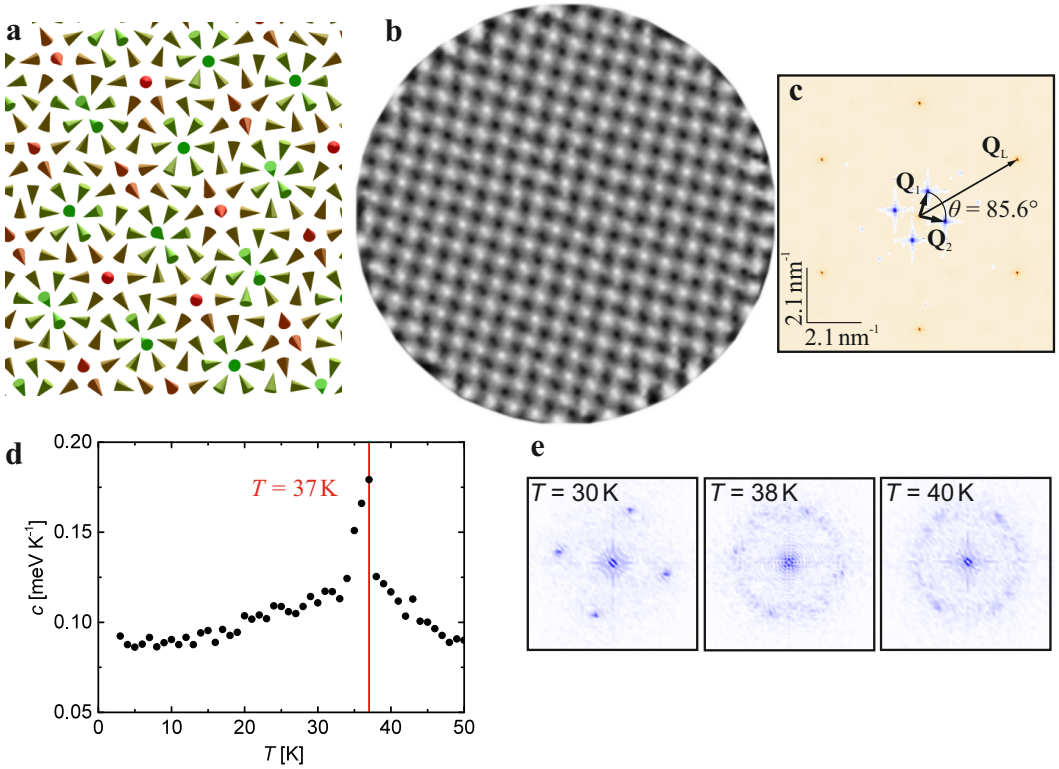

Figure 6.3: Consistency check of energy parameters. Temperature dependent MC studies of the nanoskyrmion lattice. (**a**) Spin structure at $T = 1\,\mathrm{K}$. (**b**) Contrast of the z-component of the magnetization. (**c**) Fourier transform of (b) (blue spots) together with the Fourier transform of the underlying crystal lattice (red spots). (**d**) Specific heat capacity as a function of temperature. A peak at $T \approx 37\,\mathrm{K}$ indicates the transition temperature to the paramagnetic state. (**e**) Fourier transform of the nanoskyrmion lattice at different temperatures. The long range order is lost at approximately 37 K.

exhibits a peak at the temperature $T_\mathrm{c} = 37\,\mathrm{K}$. At temperatures close to T_c, the four Fourier spots of the nanoskyrmion lattice transform into a circle with a radius close to Q (Fig. 6.3 e). This indicates a loss of the long-range order of the nanoskyrmion lattice while the periodicity of the magnetic structure is conserved locally. Experimental studies showed a transition temperature of $T_\mathrm{c} = 27.8\,\mathrm{K}$ [120] which was determined by a vanishing magnetic contrast in the images obtained with a spin-polarized scanning tunneling microscope. This temperature is somewhat lower than the one obtained with the present Monte Carlo calculations. It is known that the size of a finite sample has an influence on the peak position in the specific heat capacity in the Monte

Carlo calculations. However, this could rather explain a smaller transition temperature instead of a larger one 3.4. Still, the theoretical model seems to have an overall reasonable agreement with the experimental findings and was used for the following investigations.

6.2.2 Confinement in triangular islands

For the study of confinement effects on the nanoskyrmion lattice, equilateral triangular islands are considered similarly to the ones found in experiment (section 6.1). Here, the island size is chosen such that each edge consists of 200 atoms which is equivalent to a side length of $\approx 54\,\mathrm{nm}$. The experimentally studied islands possessed edges of $30\,\mathrm{nm} - 60\,\mathrm{nm}$ length.

When reducing the temperature from $45\,\mathrm{K} > T_\mathrm{c}$ to $0.1\,\mathrm{K}$ in 45 temperature steps with 5×10^4 MC steps each, multi-domain states similar to the one shown in Fig. 6.4 a are obtained. All three rotational domains of the nanoskyrmion lattice are visible within a single island and, like in experiment, one diagonal

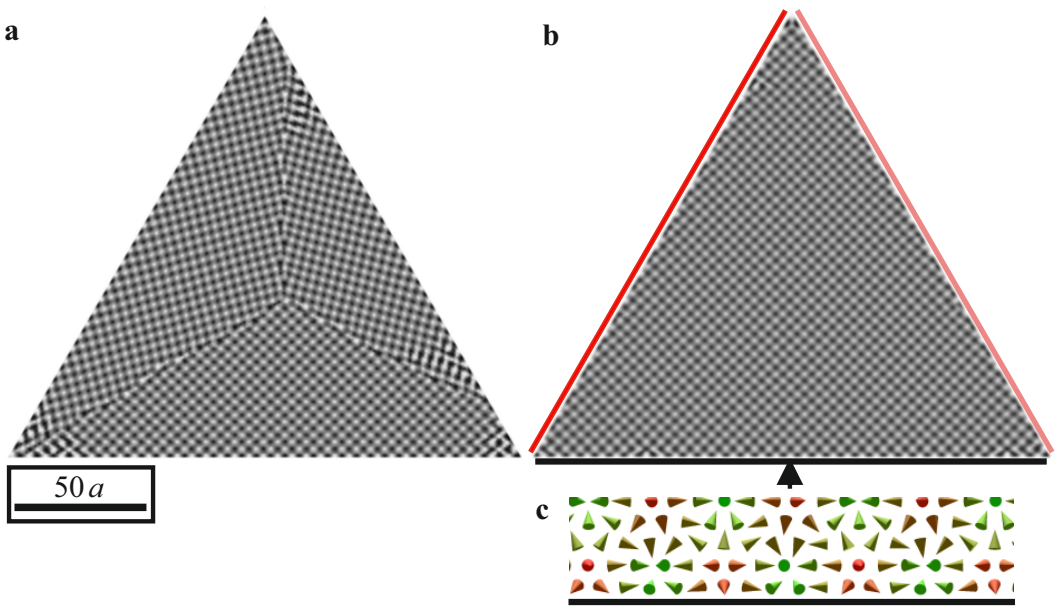

Figure 6.4: Confinement in triangular islands. (**a**), (**b**) Triangular islands with open boundary conditions exhibiting multi- and single-domain states at $T = 0.1\,\mathrm{K}$. The displayed out-of-plane sensitive SP-STM images were calculated from the Monte Carlo spin configurations as described in Ref. [121]. (**c**) Spin structure of the nanoskyrmion lattice at the energetically favorable edge, taken from (b).

of the square of the magnetic unit cell is mostly aligned parallel to the edge of an island. For this island size, a single-domain state is not obtained as a result of the cooling process from a random initial state. Since a single-domain state is needed to determine the energy of the energetically favorable and unfavorable edges, this state is constructed by periodically repeating the spin structure of one of the domains and a subsequent annealing by cooling from $15\,\mathrm{K} < T_\mathrm{c}$ to $0.1\,\mathrm{K}$ within 15 temperature steps of 5×10^4 MC steps each. The result is a single-domain state coupled to one of the edges with a diagonal of the magnetic unit cell parallel to the edge, as before, and two edges showing spin configurations with lower symmetry, see Fig. 6.4 b. In order to obtain a statistical average, the artificially constructed structure was relaxed by decreasing the temperature of the system from 8 different temperatures in the range of $16-23\,\mathrm{K}$ to $0.1\,\mathrm{K}$ in 15 temperature steps with $5 \cdot 10^4$ Monte Carlo steps each. A closer inspection of the preferred edge in Fig. 6.4 c shows that the skyrmion centers are positioned in the second row from the edge. At the edge itself the spin configuration is a cycloidal spiral running along the edge, tilted about 30° from the perpendicular direction. This configuration is reminiscent of the coupling of spin spirals to edges in PdFe/Ir(111) (section 5.4) and the edge tilt observed in calculations of systems dominated by the Dzyaloshinskii-Moriya interaction (section 5.3.2).

As a starting point, the mean total energy per atom is calculated row-wise as a function of the distance to the edges at $T = 0.1\,\mathrm{K}$ (Fig. 6.5). The labeling of the edges refers to the triangular island shown in Fig. 6.4 b. The top-left and the top-right edges are energetically equivalent and the energy converges with an increasing distance from the edge whereas for the bottom, energetically

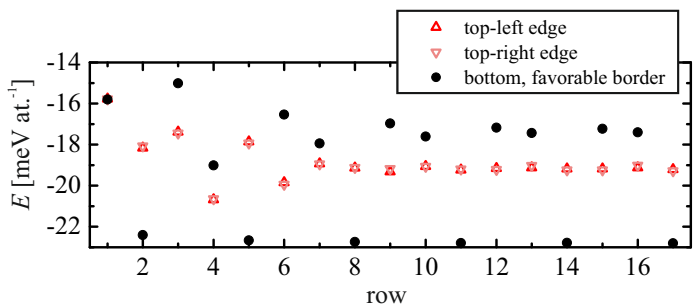

Figure 6.5: Energy analysis at an edge. Row-wise mean energy per atom as a function of the distance to the edge. The labels correspond to the island Fig. 6.4 b

favorable edge the mean energy is approximately periodic with a periodicity of 3 atomic rows far away from the edge. In the latter case, two atomic rows which have approximately the same energy are followed by a row of lower energy. The atomic row with the lower energy coincides with a diagonal of the nanoskyrmion lattice. Thereafter, the mean energy cost for each atomic row with respect to a corresponding bulk atomic row can be determined. This is shown in Fig. 6.6 for the individual energy contributions as well as for the total energy. One can observe that the influence of an edge diminishes with the distance to the edge and that it is small from approximately the tenth atomic row on. The energy difference of the first twelve atomic rows between the energetically favorable and unfavorable edge is displayed at the right side of Fig. 6.6. A minus sign in the energy difference indicates that the bottom edge is energetically favorable. One can deduce that within the considered model the interplay of the first and third nearest neighbor exchange interaction, the DM interaction and the four-spin interaction are responsible for the alignment of the diagonal of the nanoskyrmion lattice parallel to an edge. Therein, energy gains in the first and third nearest neighbor exchange interaction as well as in the DM interaction compensate an energy loss in the four-spin interaction and cause a total energy gain of $\approx 2.2\,\mathrm{meV}a^{-1}$ between the two orientations of the nanoskyrmion lattice with respect to an edge. This value is equivalent to $8.1\,\mathrm{meV/nm}$.

In the next step, the energy cost due to the formation of a domain wall is estimated. The energy density of the system varies locally both within the nanoskyrmion lattice as well as in a domain wall between two different rotational domains of the nanoskyrmion lattice. Furthermore, the spin structure appears to be incommensurate with the crystal structure such that the energy of a domain wall cannot be determined by simply averaging the energy of multiple atoms contributing to the domain wall. Instead, it can be derived by a comparison of the energies of islands with single domain and multi-domain states. A multi- and a single-domain state island were shown beforehand in Fig. 6.4a and b. Additional multi-domain-states were produced by reducing the temperature from the paramagnetic state to 0.1 K as before. In total, three different magnetic triple-domain states as shown in Fig. 6.7 were taken into account with energies as presented in table 6.1.

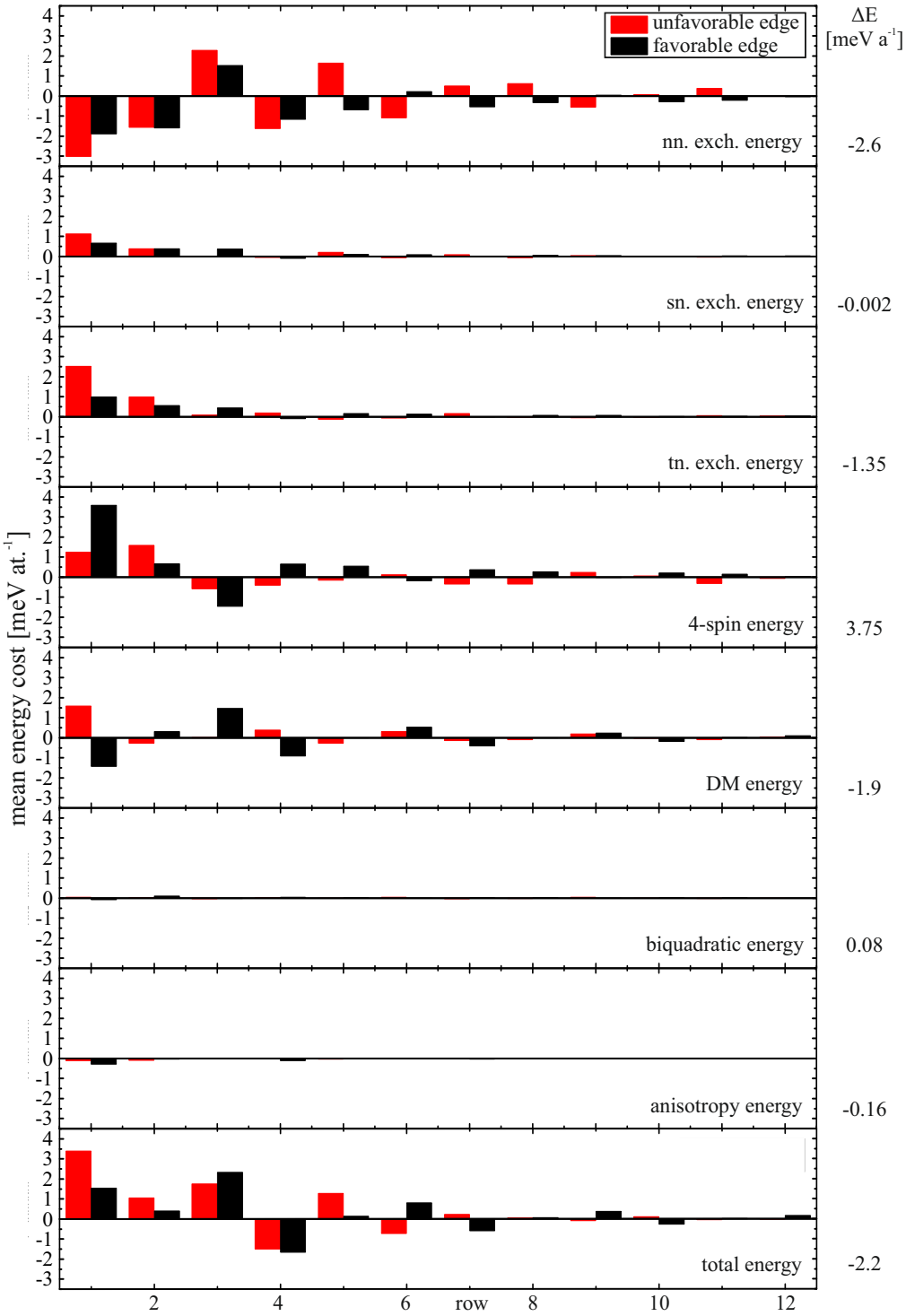

Figure 6.6: Energy costs of an edge. Row-wise mean energy cost per atom as a function of the distance to the edge. The values to the right side provide the energy difference of the sums of the costs for the two edges. The minus sign indicates that the bottom edge of the island in Fig. 6.4 b is energetically preferred.

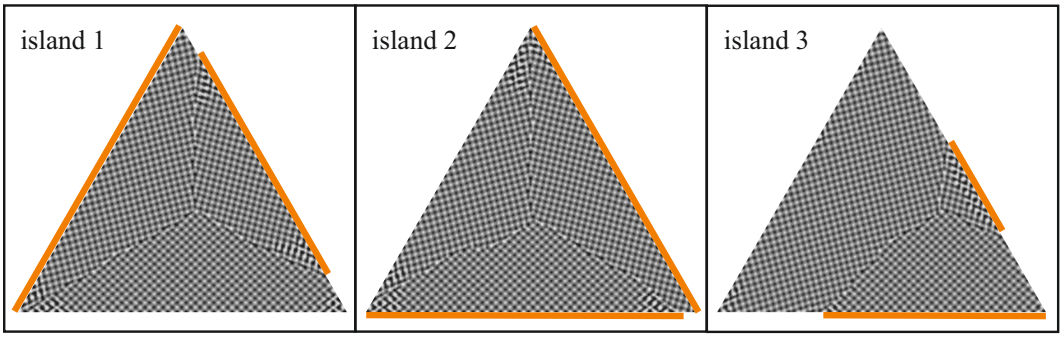

Figure 6.7: Multi-domain states in triangular islands. Three islands with multi-domain states at T = 0.1 K. The parts of the edges at which the nanoskyrmion lattice has to be reoriented locally in order to go to a single-domain state are marked.

The domain wall lengths s_{dw} of the three islands are $s^1_{\mathrm{dw}} \approx 300$, $s^2_{\mathrm{dw}} \approx 320\,a$ and $s^3_{\mathrm{dw}} \approx 175\,a$. At the edge, the nanoskyrmion lattice has to be reoriented on a length s_{edge} for a transition to the single-domain state and $s^1_{\mathrm{edge}} \approx 340\,a$, $s^2_{\mathrm{edge}} \approx 368\,a$ and $s^3_{\mathrm{edge}} \approx 200\,a$. The energy costs $\Delta E_{\mathrm{edge}} = 2.2\,\mathrm{meVa}^{-1}$ for a reorientation of the nanoskyrmion lattice at an edge is discussed in the previous section. The energy cost ΔE_{dw} due to the formation of a domain wall is obtained with

$$\Delta E_{\mathrm{dw}} = (E_{\mathrm{multi-domain}} - E_{\mathrm{single-domain}} + s_{\mathrm{edge}} \Delta E_{\mathrm{edge}})/s_{\mathrm{dw}}$$

and the results for the three islands is shown in table 6.2. The four-spin interaction and the anisotropy energy are decreased by the formation of a domain wall while the exchange energies as well as the DM energy are increased. This adds up to a total energy increase of about 3.1 meV/a or 11.4 meV/nm

	$E_{\mathrm{nn.exch.}}$ [meV]	$E_{\mathrm{sn.exch.}}$ [meV]	$E_{\mathrm{tn.exch.}}$ [meV]	$E_{\mathrm{biq.}}$ [meV]	$E_{\mathrm{4-spin}}$ [meV]	E_{DM} [meV]	$E_{\mathrm{aniso.}}$ [meV]	E_{total} [meV]
single domain	-263763 ±386	-18296 ±86	-56901 ±68	7643 ±12	33242 ±241	-81653 ±58	-2651 ±18	-382379 ±18
island 1	-264402	-17504	-56560	7717	32954	-81488	-2927	-382209
island 2	-264163	-17474	-56580	7718	32752	-81483	-2956	-382186
island 3	-264047	-17783	-56711	7690	32865	-81481	-2825	-382293

Table 6.1: Energies of islands with single and multi-domain states. The energies of the single-domain state of Fig. 6.4 b and of the multi-domain states in Fig. 6.7.

	$\Delta E_{\text{nn.exch.}}$ [meV a^{-1}]	$\Delta E_{\text{sn.exch.}}$ [meV a^{-1}]	$\Delta E_{\text{tn.exch.}}$ [meV a^{-1}]	$\Delta E_{\text{biq.}}$ [meV a^{-1}]	$\Delta E_{4-\text{spin}}$ [meV a^{-1}]	ΔE_{DM} [meV a^{-1}]	$\Delta E_{\text{aniso.}}$ [meV a^{-1}]	ΔE_{total} [meV a^{-1}]
island 1	0.82	2.64	2.67	0.16	-5.21	2.70	-0.74	3.04
island 2	1.74	2.57	2.56	0.14	-6.84	2.72	-0.77	3.11
island 3	1.35	2.93	2.63	0.18	-6.44	3.15	-0.81	2.99

Table 6.2: The energy cost of a domain wall. The average energy cost of a domain wall compared to the nanoskyrmion lattice divided by the domain wall length.

which is on the same order as the difference in edge energies ΔE_{edge}. Interestingly, the competition of the energy contributions from the edge and the domain wall favor a mono-domain state for the triangular islands as can be seen in the total energies in table 6.1. Therefore, it can be concluded that the domain walls are formed due to entropy when decreasing the temperature from above T_{c}. However, effects that were not taken into account in the Monte Carlo calculations, may play a role in the experimental systems. Firstly, atomic defects can cause domain wall pinning (Fig. 6.1). Secondly, the magnetic interactions and the anisotropy energy could be different at the edge compared to the interior, which would change the energy balance between single- and multi-domain state. For example, with the calculated domain wall energy and a slightly increased value of the energy costs of $\Delta E_{\text{edge}} \approx 2.7\,\text{meV}/a$ at an edge, single- and multi-domain states would already be energetically degenerate in a triangular island.

In the present system, the movement of domain walls is suppressed compared to domain walls in a ferromagnetic sample since it requires a rearrangement of the nanoskyrmion lattice. This involves an energy barrier which is reflected by the rather inhomogeneous energy distribution within the nanoskyrmion lattice and the domain wall as shown in Fig. 6.8. The images provide in a color scheme the local contributions of the various energy terms to the total energy of the atomic magnetic moments. A vertical aligned domain wall in the middle of the images separates two different rotational domains of the nanoskyrmion lattice on the left and right side of the image from each other. The magnetic unit cells of the two rotational domains are indicated for convenience. The most obvious observation is the local competition of the nearest-neighbor exchange interaction and four-spin interaction. Regions within the domain wall,

which are particularly favorable for one of the two interactions, are unfavorable for the other interaction. Apart from this, the energy costs for the formation of a domain wall remain hidden in the spatial inhomogeneity of the energies.

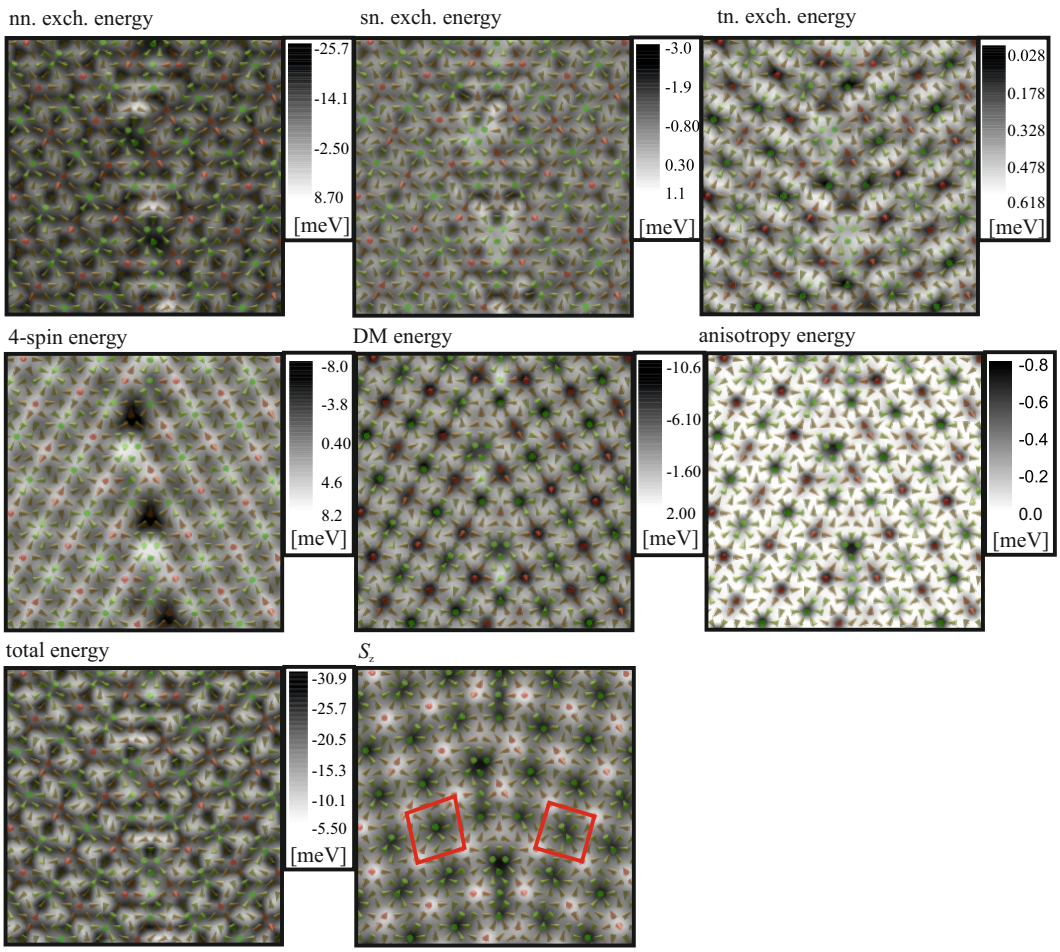

Figure 6.8: Color maps of atomic energies and perpendicular magnetization. A vertical aligned domain wall separates two rotational domains of the nanoskyrmion lattice. The magnetic unit cells are indicated for the two rotational domains for convenience. The temperature of the system is $T = 0.1\,\mathrm{K}$.

6.2.3 Ferromagnetic edge

Due to the deposition of ferromagnetic Ni islands onto the monolayer of Fe on Ir(111), the behavior of the nanoskyrmion lattice in the presence of a ferromagnetic edge could be studied experimentally as discussed in section 6.1. In order to investigate this issue with the Monte Carlo model, a system with the shape of a half circle is chosen as a starting point to avoid concurrent influences of multiple edges. The spins at the straight edge are fixed ferromagnetically in a direction perpendicular to the system plane. After cooling the system from a value above T_c to $T = 1\,\mathrm{K}$, one side and not a diagonal of the square nanoskyrmion lattice is parallel to the straight edge (Fig. 6.9 a). This domain is dissimilar to the previously observed rotational domains which can be verified by the corresponding atomic spin structures shown in Fig. 6.9 b and Fig. 6.3 a. To estimate the energy cost of this new rotational domain, a larger sample is selected with two ferromagnetic edges above and below and open boundaries left and right, see Fig. 6.9 c. From the enclosed nanoskyrmion lat-

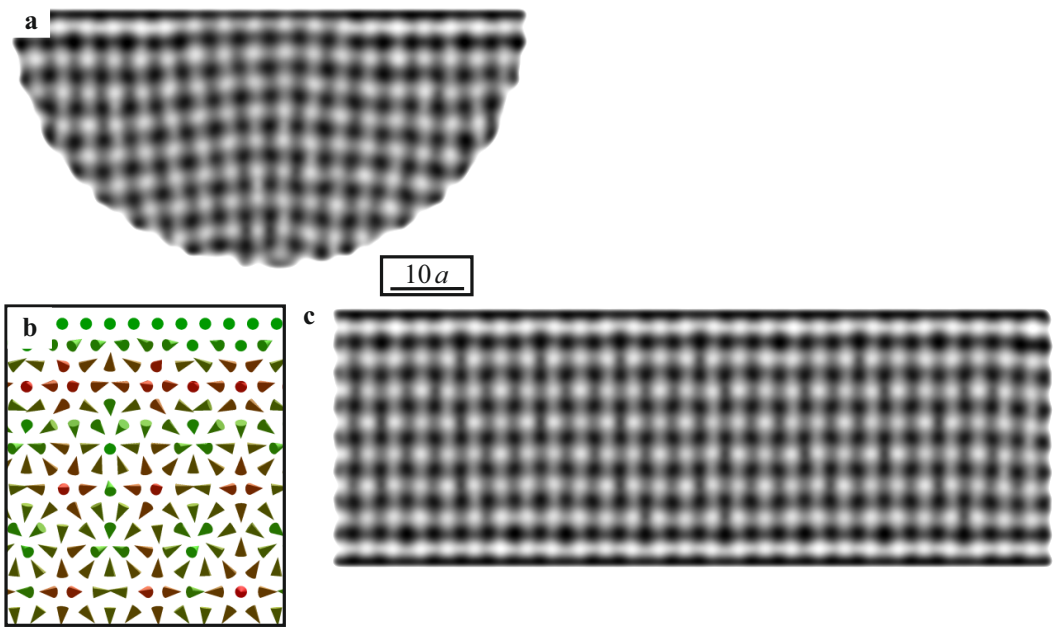

Figure 6.9: Ferromagnetic edges. (**a**) Perpendicular magnetic contrast of the nanoskyrmion state on a half-disk with a ferromagnetic edge as obtained from MC calculations at $T = 1\,\mathrm{K}$ [121]. (**b**) Spin structure at the upper ferromagnetic edge, taken from (c). (**c**) Magnetic stripe at $T = 0.1\,\mathrm{K}$ with two ferromagnetic edges (top/bottom) and open boundary conditions left and right.

tice, one obtains an estimate for the energy cost with respect to the common rotational domains of $\approx 0.25\,\mathrm{meV/atom}$.

6.3 Conclusion

It was found that the orientation of the nanoskyrmion lattice in Fe/Ir(111) can be controlled by tailoring edge properties. In particular, a diagonal of the magnetic unit cell is coupled parallel to a close-packed edge of an Fe island and one side of the magnetic cell is coupled parallel to a ferromagnetic edge. Corresponding behavior was observed both in experimental and Monte Carlo investigations. From the Monte Carlo calculations, the local energy cost at an edge of an Fe island due to a rotation of the nanoskyrmion lattice was determined as $2.2\,\mathrm{meV\,a^{-1}}$ and the energy cost of a domain wall between different rotational domains of the nanoskyrmion lattice was deduced to be $3.1\,\mathrm{meV\,a^{-1}}$. These results allow for the conclusion that the domain formation in triangular islands is governed by mismatching symmetries of island shape and skyrmion lattice. Despite the lower energy of a single-domain state, multi-domain states arise by the combined effect of entropy and an intrinsic domain wall pinning, which results from the skyrmionic character of the spin texture.

The results about the confinement effects of this chapter are specific for the nanoskyrmion lattice in Fe/Ir(111) which exhibits a square magnetic unit cell due to the influence of the four-spin interaction. In most systems, the four-spin interaction is negligible and the skyrmions appear in a close packed lattice with a six-fold symmetry. Hence, these systems may show different confinement effects which is an interesting question for future investigations.

Chapter 7

Skyrmions in inhomogeneous environments

The previous chapters 5 and 6 dealt with influences of material boundaries on spin-spiral and skyrmion states. In contrast to that, this chapter discusses effects that result from spatial inhomogeneities of material parameters within a skyrmionic material. First, linear variations of energy parameters along a sample system are studied and employed to determine phase space and equilibrium properties of skyrmions in section 7.1. Second, periodic spatial modulations of energy parameters, that lead to the formation of non-axisymmetric skyrmion states, are investigated in section 7.2. Qualitative similarities with recent experimental observations on the magnetic triple layers Fe/Ir(111) are shown.

Parts of this chapter contributed to the following articles:

- A. Siemens, Y. Zhang, J. Hagemeister, E. Y. Vedmedenko & R. Wiesendanger. Minimal radius of magnetic skyrmions: statics and dynamics. New J. Phys. **18** 045021 (2016)

- J. Hagemeister, E.Y. Vedmedenko & R. Wiesendanger. Pattern formation in skyrmionic materials with anisotropic environments. Phys. Rev. B **94** 104434 (2016).

7.1 Linear spatial variation of energy parameters

Starting point for the Monte Carlo calculations presented in the following is the standard effective Hamiltonian

$$H = -\sum_{<i,j>} J_{ij}\mathbf{S}_i \cdot \mathbf{S}_j - \sum_{<i,j>} \mathbf{D}_{ij} \cdot (\mathbf{S}_i \times \mathbf{S}_j) - K\sum_i (S_i^z)^2 - \mu \sum_i \mathbf{B} \cdot \mathbf{S}_i \tag{7.1}$$

for skyrmionic systems. The interaction parameters provide the respective energies per bond and the anisotropy energy is set to zero, i.e. $K = 0$, for simplicity. Two-dimensional hexagonal lattices with a rectangular boundary shape and open boundary conditions are used. The value of D/J is varied along one dimension of a magnetic sample which has the result that ferromagnetic, skyrmionic and spin-spiral phases may be visible simultaneously at low temperatures within this sample. This offers a convenient way to determine phase boundaries between the different magnetic states as will be discussed in section 7.1.2. For this purpose, a software tool is needed to automatize the identification of positions and sizes of the skyrmions within a given magnetic sample.

7.1.1 Skyrmion position and size

The positions and sizes of magnetic skyrmions were obtained with a self-written Python script as explained in the following with the aid of the magnetic sample presented in Fig. 7.1. The value of J is varied linearly along the sample such that $D/J = 2$ at the left side of the sample and $D/J \approx 0.27$ at the right side of the sample. D is constant along the sample, $\mu B/D = 0.3$ and $k_\mathrm{B}T/D = 8.6 \cdot 10^{-3}$. The displayed color map of the perpendicular component of the magnetization exhibits various skyrmions. In a first step, local minima in the magnetization were determined in order to obtain approximate values for the positions of the skyrmion centers $(x_\mathrm{c}, y_\mathrm{c})$. Thereafter, these were used as initial values for fit parameters in two-dimensional approximation processes of the skyrmions. The polar angle Θ was approximated by

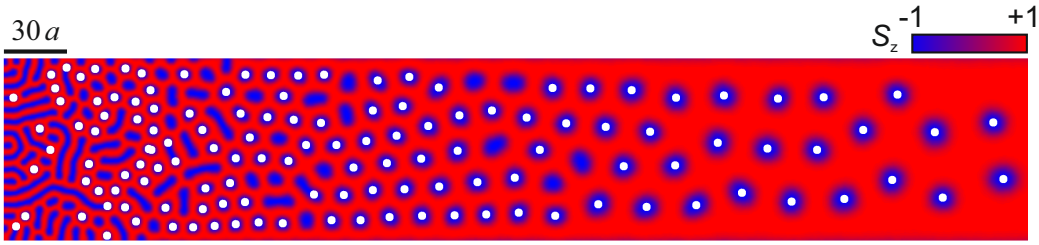

Figure 7.1: Skyrmion positions. Magnetic sample with skyrmions whose positions were obtained automatized with a Python script. The obtained skyrmion positions are indicated by white points.

$$\Theta = |\arcsin\left(\tanh\left(\frac{\sqrt{(x-x_\mathrm{c})^2+(y-y_\mathrm{c})^2}+c}{w/2}\right)\right) \tag{7.2}$$

$$+\arcsin\left(\tanh\left(\frac{\sqrt{(x-x_\mathrm{c})^2+(y-y_\mathrm{c})^2}-c}{w/2}\right)\right)| \tag{7.3}$$

with the fit parameters $(x_\mathrm{c}, y_\mathrm{c}, c, w)$. This kind of formula was originally used for the description of 360° domain walls [122] but it was also successfully applied to magnetic skyrmions [57]. With the fit parameters c and w, the radius of the skyrmions can be determined as the radius of the region in which the magnetization locally has a perpendicular component in the opposite direction of the ferromagnetic background. The approximation process was performed locally to the skyrmion texture. For this purpose the region within a radius of $20\,a$ around an initial guess for $(x_\mathrm{c}, y_\mathrm{c})$ was considered which was a somewhat arbitrary choice but sufficiently large to fully contain the respective skyrmion. However, the size of the region gave rise to the possibility that parts of neighboring skyrmions were included which was taken care of in a second step. Starting from a skyrmion center $(x_\mathrm{c}, y_\mathrm{c})$ in which the polar angle is locally minimal, the polar angle should strictly increase with an increasing distance to the center. All atomic magnetic moments that did not fulfill this requirement were removed for the approximation process. Fig. 7.2 shows the result of the approximation of an exemplary skyrmion with $D/J = 0.14$, $\mu B/J = 0.042$ at $k_\mathrm{B}T/J = 1.2 \cdot 10^{-3}$. For the fit parameters, $c = 3.96\,a$ and $w = 9.21\,a$ were obtained which yield a skyrmion radius of $5.22\,a$.

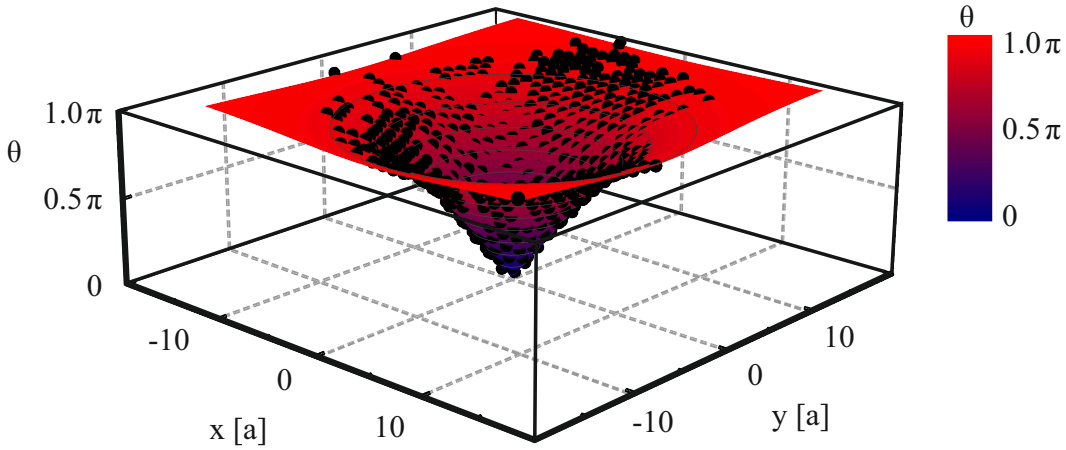

Figure 7.2: Two-dimensional fit of a magnetic skyrmion. The choice of lateral axes is such that the skyrmion center is at (0,0).

7.1.2 Phase diagrams

Basis for the determination of phase diagrams was the observation that smooth parameter changes along a sample give rise to the simultaneous formation of ferromagnetic, skyrmionic and spin-spiral states within one sample as shown exemplarily in Fig. 7.3. In this case, the parameter ratio D/J was linearly varied in the interval $(0, 2)$ and $\mu B/J = 0.7$ with J kept constant. The magnetic state was obtained after a reduction of the temperature to $k_{\mathrm{B}}T/J = 8.6 \cdot 10^{-3}$ in 20 steps each consisting of 75,000 Monte Carlo steps. In the region of small D/J, the system is ferromagnetic while it exhibits spin-spirals in the region of large D/J. In the intermediate region, skyrmions of different lateral sizes are observable. The search for positions and sizes of the the skyrmions was performed automatized with a python script as explained in the previous section 7.1.1. Clearly, the radii of the skyrmions do not possess a constant value along the sample but they exhibit a maximum that seems to mark the point where a transition between skyrmion gas and skyrmion lattice takes place (Fig. 7.3). This is in good agreement with A. Butenko's statement in her doctoral thesis that the skyrmion size should be proportional to D/H for an isolated skyrmion and proportional to A/D in a skyrmion lattice [123]. Hence, the variation of the energy parameters along a large sample proves to be a convenient method to determine the boundaries between different magnetic states in skyrmionic materials. Consequently, phase diagrams as shown in Fig. 7.4 a

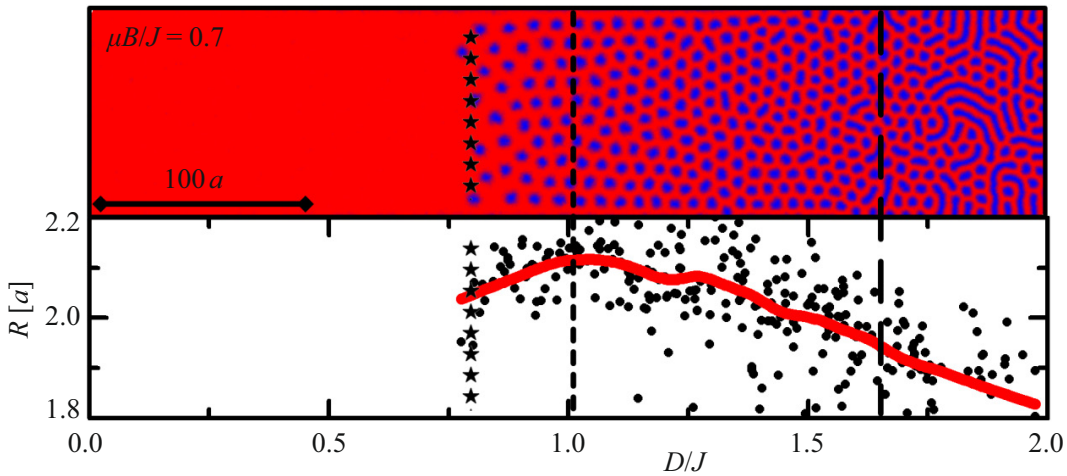

Figure 7.3: Linear variation of Dzyaloshinskii-Moriya interaction parameter. The variation of D along the sample causes locally the formation of ferromagnetic, skyrmionic and spin-spiral states.

and 7.4 b can be obtained, in which the color maps provide a representation of the skyrmion density ρ which is given by the ratio of the effective area locally occupied by the skyrmions and the area occupied by skyrmions of same size in a close packed lattice. The black lines, which are also included in Fig. 7.3, indicate the phase boundaries. For the determination of the phase diagrams, samples of large size with $\approx 300,000$ lattice sites were used and small variations of the D/J ratio were imposed in order to avoid distortions of the skyrmions, which are the topic of section 7.2. Depending on the skyrmion size, $\Delta(D/J)/(D/J)$ was chosen in the range of about $(0.03\% - 0.5\%)$ per lattice constant in order to avoid large parameter changes within a skyrmion.

Figures 7.4 c and d provide an overview of the skyrmion radius as a function of the position in phase space showing that a large external magnetic field and a large ratio of D/J leads to the formation of skyrmions with a small later size on the order of the lattice constant. The question about the smallest possible size of a stable skyrmion on a discrete lattice arises. In order to investigate this issue, a closer look is taken at the skyrmion radius at the phase boundary of the skyrmion lattice phase towards the FM phase (Fig. 7.5 a). Unsurprisingly, the radius decreases with increasing ratio D/J. It seems that the behavior can be described by a hyperbolic function with an offset of $0.52\,a$ being the smallest radius for a stable skyrmion at infinite D/J.

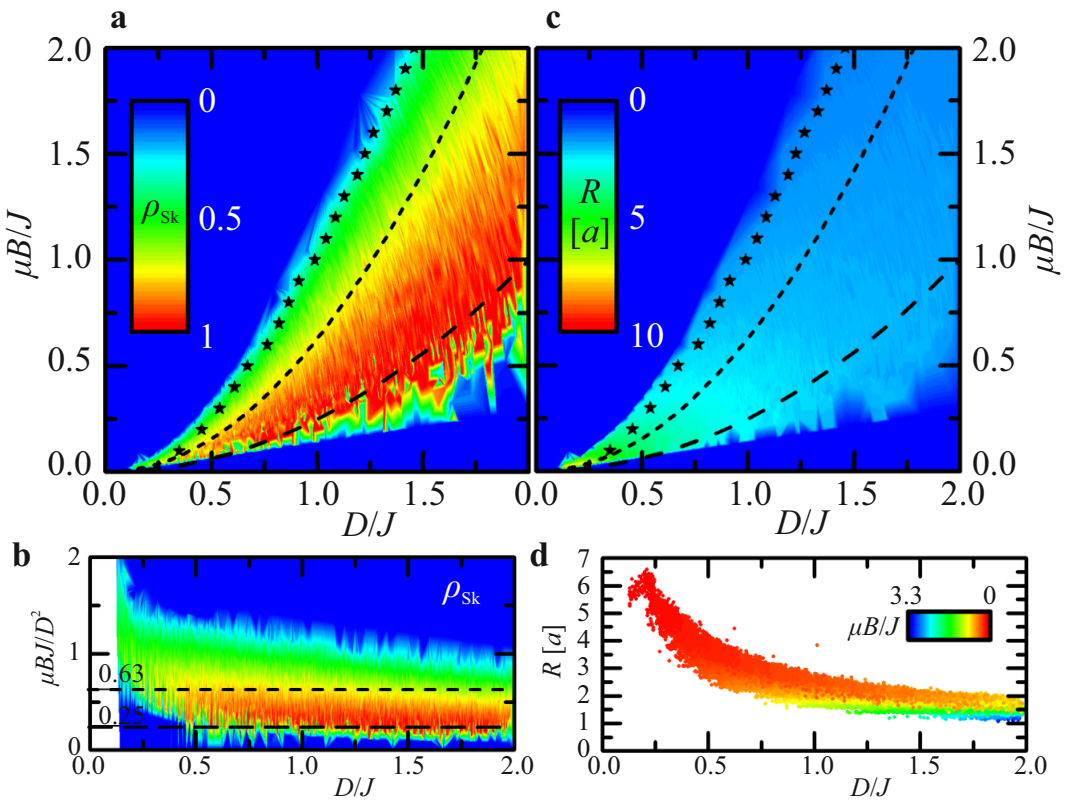

Figure 7.4: Phase diagrams. (**a**), (**b**) Phase diagrams using the skyrmion density ρ as an order parameter at $k_B T/D = 8.6 \cdot 10^{-3}$. (**c**), (**d**) Skyrmion radii as a function of the position in phase space.

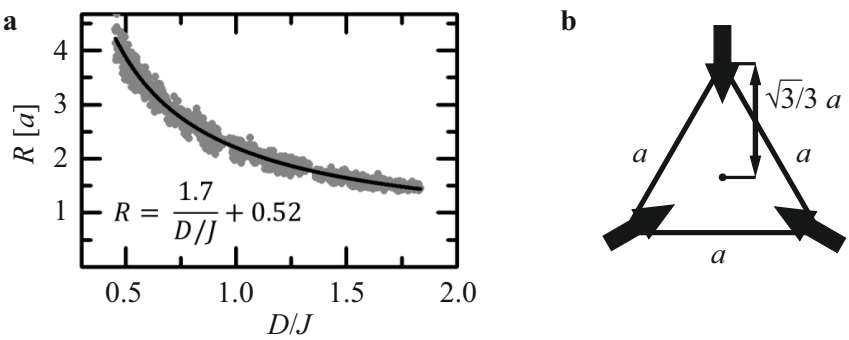

Figure 7.5: Skyrmion radii. (**a**) Skyrmion radius R at the phase boundary of the skyrmion lattice phase towards the FM phase. (**b**) Theoretical consideration about the smallest possible skyrmion radius on a hexagonal lattice yielding $R_{\min} = \sqrt{3}/3\, a \approx 0.58\, a$.

For a comparison, the size of an axisymmetric skyrmion, whose center is in the middle of three neighboring atoms, is considered. Such a skyrmion would vanish along with its topological charge when it becomes so small that the magnetic moments of three neighboring atomic sites lie in the plane and point towards the position of the former skyrmion center (Fig. 7.5 b). This theoretical model provides an estimation for the smallest possible skyrmion radius of $0.58\,a$ which is with a deviation of about 10% quite similar to the one stated above. This finding is in contrast to the description of skyrmions in the continuum model in which they can become infinitesimal small.

7.2 Periodic spatial modulation of energy parameters

A broad range of theoretical and experimental investigations have been conducted with the consideration of axisymmetric skyrmions in isotropic environments. However, one naturally observes a huge variety of anisotropic behavior in many experimentally relevant materials [124, 125, 126, 127]. Consequently, the experimental observation of skyrmions which are deformed with respect to the axisymmetric shape was reported for chiral bulk magnets with crystal lattice strain recently [128]. Skyrmionic systems with interface induced Dzyaloshinskii-Moriya interaction typically consist of a single or multiple atomic, magnetic layers of different atomic species which are deposited succeedingly onto a non-magnetic supporting crystal [22, 100, 102, 129, 41]. In principle, various crystal structures are possible but here, the focus is on hexagonal lattices due to their current relevance in experimentally investigated systems [21, 22, 117]. Typically, hexagonal lattices provide a rather isotropic environment (see chapter 5) but the combination of materials with different lattice constants can give rise to lattice strain and reconstructions in the magnetic surface layers. Hence, anisotropic environments can also emerge in skyrmionic systems with interface induced Dzyaloshinskii-Moriya interaction as has been discussed recently for the double [117] and triple [130] atomic layers of Fe on Ir(111). The key findings for these two materials will be presented in the following because they were the motivation for the subsequent MC studies.

7.2.1 Double and triple layers of Fe on Ir(111)

The first atomic layer of Fe on Ir(111) grows pseudomorphically and exhibits a nanoskyrmion lattice [21] in the fcc stacking and a hexagonal spin texture in the hcp stacking [118]. In the second and third atomic layers of Fe on Ir(111), areas with reconstruction lines that form due to the mismatch of lattice constants can be found (Fig. 7.6 a). The reconstruction lines are aligned parallel with respect to each other and perpendicular to a close packed atomic row of the Ir(111) surface. They have a periodicity of about 5.2 nm [117] in the double layers and $(4-9)$ nm [130] in the triple layers. In both material systems, cycloidal spin-spirals were found with periodicities of 1.6 nm [117] in the double and 3.8 nm [130] in the triple layers at zero magnetic field. The spin-spiral wave fronts exhibit an overall alignment parallel to a symmetry equivalent $[10\bar{1}]$ direction. Interestingly, the wave fronts are spatially modulated (Fig. 7.6 b) with the periodicity of the dislocation lines which could be explained by a

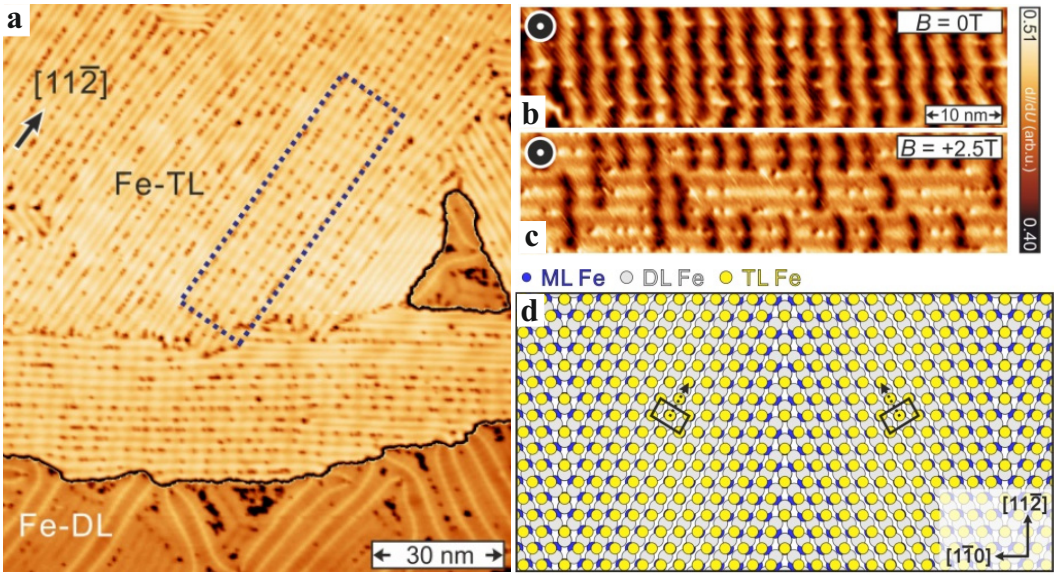

Figure 7.6: Triple atomic layers of Fe on Ir(111). The figures are reprinted by permission from Macmillan Publishers Ltd: [NATURE NANOTECHNOLOGY] (Ref. [130], url), copyright (2016). (**a**) Constant-current image of atomic layers of iron on Ir(111) obtained with a spin-polarized scanning tunneling microscope. (**b**), (**c**) $\mathrm{d}I/\mathrm{d}U$ map of the area marked in **a** at 0 T and 2.5 T perpendicular external magnetic field. The measurement parameters are $U = -0.7\,\mathrm{V}$, $I = 1\,\mathrm{nA}$ and $T = 7.8\,\mathrm{K}$. (**d**) Structural model for the atomic triple layer of iron on Ir(111).

structural model for the atom positions [117, 130]. P.-J. Hsu et *al.* point out in Ref. [117] that previous studies on epitaxial growth showed a preference of bcc materials to form a bcc(110)-like interface with a fcc(111) surface and provide Ref. [131, 132, 133] for comparison. They deduce a compression of the second and third layers by a few percent and present the resulting model for the atomic structure as shown in Fig. 7.6 d [130]. Regions with bcc(110)-like areas are indicated by black rectangles which are believed to locally guide the spin-spiral wave fronts. A minimal opening angle of the zigzag wave fronts of 117° can be deduced for the double layer system and similar values are expected for the triple layer system. The spin-spiral state in the double layer system is stable up to 9 T perpendicular external magnetic field. However, skyrmionic objects with a non-vanishing topological charge could be obtained in the triple layer system with magnetic fields of about 2.5 T (Fig. 7.6 c) [130]. They are non-axisymmetric and thus exhibit a different geometry from the initially theoretically proposed axisymmetric magnetic skyrmions [12].

7.2.2 Model for Monte Carlo calculations

Starting point for the MC calculations is the standard effective Hamiltonian

$$H = -\sum_{<i,j>} J_{ij}\mathbf{S}_i \cdot \mathbf{S}_j - \sum_{<i,j>} \mathbf{D}_{ij} \cdot (\mathbf{S}_i \times \mathbf{S}_j) - \sum_i K_i(\mathbf{e}_{K_i} \cdot \mathbf{S}_i)^2 - \mu \sum_i \mathbf{B} \cdot \mathbf{S}_i \tag{7.4}$$

consisting of the exchange energy, the DM energy, the magnetocrystalline anisotropy and the Zeeman energy. Here, all interaction parameters are given per bond. The classical three-dimensional spins $\mathbf{S}_i$ of unit length can rotate freely on the unit sphere. The corresponding phase space with an isotropic energy parameter environment is well known [15, 103, 104] (see also section 2.2). In order to summarize, a spin-spiral state with a fixed rotational sense is the ground state at low temperatures and zero external magnetic field in a broad parameter range. The application of a perpendicular external magnetic field can cause a transition from the spin-spiral state to a skyrmionic state at an intermediate field strength and eventually the saturated ferromagnetic state is reached at a sufficiently large field.

For the following investigations, a nearest neighbor DM interaction strength $|\mathbf{D}| = D$ is considered and for symmetry reasons, the DM-vectors are chosen to lie in the plane of the magnetic film and to be perpendicular to the connection line between neighboring spins [58]. Two-dimensional triangular lattices with the lattice constant a are used and the behavior of multiple magnetic layers is mimicked by spatial modulations of the parameters of the anisotropy energy and exchange interaction.

7.2.3 Modulation of exchange interaction parameter

Similar to previous investigations [134, 135], effective nearest-neighbor exchange interaction parameters J_{ij} are introduced. The earlier model is extended in order to modulate the strength of the exchange coupling not only as a function of the orientation of the respective bond but as a generalization also of the position in the lattice according to the following description

$$J_{ij}^2(\mathbf{r}_i, \mathbf{r}_j) = \left(j_{\mathrm{M}}^2 \cdot \frac{|\mathbf{e} \cdot \mathbf{r}_{ij}|^2}{a^2} + j_{\mathrm{m}}^2 \cdot \frac{|\mathbf{e} \times \mathbf{r}_{ij}|^2}{a^2} \right) \tag{7.5}$$

$$\mathbf{e}^T(\alpha) = (\cos(\alpha), \sin(\alpha), 0) \tag{7.6}$$

$$\alpha = \alpha_{\max} \cdot \sin\left(\frac{2\pi}{\lambda} \cdot \left[\frac{1}{2}(\mathbf{r}_i + \mathbf{r}_j) \cdot \mathbf{e}_{[10\bar{1}]} \right] \right) \tag{7.7}$$

The equation 7.5 is equivalent to the parametrization of an ellipse with the semi-major axis j_{M} and semi-minor axis j_{m} in the case of $j_{\mathrm{M}} > j_{\mathrm{m}}$. The ellipse lies within the plane of the magnetic film and the direction of the major axis $\mathbf{e}$ is locally rotated by the angle α with respect to the $[10\bar{1}]$ direction. $\boldsymbol{r}_{ij}$ is the vector connecting the lattice sites i and j. The choice of unequal parameters j_{M} and j_{m} provides an anisotropic environment with an exchange interaction strength which then depends on the crystallographic orientation of a bond. The angle $\alpha_{\max}$ and the period λ in units of a can be used to create a periodic modulation of the anisotropic environment of the exchange-interaction along the crystallographic direction $[10\bar{1}]$.

Figure 7.7 a shows the perpendicular component of the magnetization of a spin-spiral state for the modulation period $\lambda = 20\,a$ and modulation angle $\alpha_{\max} = 29°$. The interaction strengths are $j_{\mathrm{m}}/j_{\mathrm{M}} = 0.5$ and $j_{\mathrm{m}}/D = 1.6$ and the anisotropy is $K = 0$. The temperature of the system was decreased from

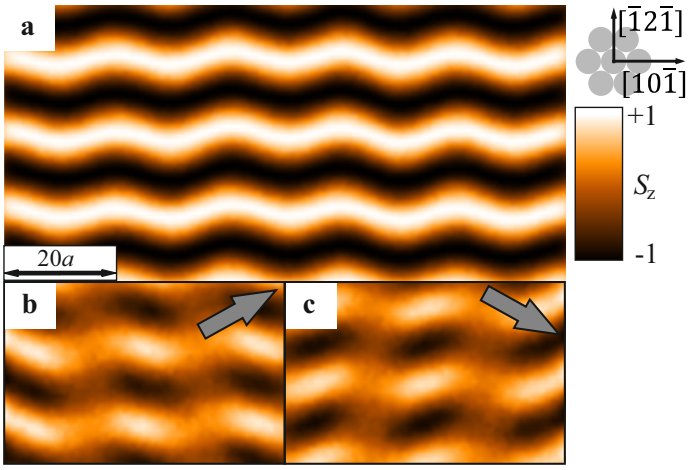

Figure 7.7: Spatial modulation of exchange constant. Spin-spiral state with zigzag shaped wave fronts on a triangular lattice with periodic boundary conditions in the [$\bar{1}2\bar{1}$] direction. The color maps give a linear scheme of the projection of the magnetization onto a given direction which is perpendicular to the plane in (**a**) and parallel to the gray arrows in (**b**) and (**c**).

$k_\mathrm{B}T/D = 1.7$ to $k_\mathrm{B}T/D = 8.6 \cdot 10^{-3}$ using 20 temperature steps with 10^5 Monte Carlo steps each ensuring that the global energy minimum is reached. The resulting spin-spirals have a wave length of approximately $14\,a$. The wave fronts are on average aligned in parallel to the [$10\bar{1}$] direction and the periodicity of their zigzag pattern is in agreement with the modulation period of the exchange energy. Part of the spin contrast vanishes (Fig. 7.7 b, c) when calculating the projection of the in-plane component of the magnetization onto the directions which enclose an angle of $\pm\alpha_\mathrm{max} = \pm 29°$ with the [$10\bar{1}$] direction. This finding can be verified by the investigation of the incidence n_ϕ of the spins' azimuthal angles ϕ with respect to the [$10\bar{1}$] direction which is shown in Fig. 7.8. With a vanishing modulation amplitude $\alpha_\mathrm{max} = 0$, the spins are aligned in the

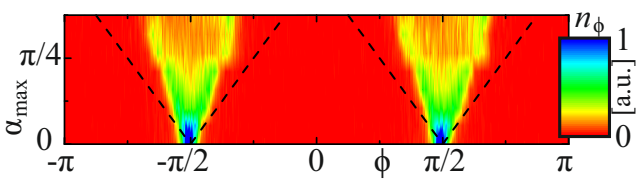

Figure 7.8: In-plane angle of magnetic moments. The frequency of the azimuthal angle ϕ with respect to the [$10\bar{1}$] direction. The dotted lines provide $\pm\frac{\pi}{2} \pm \alpha_\mathrm{max}$.

plane given by the system's normal vector and the $[\bar{1}2\bar{1}]$ direction. An increase of the modulation amplitude $\alpha_{\max}$ causes the single peaks at $\pm 0.5\,\pi$ to split into double peaks with a distance of approximately $\alpha_{\max}$. Consequently, the spins are predominantly perpendicular to the local spin-spiral wave fronts as expected for cycloidal spin-spirals [11].

Following this, the modulation of the exchange energy onto the skyrmion state is investigated. Fig. 7.9 a-f show the magnetic ground states which are obtained when the temperature of the system is reduced with applied constant magnetic fields. Except for the magnetic field, all simulation parameters are chosen to be the same as before. The spin-spirals break up at the magnetic field $\mu B/D = 0.237$ and elongated zigzag structures are created which eventually shrink at magnetic field strengths larger than $\mu B/D = 0.284$. No individual

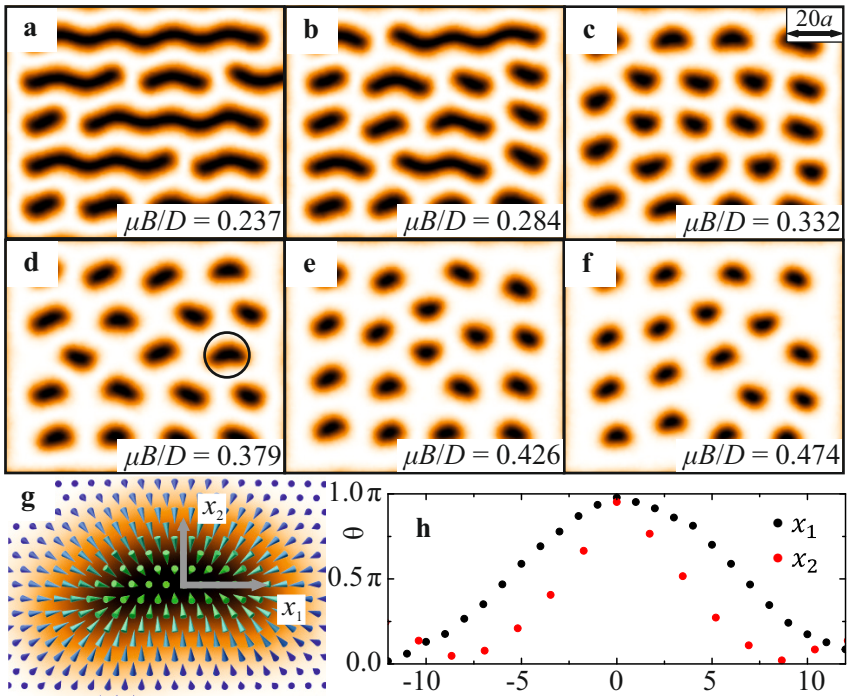

Figure 7.9: Spatial modulation of exchange energy. (**a-f**) Perpendicular contrast of the magnetic pattern which is obtained under application of a perpendicular magnetic field to a zigzag spin-spiral state with open boundary conditions. (**g**) Spin texture of the magnetic object marked in (d). (**h**) Profiles of the polar angle for the magnetic texture in (g).

magnetic objects are observed for fields larger than $\mu B/D = 0.62$. The magnetic objects possess a unique rotational sense and yield a non-vanishing topological charge Q. Furthermore, the magnetic objects are non-axisymmetric as investigated exemplarily for the marked spin texture in Fig. 7.9 d. Fig. 7.9 g, h show the atomic spin configuration and the corresponding line profiles of the spins' polar angles. The profiles of the polar angle of the local magnetization direction clearly show an elongation of the structure into the $[10\bar{1}]$ direction compared to the $[\bar{1}2\bar{1}]$ direction.

7.2.4 Modulation of anisotropy energy parameter

It is known that the anisotropy energy can in principle vary locally in thin magnetic films [136]. In the following, the effects of a spatial modulation of the anisotropy energy in combination with an isotropic environment of the exchange and Dzyaloshinskii-Moriya interaction is investigated. Stripe-like regions with an easy in-plane axis parallel to the $[\bar{1}2\bar{1}]$ direction and easy in-plane axis parallel to the $[10\bar{1}]$ direction are introduced with the widths $dl_1 = 18\,a$ and $dl_2 = 2\,a$ which are periodically repeated along the $[10\bar{1}]$ direction with a periodicity of $20\,a$. In Fig. 7.10 a, a sketch of the atomic lattice is given indicating the anisotropy axis for each lattice site. The same anisotropy energy constant of $K/D = 0.6$ is assumed for the two regions and $J/D = 2.1$ is chosen. Fig 7.10 b-d show the magnetic ground states for different magnetic fields after the reduction of the temperature in the same fashion as before. The spin-spiral period at zero magnetic field is approximately $15.8\,a$ and the wave fronts are aligned in parallel to the $[10\bar{1}]$ direction. With an applied magnetic field of $\mu B/D = 0.52$, an ordered state of elongated magnetic objects is formed. Their centers lie in the middle of the regions that possess an anisotropy axis parallel to the $[\bar{1}2\bar{1}]$ direction and their elongation into the $[10\bar{1}]$ direction is determined by the areas in which the anisotropy axis is parallel to the $[10\bar{1}]$ direction. This finding is verified exemplarily for a single magnetic object which is highlighted in Fig. 7.10 c. Fig. 7.10 e shows the corresponding spin configuration and Fig. 7.10 f displays the profiles of the polar angle of the magnetization along two perpendicular crystallographic axes. One can clearly discern a lateral size of the magnetic object parallel to the $[10\bar{1}]$ direction of about $20\,a$. In other words, the modulation of the anisotropy energy aligns

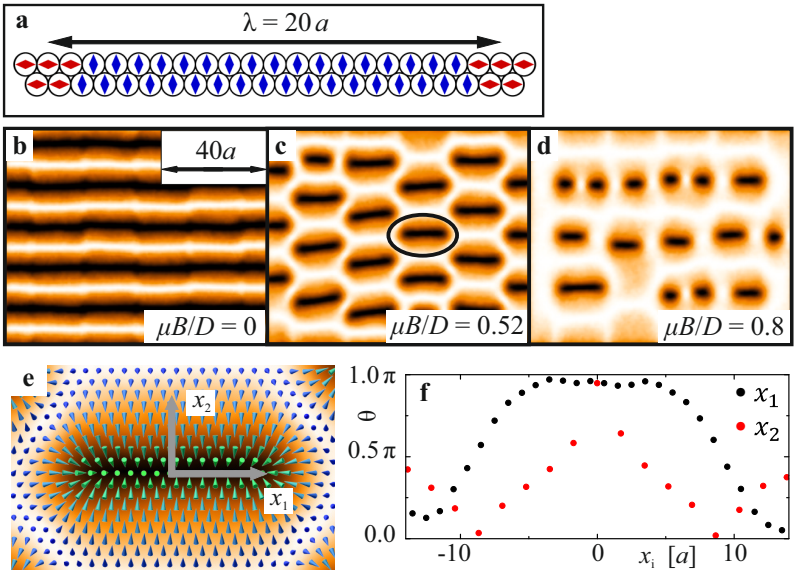

Figure 7.10: Spatial modulation of anisotropy energy. (**a**) Sketch of the atomic lattice in the top view indicating regions of easy in-plane anisotropy axes parallel to the $[10\bar{1}]$ (red) and $[\bar{1}2\bar{1}]$ (blue) direction. (**b**)-(**d**) Perpendicular magnetic contrast of the ground state in an applied magnetic field. (**e**) Spin configuration of a skyrmion marked in (c). (**f**) Profiles of the polar angle through the magnetic texture shown in (e).

the magnetic objects on tracks along the $[\bar{1}2\bar{1}]$ direction. For magnetic fields larger than $\mu B/D \approx 0.7$, a part of the magnetic objects splits into two smaller parts and eventually the ferromagnetic state is reached at fields larger than $\mu B/D \approx 0.9$.

7.2.5 Formation of skyrmionic tracks

In the following, it is shown that linearly aligned skyrmionic structures along a track can be formed by a spatial modulation of the energy parameters in a 2D model system. For this purpose, the effects of the modulation of the exchange and anisotropy energy are combined with an isotropic environment of the DM-interaction on the magnetic ground state of skyrmionic systems. The parameters for the exchange and Dzyaloshinskii-Moriya interaction are chosen as in the simulations for Fig. 7.7 and 7.9. Additionally, a spatial modulation of an easy in-plane anisotropy axis with the energy $K/D = 0.6$ similar to simulations for Fig. 7.10 is assumed but the anisotropy axes are partly

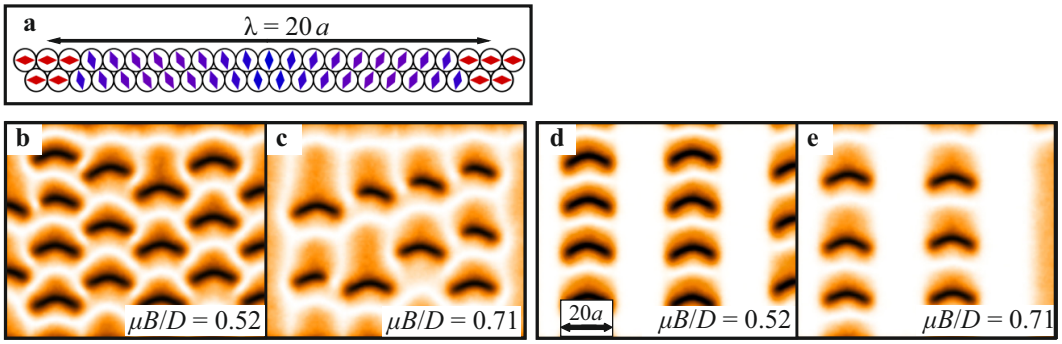

Figure 7.11: Skyrmion tracks. (**a**) Sketch of the atomic lattice in the top view indicating the spatial modulation of the direction of the easy anisotropy axis. (**b**),(**c**) Perpendicular contrast of the magnetic ground states at different magnetic fields. The spatially modulated anisotropy energy used for Fig. 7.10 is combined with the anisotropic environment of the exchange interaction used in Fig. 7.7, 7.9 and an isotropic environment of the DM-interaction. (**d**),(**e**) Formation of skyrmion tracks by a spatial modulation of local magnetic anisotropy as explained in the text.

adopted to follow the modulation of the exchange interaction as indicated in Fig. 7.11 a, i.e. they are locally parallel to the minor axis of the exchange modulation scheme. For two magnetic fields, the magnetic ground states at low temperatures are shown in Fig. 7.11 b and 7.11 c. One observes ordered bent non-collinear spin states with a non-vanishing topological charge at the magnetic field $\mu B/D = 0.52$ which appear at $\mu B/D \approx 0.71$ with a larger spatial separation and are not observed for $\mu B/D \gtrsim 0.85$. As before, the magnetic objects are aligned along tracks parallel to the $[\bar{1}2\bar{1}]$ direction. However, the magnetic objects of neighboring tracks influence each other in the current status in such a way that they could not be moved independently from each other parallel to the $[\bar{1}2\bar{1}]$ direction. Every second track can be excluded by locally substituting the easy in-plane axis by an easy out-of-plane anisotropy axis with the energy $K/D = 0.6$. The resulting magnetic equilibrium skyrmion-like patterns are confined to spatially separated tracks parallel to the $[\bar{1}2\bar{1}]$ direction (Fig. 7.11 d and 7.11 e) along which they can be moved as discussed in section 7.2.6. In real systems, this creation of tracks could be achieved by nanostructuring of the surface. Next, a closer look at the spatial distribution of the topological charge and the energy densities for the obtained magnetic objects reveals that the largest contributions to the topological charge arise at

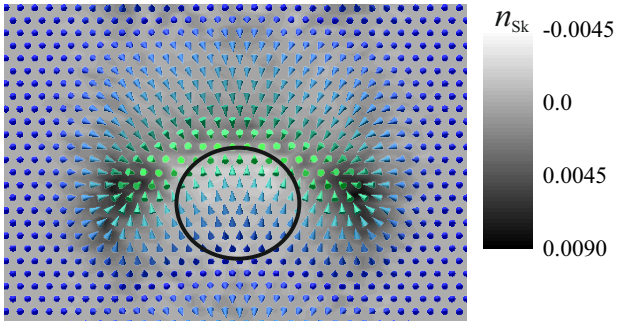

Figure 7.12: Topological charge. Spin structure and local skyrmion density for a magnetic object shown in Fig. 7.11 d. Within the marked area, topological charge of negative sign is acquired.

their ends and a contribution of opposite sign is acquired near the bend as can be observed in Fig. 7.12. The sum over the local contributions to the topological charge provides $Q = 1$ for each magnetic object. The exchange energy is large where the DM energy is small as in the region where the magnetic moments have a perpendicular component opposite to the external magnetic field (Fig. 7.13). The anisotropy energy is small in regions where the spins of

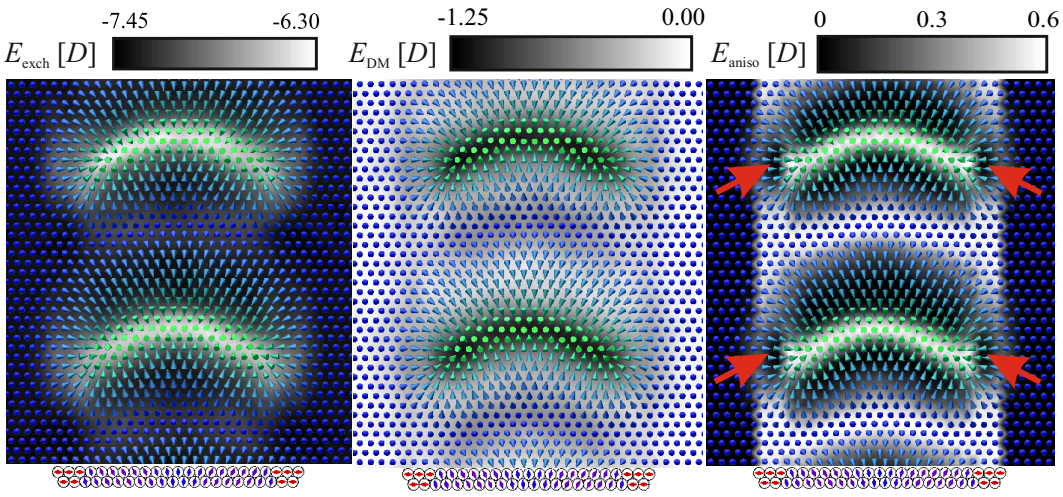

Figure 7.13: Energy densities. The energy densities of the exchange interaction E_{exch}, the DM interaction E_{DM} and the anisotropy energy E_{aniso} for two skyrmions shown in Fig. 7.11 d. In the bottom, the local orientations of the easy anisotropy axes are indicated (same as in Fig. 7.11 a). The red arrows indicate the regions in which the in-plane part of the magnetic objects pin to the edges of the magnetic track due to the anisotropy energy.

the magnetic objects lie predominantly within the magnetic layer which is expected when considering the choice of the directions for easy anisotropy axes as shown in the bottom of the individual images in Fig. 7.13 or in Fig. 7.11 a. Especially, the anisotropy energy is small at the ends of the elongated objects as indicated by the red arrows. The ends coincide with the narrow regions where the anisotropy axis is oriented parallel to the $[10\bar{1}]$ direction (see Fig. 7.13). This confines the skyrmionic structure spatially in the $[10\bar{1}]$ direction and additionally prevents them from decreasing their size in the $[10\bar{1}]$ direction due to their pinning effect. In between these regions, the easy anisotropy axis is locally parallel to the minor axis of the exchange energy modulation scheme which suppresses in combination with the direction dependent exchange energy parameter a splitting of the magnetic objects and stabilizes them over a relatively large magnetic field range. Hence, both the exchange interaction and the anisotropy energy are responsible for the stabilization of the elongated skyrmionic structures.

7.2.6 Skyrmion manipulation with magnetic tip

For technological applications it is desirable to not only align magnetic skyrmions along tracks but also to manipulate their lateral position. The skyrmions presented in Fig. 7.11 d and 7.11 e are aligned along tracks due to energy barriers resulting from a spatial modulation of the anisotropy landscape. However, this confinement is restricted to the $[10\bar{1}]$ direction and the skyrmions are free to be moved by a driving force along the $[\bar{1}2\bar{1}]$ direction which will be demonstrated in the following.

As a driving mechanism, the spin-polarized electric current from a magnetic tip is chosen. The influence can be described according to Ref. [96] (see also section 3.7) by an additional term H_T in the Hamiltonian for Monte Carlo calculations.

$$H_\mathrm{T} = -g \sum_i \mathbf{T}_i \cdot \mathbf{S}_i \tag{7.8}$$

$$\mathbf{T}_i = -I_0 \exp\left(-2\kappa\sqrt{(x_i - x_\mathrm{tip})^2 + (y_i - y_\mathrm{tip})^2 + h^2}\right) \cdot P \cdot \mathbf{m}_\mathrm{tip} \tag{7.9}$$

Therein, g is a coupling constant and T_i takes the spin-polarized current into

account. P is the tip polarisation, $\mathbf{m}_{\text{tip}}$ a unity vector parallel to the magnetization direction of the tip, κ the inverse decay length in vacuum, $\mathbf{r}_i = (x_i, y_i, 0)$ and $\mathbf{r}_{\text{tip}} = (x_{\text{tip}}, y_{\text{tip}}, h)$ the positions of the lattice sites, and the tip and I_0 the spin-polarized current. Typical values are chosen for the decay length $\kappa = 3\text{Å}^{-1}$ and the current $I_0 = 10^5 \frac{\mu_s}{\gamma D}$ [96]. The tip velocity is set to $1.5 \cdot 10^{-5}$ lattice constants per Monte Carlo step. The position of the tip is updated in intervals of 5000 Monte Carlo steps. The magnetization direction of the tip is chosen parallel to the skyrmion center and $g = 1$ and $h = 1a$ with a being the lattice constant. One finds that the tip is able to move the skyrmions of Fig. 7.11 d along the track at the temperature $k_{\text{B}}T/D = 0.086$. A picture sequence of this process is shown in Fig. 7.14. The tip is positioned above a skyrmion and when the tip is moved along the track, it moves the skyrmion along. This causes the other skyrmions to move as well. Since periodic boundary conditions were imposed in the direction of the tracks the skyrmions that leave the sample at one side reappear at the opposite side of the sample.

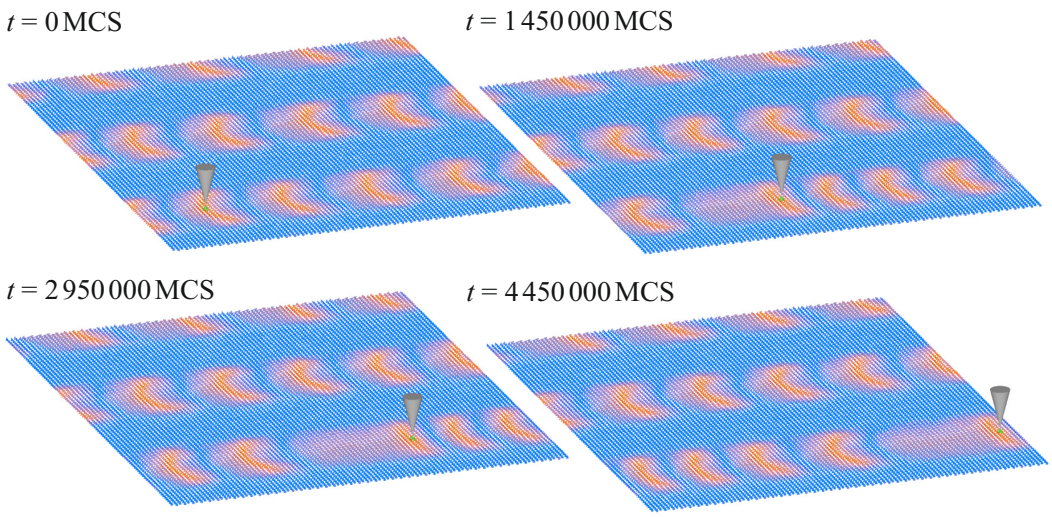

Figure 7.14: Skyrmion movement with a magnetic tip. Monte Carlo simulation of the movement of skyrmions with the tip of a spin-polarized scanning tunneling microscope. The skyrmions from Fig. 7.11 d are moved along a track. Due to periodic boundary conditions, the skyrmions that are pushed out of the sample to one side reappear at the opposite side.

7.3 Summary

Summing up, it was shown that small spatial gradients of material parameters provide a convenient method to determine phase diagrams of skyrmionic systems. Large spatial variations of material parameters can result in highly deformed magnetic objects with a non-vanishing topological charge. Apart from the non-axisymmetry, these objects possess main characteristics of skyrmions such as a small lateral size and the stabilization by a competition of DM interaction, exchange interaction and magnetocrystalline anisotropy energy. Moreover, the skyrmionic objects were aligned along tracks due to a spatial modulation of the energy landscape.

These results qualitatively reproduce the behavior of the magnetic states observed experimentally in the double and triple layers of Fe on Ir(111). In these material systems, a spatial modulation of material parameters is caused by periodic reconstruction features that originate from lattice strain due to a mismatch of lattice constants.

Additionally to this, the possibility to influence the lateral position of skyrmions by the tip of a spin-polarized scanning tunneling microscope is confirmed by Monte Carlo calculations. Previous experimental investigations already revealed that the position of skyrmions in the Pd/Fe bilayer on Ir(111) can be decisively manipulated by a scanning tunneling microscope in an indirect way by induced spatial displacements of pinning Co clusters on top of the surface [137].

Chapter 8

Summary

Magnetic skyrmions are regarded as promising candidates for bits of information in future data storage devices and many research activities are currently conducted to realize this goal. This thesis discussed fundamental properties of magnetic skyrmions as their thermal stability and behavior in confined geometries.

In chapter 4, a stochastic switching between ferromagnetic and skyrmionic state within Monte Carlo calculations was used to determine mean lifetimes of the two states as a function of magnetic field and temperature. Arrhenius-like dependences were found that give rise to activation energies in the range of about $(4.5-7.5)\,J$ for the skyrmion and $\approx 11\,J$ for the ferromagnetic state with J providing the exchange energy parameter per atomic bond. The material parameters were $D/J = 0.32$ and $K/J = 0.1$. The internal energy of the skyrmion was larger than that of the ferromagnet within the investigated range of external magnetic fields and the difference in the attempt frequencies was identified as the stabilizing mechanism of the skyrmion state. The calculations revealed an attempt frequency of the skyrmion which was about three orders of magnitude smaller than that of the ferromagnetic state. This discrepancy in the attempt frequencies could be linked to the entropy difference of the two states using the Eyring equation, finding that the skyrmion possesses a larger entropy compared to the ferromagnetic state. This may be explained by the fact that the skyrmion allows for fluctuations in position, size and shape. Finally, the obtained Monte Carlo results are compared to experimental observations made with a spin-polarized scanning tunneling microscope on

Pd/Fe/Ir(111). Experimentally, an electric tunnel current was used to locally induce a stochastic switching between skyrmion and ferromagnetic state. In this way, mean lifetimes of the two states were acquired as a function of an external magnetic field. The mean lifetimes determined from the Monte Carlo calculations were linearly rescaled to the experimentally determined lifetimes which allowed for a calibration of energy parameters and Monte Carlo time steps with real units. A discrepancy between the obtained energy parameters and the energy parameters suitable to describe an extended Pd/Fe/Ir(111) film can be expected since the magnetic skyrmions were pinned to atomic defects in the experimental system.

Chapter 5 dealt with the influence of a boundary of a two-dimensional hexagonal lattice on the formation of spin-spiral states. Nearest-neighbor exchange and Dzyaloshinskii-Moriya interactions were considered. Analytical calculations showed that a parallel alignment of the spin-spiral vector with respect to an edge of the system formed by a close-packed atomic row possesses the lowest energy. An additional reduction of edge energy due to an edge tilt effect of the spin-spiral was obtained using a combination of variation calculus with the continuum model and Monte Carlo calculations. The results were employed to explain experimental observations about spin-spiral states in Pd/Fe islands on Ir(111).

For chapter 6, the focus was on the effects of edges on the spatial orientation of adjacent domains of the nanoskyrmion lattice in Fe/Ir(111). The formation of triple-domain states in triangular Fe islands was found as a result of incompatibility of square skyrmion lattice and triangular island boundary. A diagonal of the nanoskyrmion lattice couples parallel to an island edge. This behavior was observed both in experiment and Monte Carlo calculations based on an energy parameter set that was reported by S.Heinze *et al.* in Ref. [21]. The Monte Carlo calculations could be used to determine the potential save of edge energy as 8.1 meV/nm due to a favorable orientation of the adjacent nanoskyrmion lattice. Additionally, the energy cost of 11.4 meV for the formation of a domain wall was obtained. Finally, the formation of triple-domain states in triangular Fe islands could be ascribed to entropy effects. At very low temperatures, the energetically more favorable single-domain state can't be formed via a continuous reduction of domain wall length due to in-

trinsic pinning effects arising from the energetically spatially inhomogeneous nanoskyrmion lattice. In experiment, additional pinning effects can be present as a result of e.g. atomic defects. Moreover, the edge energies may be different because of energy parameters which are locally different compared to the interior of an extended magnetic film. This could change the energies of single- and triple-domain states in triangular islands. Beside of this, the influence of a ferromagnetic edge was studied. In experiment, this edge condition was achieved by additional ferromagnetic Ni islands. In contrast to an edge of an Fe island, a side of the magnetic unit cell couples parallel to a ferromagnetic edge. This can be understood qualitatively by the fact that a diagonal of the magnetic unit cell possesses, in contrast to a side of the magnetic unit cell, a zero magnetic moment in average.

Chapter 7 dealt with spatial modulations of the energy parameters in skyrmionic systems. Firstly, linear variations were employed to show a convenient method to determine the phase space of skyrmionic systems. From the obtained skyrmion radii as a function of position in phase space, a minimal skyrmion radius of about $0.52\,a$ on hexagonal lattices with lattice constant a was determined. Secondly, periodic spatial modulations of the energy parameters were employed to obtain zigzag type spin-spirals and deformed skyrmionic states. A qualitative agreement with recent observations of deformed skyrmions in triple layers of Fe on Ir(111) was achieved.

Bibliography

[1] Osterkamp, J. Älteste Höhlenmalereien in Ostasien? (2014). URL `http://www.spektrum.de/news/aelteste-hoehlenmalereien-in-ostasien/1311775`. Retrieved on 24.10.2016.

[2] Daniel, E. D., Mee, C. D. & Clark, M. H. (eds.) *Magnetic Recording: The first 100 years* (IEEE Press, 1999).

[3] Richter, H. J. The transition from longitudinal to perpendicular recording. *J. Phys. D: Appl. Phys.* **40** (2007).

[4] Toshiba achieves world's highest areal density in a 2.5-inch hard disk drive (2015). URL `http://toshiba.semicon-storage.com/eu/company/news/2015/02/storage-20150224-4.html`. Retrieved on 06.09.2016.

[5] Mee, C. & Fan, G. A proposed beam-addressable memory. *IEEE Transactions on Magnetics* **3**, 72-76 (1967).

[6] Rottmayer, R. E. *et al.* Heat-assisted magnetic recording. *IEEE Transactions on Magnetics* **42**, 2417-2421 (2006).

[7] Vogler, C., Abert, C., Bruckner, F., Suess, D. & Praetorius, D. Heat-assisted magnetic recording of bit-patterned media beyond 10 Tb/in^2. *Applied Physics Letters* **108**, 102406 (2016).

[8] Kiselev, N. S., Bogdanov, A., Schäfer, R. & Rößler, U. K. Chiral skyrmions in thin magnetic films: New objects for magnetic storage technologies? *J. Phys. D: Appl. Phys.* **44**, 392001 (2011).

[9] Fert, A., Cros, V. & Sampaio, J. Skyrmions on the track. *Nat. Nanotechnol.* **8**, 152-156 (2013).

[10] Bogdanov, A. N. & Yablonskiĭ, D. A. Thermodynamically stable "vortices" in magnetically ordered crystals. The mixed state of magnets. *Zh. Eksp. Teor. Fiz.* **95**, 178-182 (1989).

[11] Bogdanov, A. & Hubert, A. Thermodynamically stable magnetic vortex states in magnetic crystals. *J. Magn. Magn. Mater.* **138**, 255 - 269 (1994).

[12] Bogdanov, A. & Hubert, A. The properties of isolated magnetic vortices. *Phys. Stat. Sol. (b)* **186**, 527-543 (1994).

[13] Mühlbauer, S. *et al.* Skyrmion lattice in a chiral magnet. *Science* **323**, 915-919 (2009).

[14] Pappas, C. *et al.* Chiral paramagnetic skyrmion-like phase in MnSi. *Phys. Rev. Lett.* **102**, 197202 (2009).

[15] Yu, X. Z. *et al.* Real-space observation of a two-dimensional skyrmion crystal. *Nature* **465**, 901-904 (2010).

[16] Yu, X. Z. *et al.* Near room-temperature formation of a skyrmion crystal in thin-films of the helimagnet FeGe. *Nat. Mat.* **10**, 106-109 (2011).

[17] Seki, S., Yu, X. Z., Ishiwata, S. & Tokura, Y. Observation of skyrmions in a multiferroic material. *Science* **336**, 198-201 (2012).

[18] Tonomura, A. *et al.* Real-space observation of skyrmion lattice in helimagnet MnSi thin samples. *Nano Lett.* **12**, 1673-1677 (2012).

[19] Milde, P. *et al.* Unwinding of a skyrmion lattice by magnetic monopoles. *Science* **340**, 1076-1080 (2013).

[20] Park, H. S. *et al.* Observation of the magnetic flux and three-dimensional structure of skyrmion lattices by electron holography. *Nat. Nanotechnol.* **9**, 337-342 (2014).

[21] Heinze, S. *et al.* Spontaneous atomic-scale magnetic skyrmion lattice in two dimensions. *Nat. Phys.* **7**, 713-718 (2011).

[22] Romming, N. *et al.* Writing and deleting single magnetic skyrmions. *Science* **341**, 636-639 (2013).

[23] Dzyaloshinskii, I. A thermodynamic theory of 'weak' ferromagnetism of antiferromagnets. *J. Phys. Chem. Solids* **4**, 241-255 (1958).

[24] Moriya, T. Anisotropic superexchange interaction and weak ferromagnetism. *Phys. Rev.* **120**, 91-98 (1960).

[25] Jonietz, F. *et al.* Spin transfer torques in MnSi at ultralow current densities. *Science* **330**, 1648-1651 (2010).

[26] Zang, J., Mostovoy, M., Han, J. H. & Nagaosa, N. Dynamics of skyrmion crystals in metallic thin films. *Phys. Rev. Lett.* **107**, 136804 (2011).

[27] Yu, X. Z. *et al.* Skyrmion flow near room temperature in an ultralow current density. *Nat. Commun.* **3**, 988 (2012).

[28] Sampaio, J., Cros, V., Rohart, S., Thiaville, A. & Fert, A. Nucleation, stability and current-induced motion of isolated magnetic skyrmions in nanostructures. *Nat. Nanotechnol.* **8**, 839-844 (2013).

[29] Iwasaki, J., Mochizuki, M. & Nagaosa, N. Current-induced skyrmion dynamics in constricted geometries. *Nat. Nanotechnol.* **8**, 742-747 (2013).

[30] Iwasaki, J., Mochizuki, M. & Nagaosa, N. Universal current-velocity relation of skyrmion motion in chiral magnets. *Nat. Commun.* **4**, 1463 (2013).

[31] Kong, L. & Zang, J. Dynamics of an insulating skyrmion under a temperature gradient. *Phys. Rev. Lett.* **111**, 067203 (2013).

[32] Kovalev, A. A. Skyrmionic spin Seebeck effect via dissipative thermomagnonic torques. *Phys. Rev. B* **89**, 241101 (2014).

[33] Lin, S.-Z., Batista, C. D., Reichhardt, C. & Saxena, A. ac current generation in chiral magnetic insulators and skyrmion motion induced by the spin Seebeck effect. *Phys. Rev. Lett.* **112**, 187203 (2014).

[34] Iwasaki, J., Koshibae, W. & Nagaosa, N. Colossal spin transfer torque effect on skyrmion along the edge. *Nano Lett.* **14**, 4432-4437 (2014).

[35] Schütte, C., Iwasaki, J., Rosch, A. & Nagaosa, N. Inertia, diffusion and dynamics of a driven skyrmion. *Phys. Rev. B* **90**, 174434 (2014).

[36] Troncoso, R. E. & Núñez, A. S. Thermally assisted current-driven skyrmion motion. *Phys. Rev. B* **89**, 224403 (2014).

[37] Knoester, M. E., Sinova, J. & Duine, R. A. Phenomenology of current-skyrmion interactions in thin films with perpendicular magnetic anisotropy. *Phys. Rev. B* **89**, 064425 (2014).

[38] Zhang, X. *et al.* Skyrmion-skyrmion and skyrmion-edge repulsions in skyrmion-based racetrack memory. *Sci. Rep.* **5**, 7643 (2015).

[39] Zhang, X., Ezawa, M. & Zhou, Y. Magnetic skyrmion logic gates: Conversion, duplication and merging of skyrmions. *Sci. Rep.* **5**, 9400 (2015).

[40] Woo, S. *et al.* Observation of room-temperature magnetic skyrmions and their current-driven dynamics in ultrathin metallic ferromagnets. *Nat. Mat.* **15**, 501-506 (2016).

[41] Moreau-Luchaire, C. *et al.* Additive interfacial chiral interaction in multilayers for stabilization of small individual skyrmions at room temperature. *Nat. Nanotechnol.* **11**, 444-448 (2016).

[42] Blundell, S. *Magnetism in Condensed Matter* (Oxford University Press, 2001).

[43] O'Handley, R. *Modern Magnetic Materials* (John Wiley & Sons, Inc., 2000).

[44] Jackson, J. D. *Klassische Elektrodynamik* (de Gruyter, 2006).

[45] Eschenfelder, A. H. *Magnetic bubble technology* (Springer, 1980/81).

[46] Skomski, R., Kashyap, A., Zhou, J. & Sellmyer, D. J. Anisotropic exchange. *J. Appl. Phys.* **97**, 10B302 (2005).

[47] Levi, P. M. & Fert, A. Anisotropy induced by nonmagnetic impurities in CuMn spin-glass alloys. *Phys. Rev. B* **23**, 4667-4690 (1981).

[48] Bak, P. & Jensen, M. H. Theory of helical magnetic structures and phase transitions in MnSi and FeGe. *J. Phys. C: Solid St. Phys.* **13**, L881 (1980).

[49] Fert, A. Magnetic and transport properties of metallic multilayers. In *Metallic Multilayers*, vol. 59 of *Materials Science Forum*, 439-480 (Trans Tech Publications, 1991).

[50] Fert, A. & Levi, P. Role of anisotropic exchange interactions in determining the properties of spin-glasses. *Phys. Rev. Lett.* **44**, 1538-1541 (1980).

[51] MacDonald, A. H., Girvin, S. M. & Yoshioka, D. $\frac{t}{U}$ expansion for the Hubbard model. *Phys. Rev. B* **37**, 9753-9756 (1988).

[52] Wieser, R., Vedmedenko, E. Y. & Wiesendanger, R. Entropy driven phase transition in itinerant antiferromagnetic monolayers. *Phys. Rev. B* **77**, 064410 (2008).

[53] Skyrme, T. H. R. A non-linear field theory. *Proc. R. Soc. A* **260**, 127-138 (1961).

[54] Rößler, U. K., Bogdanov, A. N. & Pfleiderer, C. Spontaneous skyrmion ground states in magnetic metals. *Nature* **442**, 797-801 (2006).

[55] Nagaosa, N. & Tokura, Y. Topological properties and dynamics of magnetic skyrmions. *Nat. Nanotechnol.* **8**, 899-911 (2013).

[56] Kézsmárki, I. *et al.* Néel-type skyrmion lattice with confined orientation in the polar magnetic semiconductor GaV_4S_8. *Nat. Mat.* **14**, 1116-1122 (2015).

[57] Romming, N., Kubetzka, A., Hanneken, C., von Bergmann, K. & Wiesendanger, R. Field-dependent size and shape of single magnetic skyrmions. *Phys. Rev. Lett.* **114**, 177203 (2015).

[58] Crépieux, A. & Lacroix, C. Dzyaloshinsky-Moriya interactions induced by symmetry breaking at a surface. *J. Magn. Magn. Mater.* **182**, 341-349 (1998).

[59] Jiang, W. *et al.* Blowing magnetic skyrmion bubbles. *Science* **349**, 283-286 (2015).

[60] von Bergmann, K. *et al.* Observation of a complex nanoscale magnetic structure in a hexagonal Fe monolayer. *Phys. Rev. Lett.* **96**, 167203 (2006).

[61] von Bergmann, K. *et al.* Complex magnetism of the Fe monolayer on Ir(111). *New J. Phys.* **9**, 396 (2007).

[62] von Bergmann, K., Kubetzka, A., Pietzsch, O. & Wiesendanger, R. Interface-induced chiral domain walls, spin spirals and skyrmions revealed by spin-polarized scanning tunneling microscopy. *J. Phys. Condens. Matter* **26**, 394002 (2014).

[63] Butenko, A. B., Leonov, A. A., Rößler, U. K. & Bogdanov, A. N. Stabilization of skyrmion textures by uniaxial distortions in centrosymmetric cubic helimagnets. *Phys. Rev. B* **82**, 052403 (2010).

[64] Schwabl, F. *Statistische Mechanik* (Springer, 2000).

[65] Eyring, H. The activated complex in chemical reactions. *J. Chem. Phys.* **3**, 107-115 (1935).

[66] Laidler, K. J. & King, M. C. The development of transition-state theory. *J. Phys. Chem.* **87**, 2657-2664 (1983).

[67] Néel, L. Theorie du trainage magnétique des ferromagnetiques en grain fins avec application aux terres cuites. *Ann. Géophys.* **5**, 99 (1949).

[68] Brown, W. F. Thermal fluctuations of a single-domain particle. *Phys. Rev.* **130**, 1677 (1963).

[69] Coffey, W. T. & Kalmykov, Y. P. Thermal fluctuations of magnetic nanoparticle: Fifty years after Brown. *J. Appl. Phys.* **112**, 121301 (2012).

[70] Schütte, C. & Rosch, A. Dynamics and energetics of emergent magnetic monopoles in chiral magnets. *Phys. Rev. B* **90**, 174432 (2014).

[71] Oike, H. *et al.* Interplay between topological and thermodynamic stability in a metastable magnetic skyrmion lattice. *Nat. Phys.* **12**, 62-66 (2016).

[72] Yin, G. *et al.* Topological charge analysis of ultrafast single skyrmion creation. *Phys. Rev. B* **93**, 174403 (2016).

[73] Rósza, L., Simon, E., Palotás, K., Udvardi, L. & Szunyogh, L. Complex magnetic phase diagram and skyrmion lifetime in ultrathin film from atomistic simulations. *Phys. Rev. B* **93**, 024417 (2016).

[74] Bessarab, P. F., Uzdin, V. M. & Jónsson, H. Method for finding mechanism and activation energy of magnetic transitions, applied to skyrmion and antivortex annihilation. *Comput. Phys. Commun.* **196**, 335 - 347 (2015).

[75] Rohart, S., Miltat, J. & Thiaville, A. Path to collapse for an isolated Néel skyrmion. *Phys. Rev. B* **93**, 214412 (2016).

[76] Lobanov, I. S., Jónsson, H. & Uzdin, V. M. Mechanism and activation energy of magnetic skyrmion annihilation obtained from minimum energy path calculations. *Phys. Rev. B* **94**, 174418 (2016).

[77] Landau, D. P. & Binder, K. *A guide to Monte Carlo simulations in Statistical Physics* (Cambridge University Press, 2000).

[78] Blügel, S. *et al.* (eds.) *Computational Condensed Matter Physics* (Forschungszentrum Jülich GmbH, 2006).

[79] Metropolis, N., Rosenbluth, A. W., Rosenbluth, M. N., Teller, A. H. & Teller, E. Equation of state calculations by fast computing machines. *J. Chem. Phys.* **21**, 1087-1092 (1953).

[80] Wolter, B. A. W. *Magnetic Atom Manipulation and Spin-dependent Atomic Friction Investigated by Spin-polarized Scanning Tunneling Microscopy and Monte Carlo Simulations.* Ph.D. thesis, Universität Hamburg (2014).

[81] Fisher, M. E. & Ferdinand, A. E. Interfacial, boundary, and size effects at critical points. *Phys. Rev. Lett.* **19**, 4:169-172 (1967).

[82] Fisher, M. E. & Barber, M. N. Scaling theory for finite-size effects in the critical region. *Phys. Rev. Lett.* **28**, 23:1516-1519 (1972).

[83] Landau, D. P. Finite-size behavior of the Ising square lattice. *Phys. Rev. B* **13**, 13:2997-3011 (1976).

[84] Landau, D. P. Finite-size behavior of the simple-cubic Ising lattice. *Phys. Rev. B* **14**, 14:225-261 (1976).

[85] Berg, B. & Lüscher, M. Definition and statistical distributions of a topological number in the lattice O(3) σ-model. *Nuclear Physics B* **190**, 412-424 (1981).

[86] van Oosterom, A. & Strackee, J. The solid angle of a plane triangle. *IEEE Transactions on Biomedical Engineering* **BME-30**, 125-126 (1983).

[87] Ralls, K. S. *et al.* Discrete resistance switching in submicrometer silicon inversion layers: Individual interface traps and low-frequency ($\frac{1}{f}$?) noise. *Phys. Rev. Lett.* **52**, 228-231 (1984).

[88] Ralls, K. S. & Buhrman, R. A. Defect interactions and noise in metallic nanoconstrictions. *Phys. Rev. Lett.* **60**, 2434-2437 (1988).

[89] Bode, M., Pietzsch, O., Kubetzka, A. & Wiesendanger, R. Shape-dependent thermal switching behavior of superparamagnetic nanoislands. *Phys. Rev. Lett.* **92**, 067201 (2004).

[90] Krause, S., Berbil-Bautista, L., Herzog, G., Bode, M. & Wiesendanger, R. Current-induced magnetization switching with a spin-polarized scanning tunneling microscope. *Science* **317**, 1537-1540 (2007).

[91] Krause, S. *et al.* Magnetization reversal of nanoscale islands: How size and shape affect the Arrhenius prefactor. *Phys. Rev. Lett.* **103**, 127202 (2009).

[92] Simoen, E., Kaczer, B., Toledano-Luque, M. & Claeys, C. Random telegraph noise: From a device physicist's dream to a designer's nightmare. *ECS Transactions* **39**, 3-15 (2011).

[93] Wiesendanger, R. *Scanning Probe Microscopy and Spectroscopy: Methods and Applications* (Cambridge University Press, Cambridge, 1994).

[94] Wortmann, D., Heinze, S., Kurz, P., Bihlmayer, G. & Blügel, S. Resolving complex atomic-scale spin structures by spin-polarized scanning tunneling microscopy. *Phys. Rev. Lett.* **86**, 4132 (2001).

[95] Tersoff, J. & Hamann, D. R. Theory and application for the scanning tunneling microscope. *Phys. Rev. Lett.* **50**, 1998 (1983).

[96] Stapelfeldt, T., Wieser, R., Vedmedenko, E. Y. & Wiesendanger, R. Domain wall manipulation with a magnetic tip. *Phys. Rev. Lett.* **107**, 027203 (2011).

[97] Ralph, D. C. & Stiles, M. D. Spin transfer torques. *J. Magn. Magn. Mater.* **320**, 1190-1216 (2008).

[98] Langreth, D. C. & Wilkins, J. W. Theory of spin resonance in dilute magnetic alloys. *Phys. Rev. B* **6**, 3189-3227 (1972).

[99] Newman, M. E. J. & Barkema, G. T. *Monte Carlo Methods in Statistical Physics* (Oxford University Press, 1999).

[100] Dupé, B., Hoffmann, M., Paillard, C. & Heinze, S. Tailoring magnetic skyrmions in ultra-thin transition metal films. *Nat. Commun.* **5**, 4030 (2014).

[101] Simon, E., Palotás, K., Rózsa, L., Udvardi, L. & Szunyogh. Formation of magnetic skyrmions with tunable properties in PdFe bilayer deposited on Ir(111). *Phys. Rev. B* **90**, 094410 (2014).

[102] Dupé, B., Bihlmayer, G., Böttcher, M., Blügel, S. & Heinze, S. Engineering skyrmions in transition-metal multilayers for spintronics. *Nat. Commun.* **7**, 11779 (2016).

[103] Banerjee, S., Rowland, J., Erten, O. & Randeria, M. Enhanced stability of skyrmions in two-dimensional chiral magnets with Rashba spin-orbit coupling. *Phys. Rev. X* **4**, 031045 (2014).

[104] Keesman, R. *et al.* Degeneracies and fluctuations of Néel skyrmions in confined geometries. *Phys. Rev. B* **92**, 134405 (2015).

[105] Ezawa, M. Skyrmion burst and multiple quantum walk in thin ferromagnetic films. *Phys. Lett. A* **375**, 3610-3614 (2011).

[106] Ramirez, A. P., Hayashi, A., Cava, R. J., Siddharthan, R. & Shastry, B. S. Zero-point entropy in 'spin ice'. *Nature* **399**, 333-335 (1999).

[107] McMichael, R. D., Shull, R. D., Swartzendruber, L. J. & Bennet, L. H. Magnetocaloric effect in superparamagnets. *J. Magn. Magn. Mater.* **111**, 29-33 (1992).

[108] Kramers, H. A. Brownian motion in a field of force and the diffusion model of chemical reactions. *Physica* **VII**, 284-304 (1940).

[109] Nowak, U., Chantrell, R. W. & Kennedy, E. C. Monte Carlo simulation with time step quantification in terms of Langevin dynamics. *Phys. Rev. Lett.* **84**, 163-166 (2000).

[110] Khajetoorians, A. A. *et al.* Current-driven spin dynamics of artificially constructed quantum magnets. *Science* **339**, 55-59 (2013).

[111] Rohart, S. & Thiaville, A. Skyrmion confinement in ultrathin film nanostructures in the presence of Dzyaloshinskii-Moriya interaction. *Phys. Rev. B* **88**, 184422 (2013).

[112] Rohart, Stanislas. Université Paris-sud, Laboratoire de Physique des Solides, Bâtiment 510, 91405 ORSAY Cedex, France. Private communication.

[113] Schmidt, L. *et al.* Symmetry breaking in spin spirals and skyrmions by in-plane and canted magnetic fields. *New J. Phys.* **18**, 075007 (2016).

[114] Binnig, G., Rohrer, H., Gerber, C. & Weibel, E. Surface studies by scanning tunneling microscopy. *Phys. Rev. Lett.* **49**, 57-61 (1982).

[115] Wiesendanger, R., Güntherodt, H.-J., Güntherodt, G., Gambino, R. J. & Ruf, R. Observation of vacuum tunneling of spin-polarized electrons

with the scanning tunneling microscope. *Phys. Rev. Lett.* **65**, 247-250 (1990).

[116] Pietzsch, O., Kubetzka, A., Haude, D., Bode, M. & Wiesendanger, R. A low-temperature ultrahigh vacuum scanning tunneling microscope with a split-coil magnet and a rotary motion stepper motor for high spatial resolution studies of surface magnetism. *Rev. Sci. Instrum.* **71**, 424 (2000).

[117] Hsu, P.-J. *et al.* Guiding spin spirals by local uniaxial strain relief. *Phys. Rev. Lett.* **116**, 017201 (2016).

[118] von Bergmann, K., Menzel, M., Kubetzka, A. & Wiesendanger, R. Influence of the local atom configuration on a hexagonal skyrmion lattice. *Nano Lett.* **15**, 3280 (2015).

[119] Iaia, D., Kubetzka, A., von Bergmann, K. & Wiesendanger, R. Structural and magnetic properties of NiFe bilayer nanostructures on Ir(111). *Phys. Rev. B* **93**, 134409 (2016).

[120] Sonntag, A., Hermenau, J., Krause, S. & Wiesendanger, R. Thermal stability of an interface-stabilized skyrmion lattice. *Phys. Rev. Lett.* **113**, 077202 (2014).

[121] Heinze, S. Simulation of spin-polarized scanning tunneling microscopy images of nanoscale non-collinear magnetic structures. *Appl. Phys. A* **85**, 407 (2006).

[122] Kubetzka, A., Pietzsch, O., Bode, M. & Wiesendanger, R. Spin-polarized scanning tunneling microscopy study of 360° walls in an external magnetic field. *Phys. Rev. B* **67**, 020401 (2003).

[123] Butenko, A. *Phenomenological theory of chiral states in magnets with Dzyaloshinskii-Moriya interactions.* Ph.D. thesis, Technische Universität Dresden (2012).

[124] Heide, M., Bihlmayer, G. & Blügel, S. Dzyaloshinskii-Moriya interaction accounting for the orientation of magnetic domains in ultrathin films: Fe/W(110). *Phys. Rev. B* **78**, 140403 (2008).

[125] Bergqvist, L., Taroni, A., Bergman, A., Etz, C. & Eriksson, O. Atomistic spin dynamics of low-dimensional magnets. *Phys. Rev. B* **87**, 144401 (2013).

[126] Zimmermann, B., Heide, M., Bihlmayer, G. & Blügel, S. First-principles analysis of a homochiral cycloidal magnetic structure in a monolayer Cr on W(110). *Phys. Rev. B* **90**, 115427 (2014).

[127] Rósza, L., Udvardi, L., Szunyogh, L. & A., S. I. Magnetic phase diagram of an Fe monolayer on W(110) and Ta(110) surface based on *ab initio* calculations. *Phys. Rev. B* **91**, 144424 (2015).

[128] Shibata, K. *et al.* Large anisotropic deformation of skyrmions in strained crystal. *Nat. Nanotechnol.* **10**, 589-592 (2015).

[129] Woo, S. *et al.* Observation of room-temperature magnetic skyrmions and their current-driven dynamics in ultrathin metallic ferromagnets. *Nat. Mat.* **15**, 501-506 (2016).

[130] Hsu, P.-J. *et al.* Electric-field-driven switching of individual magnetic skyrmions. *Nat. Nanotechnol.* **12**, 123-126 (2016).

[131] Bauer, E. & van der Merwe, J. H. Structure and growth of crystalline superlattices: From monolayer to superlattice. *Phys. Rev. B* **33**, 3657 (1986).

[132] An, B., Zhang, L., Fukuyama, S. & Yokogawa, K. Growth and structural transition of Fe ultrathin films on Ni(111) investigated by LEED and STM. *Phys. Rev. B* **79**, 085406 (2009).

[133] Phark, S.-H. *et al.* Reduced-dimensionality-induced helimagnetism in iron nanoislands. *Nat. Commun.* **5**, 5183 (2014).

[134] Vedmedenko, E. Y. *et al.* Domain wall orientation in magnetic nanowires. *Phys. Rev. Lett.* **92**, 077207 (2004).

[135] Vedmedenko, E. Y., von Bergmann, K., Oepen, H. P. & Wiesendanger, R. Lattice-dependent anisotropy in the orientation of magnetic domain walls. *J. Magn. Magn. Mater.* **290-291**, 746-749 (2005).

[136] Porrati, F., Wulfhekel, W. & Kirschner, J. An analytical model for ultrathin films with spatially varying magnetic anisotropies. *J. Magn. Magn. Mater.* **270**, 22-31 (2004).

[137] Hanneken, C., Kubetzka, A., von Bergmann, K. & Wiesendanger, R. Pinning and movement of individual nanoscale magnetic skyrmions via defects. *New J. Phys.* **18**, 055009 (2016).

Publications

- J. Hagemeister, N. Romming, K. von Bergmann, E.Y. Vedmedenko & R. Wiesendanger. Stability of single skyrmionic bits. Nat. Commun. **6** 8455 (2015).
- A. Siemens, Y. Zhang, J. Hagemeister, E. Y. Vedmedenko & R. Wiesendanger. Minimal radius of magnetic skyrmions: statics and dynamics. New J. Phys. **18** 045021 (2016)
- L. Schmidt, J. Hagemeister, P.-J. Hsu, A. Kubetzka, K. von Bergmann & R. Wiesendanger. Symmetry breaking in spin spirals and skyrmions by in-plane and canted magnetic fields. New J. Phys. **18** 075007 (2016).
- J. Hagemeister, E.Y. Vedmedenko & R. Wiesendanger. Pattern formation in skyrmionic materials with anisotropic environments. Phys. Rev. B **94** 104434 (2016).
- J. Hagemeister, D. Iaia, E.Y. Vedmedenko, K. von Bergmann, A. Kubetzka & R. Wiesendanger. Skyrmions at the edge: Confinement effects in Fe/Ir(111). Phys. Rev. Lett. **117** 207202 (2016).

Talks and posters

- Julian Hagemeister, Robert Wieser, Elena Vedmedenko and Roland Wiesendanger. Creation and annihilation of skyrmions in ultrathin magnetic films. Spring Conference, Deutsche Physikalische Gesellschaft, Dresden (2014).
- Julian Hagemeister, Elena Vedmedenko and Roland Wiesendanger. Tailoring skyrmion lattices. SKYMAG, Paris (2014)
- Julian Hagemeister, Elena Vedmedenko and Roland Wiesendanger. Stability of Single Skyrmionic Bits. SFB 668-Seminar, Hamburg (2014).
- Julian Hagemeister, Niklas Romming, Kirsten von Bergmann, Elena Y. Vedmedenko and Roland Wiesendanger. Stability of Single Skyrmionic Bits. Spring Conference, Deutsche Physikalische Gesellschaft, Berlin (2015).

- Julian Hagemeister, André Kubetzka, Elena Y. Vedmedenko and Roland Wiesendanger. Confinement effects in lattices of nanoskyrmions. 20th International Conference on Magnetism, Barcelona (2015)
- Julian Hagemeister, Elena Y. Vedmedenko and Roland Wiesendanger. Influence of lattice strain on the formation of magnetic skyrmions. Spring Conference, Deutsche Physikalische Gesellschaft, Regensburg (2016).

Acknowledgements

Finally, I gladly thank the people who contributed to this PhD thesis with their support during the last years.

- Prof. Dr. R. Wiesendanger for his advice and the opportunity to work in an excellent research team with the possibility to present results at international conferences.
- Dr. E. Vedmedenko for her great support and advice as well as the revision of the manuscript.
- Mario Krizanac, David Altwein and Dr. Kolja Them for many discussions and a nice working atmosphere in the shared office.
- My former colleague Dr. Thim Stapelfeldt who guided me during my time as a Master student in this research group. That is when I wrote the main parts of the Monte Carlo program which I continued to improve as a PhD student thereafter.
- My colleague Jonas Harm for a lot of help with programs for graphic design as POV-Ray.
- My colleagues Niklas Romming, Lorenz Schmidt, Dr. Pin-Jui Hsu for plenty of interesting and fruitful discussions.
- My colleagues Dr. André Kubetzka and Dr. Kirsten von Bergmann from whom I got a lot of inspiration for investigations.
- My colleagues Johannes Friedlein and Dr. Stefan Krause for stimulating discussions.
- My girlfriend Sarah for her love and encouragement.
- My parents and sister for their moral support, especially during the most challenging periods of the PhD time.

Eidesstattliche Versicherung
Declaration on oath

Hiermit erkläre ich an Eides statt, dass ich die vorliegende Dissertationsschrift selbst verfasst und keine anderen als die angegebenen Quellen und Hilfsmittel benutzt habe.

I hereby declare, on oath, that I have written the present dissertation by my own and have not used other than the acknowledged resources and aids.

Hamburg, den 29.08.2017
Julian Hagemeister